UNIVERSITY OF CALIFORNIA SAN DIEGO

Novel Deposition Methods for Group III-Nitride Films at Low Temperatures

A Dissertation submitted in partial satisfaction of the requirements
for the degree Doctor of Philosophy

in

Chemistry

by

Aaron J. McLeod

Committee in charge:

Professor Andrew C. Kummel, Chair
Professor Peter Asbeck
Professor Michael Sailor
Professor Amitabha Sinha
Professor Mark H. Thiemens

2023

The Dissertation of Aaron J. McLeod is approved, and it is acceptable in quality and form for publication on microfilm and electronically.

University of California San Diego

2023

DEDICATION

To all educators, mentors, and role models that have nurtured my sense of curiosity. It was only through your successive efforts and encouragements that this was possible.

TABLE OF CONTENTS

LIST OF TABLES

LIST OF FIGURES

LIST OF ABBREVIATIONS

AlN	Aluminum nitride
GaN	Gallium nitride
InGaN	Indium gallium nitride
SiC	Silicon carbide
SiO_2	Silicon dioxide
Al_2O_3	Aluminum oxide; sapphire
Ar	Argon
Kr	Krypton
N_2	Nitrogen
BEOL	Back end of the line
WBG	Wide bandgap
ALD	Atomic layer deposition
PE-ALD	Plasma enhanced atomic layer deposition
ALA	Atomic layer annealing
CVD	Chemical vapor deposition
MOCVD	Metal organic chemical vapor deposition
MBE	Molecular beam epitaxy
ICP	Inductively coupled plasma
TDMAA	Tris(dimethylamido) aluminum (III)
TDMAGa	Tris(dimethylamido) gallium (III)
N_2H_4	Hydrazine
DC	Direct current

RF	Radio frequency
W	Watt
sccm	standard cubic centimeter per minute
κ	Thermal conductivity
G	Thermal boundary conductance
XPS	X-ray photoelectron spectroscopy
CMA	Cylindrical mirror analyzer
XRD	X-ray diffraction
XRR	X-ray reflectivity
FWHM	Full width at half max
GI-XRD	Grazing incidence x-ray diffraction
SiC	Silicon carbide
TEM	Transmission electron microscopy
STEM	Scanning transmission electron microscopy
HR-TEM	High resolution transmission electron microscopy
SAED	Selected area electron diffraction
FFT	Fast Fourier transform
SE	Spectroscopic ellipsometry
TDTR	Time domain thermoreflectance
BTE	Boltzmann transport equation
DMM	Diffuse mismatch model
BVK	Born von Karman

ACKNOWLEDGEMENTS

My deepest appreciation goes to Professor Andrew C. Kummel for years of inspiration and insight. Your ability to cast a positive light on and draw meaning from every set of results has been a lesson on how to approach any challenge. From the day I joined your research group I have continually grown as a scientist.

Equal appreciation goes to my senior student, Scott T. Ueda, who courageously guided a chemist into the world of vacuum and materials science. Your explanations, diagrams scribbled on sticky notes, and quizzing me on wrench sizes necessary for any fitting provided the technical foundation for my graduate education.

I also wish to acknowledge my lab mates over the years for sharing of parts and expertise: Dr. Steven Wolf, Dr. Christopher Ahles, Dr. Yunil Cho, Dr. Theodor Weiss, Dr. SeongUk Yun, Victor Wang, Ping-Che Lee, James Huang, Jimmy Kuo, Jacob Watson, Jannick Fammels, Harshil Kashyap, Chelsea Swank, and my new breakroom/office-mate, Dr. Dohyun Go. To Victor Wang, your friendship and commiseration upon every equipment failure, minor or catastrophic, will not be forgotten! It would be a pleasure to work with you again. To my junior student, Ping-Che Lee, I thank you for sharing your expertise on TEM and for your patience and careful attention as we sorted out equipment malfunctions and process challenges. I wish you all the best in your future work! Many thanks go to our collaborators, especially at Stanford University: Dr. Christopher Perez and Dr. Michelle Chen, and their former advisors Dr. Eric Pop and Dr. Ken Goodson. You have given our work the context necessary to make meaningful contribution to technological development.

Without the investment and technical expertise of our industry partners this research would not have been possible: the Semiconductor Research Corporation and all partner companies, EMD Electronic Materials, Rasirc, Applied Materials, and BASF.

I would like to thank my committee members, Dr. Michael Sailor, Dr. Amit Sinha, Dr. Mark Thiemens, and Dr. Peter Asbeck, for their participation and guidance throughout my time at UCSD. The mentorship provided by Dr. Katherine Willets and my former lab mates at my undergraduate institution, Temple University, has been instrumental in guiding my academic career. This group introduced me to the world of nanoscience and fostered my interest in working with atomic-scale precision. Further, my development as a scientist and scholar first came about by the passionate instruction and dedication of many teachers of my primary and secondary education, specifically Mrs. Buzin, Ms. Esris, and Mrs. Price.

Final recognition goes to the family and friends that have supported me throughout all stages of my life and education. To my parents, grandparents, aunt, and brothers, you have provided me a wealth of opportunities and the resources necessary to pursue them.

Chapter 2, in full, is a reprint of the material as it appears in the following publication, of which the dissertation author was the primary researcher and author:

McLeod, Aaron J.; Ueda, Scott T.; Lee, Ping Che; Spiegelman, Jeff; Kanjolia, Ravindra; Moinpour, Mansour; Woodruff, Jacob; Kummel, Andrew C. "Pulsed Chemical Vapor Deposition for Crystalline Aluminum Nitride Thin Films and Buffer Layers on Silicon and Silicon Carbide", Thin Solid Films, vol. 768, 2023.

Chapter 3, in full, has been submitted for publication of the material as it may appear in the following publication, of which the dissertation author was the primary researcher and author:

McLeod, Aaron J.; Lee, Ping Che; Ueda, Scott T.; Devereaux, Zachary J.; Winter, Charles H.; Spiegelman, Jeff; Kanjolia, Ravindra; Moinpour, Mansour; Kummel, Andrew C. "Atomic Layer Annealing with Radio Frequency Substrate Bias for Control of Grain Morphology in Gallium Nitride Thin Films", Materials Research Society Bulletin Impact Section, 2023.

Chapter 4, in part, is being prepared for publication, of which the dissertation author was a primary researcher and coauthor:

McLeod, Aaron J. and Perez, Christopher; Chen, Michelle; Yi, Su-in; Vaziri, Sam; Hood, Ryan; Ueda, Scott T.; Bao, Xinyu; Asheghi, Mehdi; Park, Woosung; Talin, A. Alec; Kumar, Suhas; Pop, Eric; Kummel, Andrew C.; Goodson, Kenneth E. "High Thermal Conductivity of Sub-Micron Aluminum Nitride Thin Films Sputter Deposited at Low Temperature"

VITA

2018 Bachelor of Science in Chemistry, Temple University

2021 Master of Science in Chemistry, University of California San Diego

2023 Doctor of Philosophy in Chemistry, University of California San Diego

PUBLICATIONS

Perez, Christopher and McLeod, Aaron J.; Chen, Michelle; Yi, Su-in; Vaziri, Sam; Hood, Ryan; Ueda, Scott T.; Bao, Xinyu; Asheghi, Mehdi; Park, Woosung; Talin, A. Alec; Kumar, Suhas; Pop, Eric; Kummel, Andrew C.; Goodson, Kenneth E. "High Thermal Conductivity of Sub-Micron Aluminum Nitride Thin Films Sputter Deposited at Low Temperature", In preparation.

McLeod, Aaron J.; Lee, Ping Che; Ueda, Scott T.; Devereaux, Zachary J.; Winter, Charles H.; Spiegelman, Jeff; Kanjolia, Ravindra; Moinpour, Mansour; Kummel, Andrew C. "Atomic Layer Annealing with Radio Frequency Substrate Bias for Control of Grain Morphology in Gallium Nitride Thin Films", *Materials Research Society Bulletin IMPACT Section*, 2023.

McLeod, Aaron J.; Ueda, Scott T.; Lee, Ping Che; Spiegelman, Jeff; Kanjolia, Ravindra; Moinpour, Mansour; Woodruff, Jacob; Kummel, Andrew C. "Pulsed Chemical Vapor Deposition for Crystalline Aluminum Nitride Thin Films and Buffer Layers on Silicon and Silicon Carbide" *Thin Solid Films*, vol. 768, 2023.

Kuo, Cheng-Hsuan; McLeod, Aaron J.; Lee, Ping-Che; Huang, James; Kashyap, Harshil; Wang, Victor; Yun, SeongUk; Zhang, Zichen; Spiegelman, Jeff; Kanjolia, Ravindra; Moinpour, Mansour; Kummel, Andrew C. "Low Resistivity Titanium Nitride Thin Film Fabricated by Atomic Layer Deposition with TiCl4 and Metal-Organic Precursors in Horizontal Vias" In Preparation.

Ueda, Scott T.; Mcleod, Aaron J.; Jo, Youhwan; Zhang, Zichen; Spiegelman, Jeff; Alvarez, Daniel; Moser, Daniel; Kanjolia, Ravindra; Moinpour, Mansour; Woodruff, Jacob; Cho, K.J.; Kummel, Andrew C. "Experimental and Theoretical Determination of the Role of Ions in Atomic Layer Annealing" *Journal of Materials Chemistry C*, vol. 14, 2022.

Cheng, Li; Fan, Bei; Zhang, Zichen; McLeod, Aaron J.; Shipley, Wade; Bandaru, Prabhakar. "The Modulation of Electrokinetic Streaming Potentials of Silicon-Based Surfaces through Plasma-Based Surface Processing" *Langmuir*, vol. 38, 2022.

Ueda, Scott T.; Mcleod, Aaron J.; Alvarez, Daniel; Moser, Daniel; Kanjolia, Ravindra; Woodruff, Jacob; Kummel, Andrew C. "Tris(dimethylamido)aluminum(III) and N_2H_4: Ideal Precursors for the Low-Temperature Deposition of Large Grain, Oriented C-Axis AlN on Si via Atomic Layer Annealing" *Applied Surface Science*, vol. 554, 2021.

FIELD OF STUDY

Major Field: Chemistry

Studies in Surface Science and Vacuum Coatings
Professor Andrew C. Kummel

ABSTRACT OF THE DISSERTATION

Novel Deposition Methods for Group III-Nitride Films at Low Temperatures

by

Aaron J. McLeod

Doctor of Philosophy in Chemistry

University of California San Diego, 2023

Professor Andrew Kummel, Chair

As the scale of transistors in integrated circuits decreases and the density of transistors increases, the precision with which all processes must be carried out scales in all dimensions. This trend has led to the development of atomic layer deposition, a technique that utilizes complementary precursors to perform successive self-limiting surface reactions to deposit materials on a monolayer-by-monolayer basis. In this work, variations of atomic layer deposition and a complementary physical vapor deposition technique are used to deposit aluminum nitride and gallium nitride films at temperatures compatible with industry limitations.

In chapter two, a technique performed in a similar fashion as atomic layer deposition is described using a novel precursor combination to deposit aluminum nitride at 400 ˚C and 580 ˚C. This technique. pulsed chemical vapor deposition, varies from atomic layer deposition in that the surface reactions are not self-limiting; however, precisely controlling precursor dosing and purging results in process control with equivalent atomic-level precision. This technique is demonstrated to deposit polycrystalline and epitaxial films with near bulk density on silicon and silicon carbide substrates, respectively, at temperatures below reported methods in the literature.

Chapter three describes atomic layer annealing for the deposition of polycrystalline gallium nitride films at 275 ˚C. In this method a brief inert ion bombardment is performed following each precursor dosing cycle to crystallize deposited material. Radio-frequency bias applied to the substrate during deposition is shown to modulate the kinetic energy of bombarding ions. This allows the intensity of the resulting collision cascades to be controlled such that the crystallinity of the deposited film can be maximized. Atomic layer deposition is performed at the same temperature as a control, but results in deposition of only amorphous films.

The final chapter describes DC reactive magnetron sputtering of aluminum nitride. The crystal structure of deposited films as a function of varied process parameters is investigated; improvements in crystal structure correlate to improved thermal conductivity in sub-micron thick films. These studies demonstrate the potential of aluminum nitride as a heat spreading material as three-dimensional integration becomes a means by which to further increase transistor density in integrated circuits.

CHAPTER 1

INTRODUCTION

1.1 The Need for Low Temperature Deposition Processes for Group III – Nitride Materials

Group III – nitride materials, such as AlN, GaN, and InGaN, have grown in importance to the microelectronics industry over recent years. Aluminum nitride, for example, is a piezoelectric material used in RF filters for mobile phones and is of particular interest as a heat spreading material in the current dawn of advanced packaging [1–3]; gallium nitride is a desirable electronic material for applications where high voltage, speed, and heat tolerance are required such as in electric vehicle transformers and in aerospace applications [4,5]; indium gallium nitride is a promising candidate for the construction of next-generation micro-light emitting diode (microLED) display technologies [6,7]. The varied properties of this class of materials will lead to a broadened scope of applications in coming years. Accordingly, processes by which high-quality films of these materials can be deposited while maintaining compatibility with current microelectronics fabrication techniques are of great interest to the materials community. The most universal restraints imposed require that deposition process do not damage underlying structures and materials necessary for the fabrication of microelectronic devices; examples of these restraints are maximum allowed deposition temperatures, avoidance of reagents that produce corrosive byproducts, and limits on ion current and kinetic energy in plasma-based processing.

The goal of this dissertation is to describe advancement in deposition processes for aluminum nitride and gallium nitride that present the ability to deposit higher-quality films on a wider range of substrates than was previously possible. These advances may find relevance in the ever-broadening scope of application of Group III – nitride materials.

1.2 Atomic Layer Deposition and Annealing

As microelectronic devices are scaled to dimensions on the order of tens of atoms rather than tens of microns, precisely controlling deposition processes has become of the utmost importance. This has resulted in the growth of a field known as atomic layer deposition, in which self-limiting surface reactions are used to repeatedly deposit monolayers of material [8]. A schematic of this process is shown in Figure 1.1. Each reaction cycle consists of dosing a precursor and a co-reactant in an alternating fashion with separation between each dose accomplished using a purge of an inert gas. This reaction cycle is repeated until a film of the desired thickness is deposited. In sequence, this first allows the precursor to undergo chemical reaction with the growth surface after which excess precursor and reaction byproducts are swept away by the purge gas. The reactant is then dosed and allowed to react with the layer of atoms deposited by the precursor and the purge gas then sweeps away excess reactant and byproducts of this second reaction. This process typically results in the deposition of smooth and conformal films.

To supply the activation energy needed for these surface reactions to occur, substrates are commonly heated to several hundred degrees Celsius, however the temperature of the substrate must not be so hot as to cause the precursor or co-reactant to desorb or decompose before the surface reaction occurs. Combined, these requirements result in a finite substrate temperature "window" in which an ALD process may occur.

There are many variations of atomic layer deposition, such as plasma-enhanced atomic layer deposition (PE-ALD), in which a plasma-generated species serves as the co-reactant, and atomic layer annealing (ALA), in which an inert plasma treatment follows each deposition cycle [9–12]. These techniques are utilized to deposit films at temperatures lower than what would otherwise be possible and/or to deposit films with enhanced properties.

1.3 Reactive Magnetron Sputtering

Aluminum nitride is commonly deposited by reactive magnetron sputtering. In this process, an aluminum target is attached to a magnetron cathode powered by either a DC or RF power supply [13,14]. The substrate and/or chamber walls serve as the anode. A sputtering gas, commonly argon, and a reactive gas, in this case nitrogen, flow through the chamber in the desired ratio. When a potential is applied to the cathode a plasma is generated, causing ionized species to bombard the target surface and sputter aluminum atoms. Reactive nitrogen species generated in the plasma interact with both surface bound and sputtered aluminum species, which then deposit onto the substrate surface. Continual bombardment of the growth surface with these species results in the formation of dense films that typically adhere well to the underlying substrate.

Parameters such as flow rates, partial pressures, magnetic configuration, applied voltage, applied power, and the distance between the target and substrate influence the characteristics of the deposited film [13–16]. Extensive optimization is needed to produce films with the desired stoichiometry, crystallographic orientation, residual strain, and morphology. In the case of aluminum nitride, chamber cleanliness and integrity are necessary to minimize oxygen contamination.

1.4 Vacuum Chamber System

To deposit films by these techniques, atomic layer deposition, atomic layer annealing, and DC reactive magnetron sputtering, a vacuum chamber system was constructed. A system of in-vacuum transfer arms connects a load lock to a sputtering chamber, an ALD/ALA chamber, and an analytical chamber containing an x-ray photoelectron spectroscopy system. Further details on these chambers are found in the following chapters.

1.5 X-Ray Photoelectron Spectroscopy

To characterize the composition of the deposited films, x-ray photoelectron spectroscopy was utilized. In this technique, an x-ray source is used to generate photoelectrons by irradiating the sample surface with x-rays. An electron energy analyzer, more specifically a double-pass cylindrical mirror analyzer in the case of the experiments reported in this work, is utilized to count the photoelectrons of a given kinetic energy. The binding energy of the photoelectrons is calculated using the equation:

$$KE_{electron} = h\nu_{x-ray} - BE_{electron} - \Phi_{spectrometer}$$

where $\Phi_{spectrometer}$ is the workfunction of the spectrometer. As the binding energy of electrons in each orbital of a given atom are known, this technique can be used to identify the elements present in a material. In practice, the detector is swept over a range of kinetic energies to generate spectra from which the chemistry of the local bonding environment of the corresponding atoms can be deduced based on binding energy shifts. The composition of the sample is determined by calculating the fractional area of peak(s) present in the binding energy region of one orbital type for each element over the sum of area from all analyzed regions. However, due to differing photoelectron yields for every element, these peak areas are first corrected using known Scofield relative sensitivity factors.

1.6 X-Ray Diffraction and Reflectivity

The crystallinity of the deposited films is frequently utilized as a metric to optimize process parameters in the following chapters. Two types of x-ray diffraction were utilized to determine film crystallinity, grazing-incidence x-ray diffraction for thin films (<50 nm) and Bragg-Brentano x-ray diffraction for thicker films (> 50 nm). In both cases, x-rays generated by a rotating copper

anode were directed at the sample and an x-ray detector was swept over a range of angles with respect to the sample surface, theta, by a goniometer. At angles of theta corresponding to inter-planar spacing, the Bragg diffraction condition is fulfilled and the x-rays are coherently scattered such that they are detected. These two techniques differ in the position of the x-ray source: in the grazing-incidence geometry the source is stationary at a small angle, omega, with respect to the sample surface. This allows for a larger interaction area, enhancing diffraction signal from thin films and minimizing signal from the substrate material. In Bragg-Brentano x-ray diffraction, the x-ray source position changes relative to the sample surface at half the rate of the detector. This setup results in diffraction signal from the entirety of the film and even the substrate in certain cases. Additional metrics for process optimization were thickness and density of deposited thin films as determined by x-ray reflectivity profile fitting.

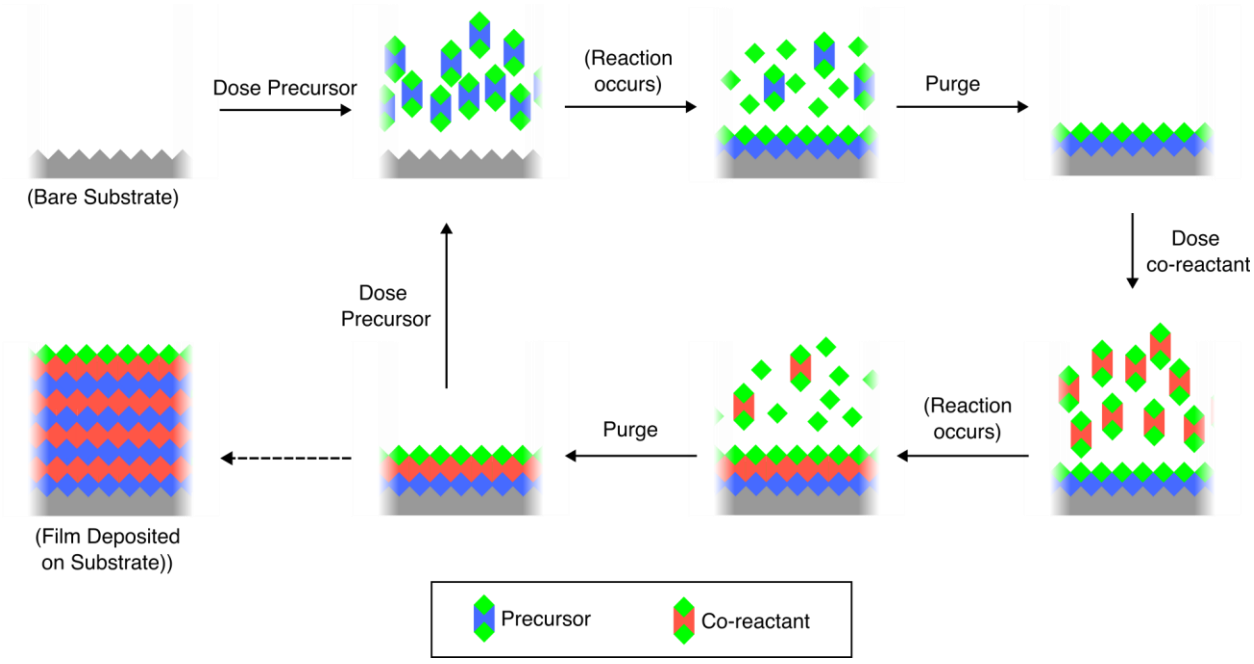

Figure 1.1 Atomic Layer Deposition Schematic. Both precursor and co-reactant in the gas phase are pulsed in an alternating fashion, with separation created using a purge gas. This allows each chemical to react with the growth surface separately while excess and byproducts are purged from the chamber. This process is repeated until a film of the desired thickness is deposited.

1.7 References

[1] M.A. Dubois, P. Muralt, Properties of aluminum nitride thin films for piezoelectric transducers and microwave filter applications, Appl Phys Lett. 74 (1999) 3032–3034. https://doi.org/10.1063/1.124055.

[2] L. La Spina, E. Iborra, H. Schellevis, M. Clement, J. Olivares, L.K. Nanver, Aluminum nitride for heatspreading in RF IC's, Solid State Electron. 52 (2008) 1359–1363. https://doi.org/https://doi.org/10.1016/j.sse.2008.04.009.

[3] Y. Bian, M. Liu, G. Ke, Y. Chen, J. Dibattista, E. Chan, Y. Yang, Surface & Coatings Technology Aluminum nitride thin film growth and applications for heat dissipation, Surf Coat Technol. 267 (2015) 65–69. https://doi.org/10.1016/j.surfcoat.2014.11.060.

[4] H. Amano, Y. Baines, E. Beam, M. Borga, T. Bouchet, P.R. Chalker, M. Charles, K.J. Chen, N. Chowdhury, R. Chu, C. De Santi, M.M. De Souza, S. Decoutere, L. Di Cioccio, B. Eckardt, T. Egawa, P. Fay, J.J. Freedsman, L. Guido, O. Häberlen, G. Haynes, T. Heckel, D. Hemakumara, P. Houston, J. Hu, M. Hua, Q. Huang, A. Huang, S. Jiang, H. Kawai, D. Kinzer, M. Kuball, A. Kumar, K.B. Lee, X. Li, D. Marcon, M. März, R. McCarthy, G. Meneghesso, M. Meneghini, E. Morvan, A. Nakajima, E.M.S. Narayanan, S. Oliver, T. Palacios, D. Piedra, M. Plissonnier, R. Reddy, M. Sun, I. Thayne, A. Torres, N. Trivellin, V. Unni, M.J. Uren, M. Van Hove, D.J. Wallis, J. Wang, J. Xie, S. Yagi, S. Yang, C. Youtsey, R. Yu, E. Zanoni, S. Zeltner, Y. Zhang, The 2018 GaN power electronics roadmap, J Phys D Appl Phys. 51 (2018). https://doi.org/10.1088/1361-6463/aaaf9d.

[5] C.R. Eddy, T.J. Anderson, A.D. Koehler, N. Nepal, D.J. Meyer, M.J. Tadjer, R. Baranyai, J.W. Pomeroy, M. Kuball, T.I. Feygelson, B.B. Pate, M.A. Mastro, J.K. Hite, M.G. Ancona, F.J. Kub, K.D. Hobart, GaN Power Transistors with Integrated Thermal Management, ECS Trans. 58 (2013). https://doi.org/10.1149/05804.0279ecst.

[6] A.R. Anwar, M.T. Sajjad, M.A. Johar, C.A. Hernández-Gutiérrez, M. Usman, S.P. Łepkowski, Recent Progress in Micro-LED-Based Display Technologies, Laser Photon Rev. 16 (2022). https://doi.org/10.1002/lpor.202100427.

[7] A.C. Liu, K.J. Singh, Y.M. Huang, T. Ahmed, F.J. Liou, Y.H. Liou, C.C. Ting, C.C. Lin, Y. Li, S. Samukawa, H.C. Kuo, Increase in the Efficiency of III-Nitride Micro-LEDs: Atomic-Layer Deposition and Etching, IEEE Nanotechnol Mag. 15 (2021) 18–34. https://doi.org/10.1109/MNANO.2021.3066393.

[8] S.M. George, Atomic layer deposition: An overview, Chem Rev. 110 (2010) 111–131. https://doi.org/10.1021/cr900056b.

[9] M. Legallais, H. Mehdi, S. David, F. Bassani, S. Labau, B. Pelissier, T. Baron, E. Martinez, G. Ghibaudo, B. Salem, Improvement of AlN Film Quality Using Plasma Enhanced Atomic

Layer Deposition with Substrate Biasing, ACS Appl Mater Interfaces. 12 (2020). https://doi.org/10.1021/acsami.0c10515.

[10] S.T. Ueda, A. McLeod, D. Alvarez, D. Moser, R. Kanjolia, M. Moinpour, J. Woodruff, A.C. Kummel, Tris(dimethylamido)aluminum(III) and N2H4: Ideal precursors for the low-temperature deposition of large grain, oriented c-axis AlN on Si via atomic layer annealing, Appl Surf Sci. 554 (2021). https://doi.org/10.1016/j.apsusc.2021.149656.

[11] H.Y. Shih, W.H. Lee, W.C. Kao, Y.C. Chuang, R.M. Lin, H.C. Lin, M. Shiojiri, M.J. Chen, Low-temperature atomic layer epitaxy of AlN ultrathin films by layer-by-layer, in-situ atomic layer annealing, Sci Rep. 7 (2017). https://doi.org/10.1038/srep39717.

[12] S.T. Ueda, A. McLeod, Y. Jo, Z. Zhang, J. Spiegelman, J. Spiegelman, D. Alvarez, D. Moser, R. Kanjolia, M. Moinpour, J. Woodruff, K. Cho, A.C. Kummel, Experimental and theoretical determination of the role of ions in atomic layer annealing, J Mater Chem C Mater. (2022). https://doi.org/10.1039/D1TC05194F.

[13] W.D. Sproul, D.J. Christie, D.C. Carter, Control of reactive sputtering processes, Thin Solid Films. 491 (2005) 1–17. https://doi.org/10.1016/j.tsf.2005.05.022.

[14] R.L. Xu, M. Munõz Rojo, S.M. Islam, A. Sood, B. Vareskic, A. Katre, N. Mingo, K.E. Goodson, H.G. Xing, D. Jena, E. Pop, Thermal conductivity of crystalline AlN and the influence of atomic-scale defects, J Appl Phys. 126 (2019). https://doi.org/10.1063/1.5097172.

[15] H. Okano, Y. Takashi, T. Tanaka, K. Shibata, S. Nakano, Preparation of c-Axis Oriented AlN Thin Films by Low-Temperature Reactive Sputtering, Jpn J Appl Phys. 31 (1992) 3446–3451.

[16] T. Kumada, M. Ohtsuka, H. Fukuyama, Influence of substrate temperature on the crystalline quality of AlN layers deposited by RF reactive magnetron sputtering, AIP Adv. 5 (2015). https://doi.org/10.1063/1.4906796.

CHAPTER 2

Pulsed Chemical Vapor Deposition for Crystalline Aluminum Nitride Thin Films and Buffer Layers on Silicon and Silicon Carbide

2.1 Abstract:

Low temperature aluminum nitride (AlN) deposition has applications ranging from serving as a heat spreading material to serving as a buffer layer for III-V semiconductors on silicon or silicon carbide (SiC) for radio frequency, power, and microLED devices. While crystalline AlN is traditionally deposited at high temperature (>800 ˚C), in the present study AlN is deposited on Si(100), Si(111), and 4H-SiC substrates by two modest temperature processes using a metal precursor with high thermal stability, tris(dimethylamido) aluminum, and a highly reactive nitrogen source, anhydrous hydrazine. A 580 ˚C pulsed chemical vapor deposition (CVD) process is compared to a more complex 400 ˚C atomic layer annealing process, in which the same precursors are utilized with periodic ion bombardment to induce film crystallinity. Films deposited by both processes template preferential c-axis orientation in subsequently sputtered AlN on unheated substrates. Both templating techniques demonstrate equivalent enhancements in crystallinity of the sputtered AlN relative to a non-templated sputtered film by x-ray diffraction and transmission electron microscopy studies. On 4H-SiC substrates, a comparison of sputtering directly and templating with the 580 ˚C pulsed CVD process reveals epitaxial deposition by the 580 ˚C pulsed CVD process which extends into the low temperature sputtered AlN.

2.2 Introduction:

Aluminum nitride (AlN) is a promising material due to its high thermal conductivity and close lattice match to gallium nitride (GaN) and indium gallium nitride (InGaN). Accordingly, AlN may find application as a heat spreading material and/or as a buffer layer material. [1–7] Deposition methods for crystalline aluminum nitride typically require temperatures exceeding 800 ˚C, such as metal organic chemical vapor deposition (MOCVD) and molecular beam epitaxy (MBE); this presents barriers to integration in back-end-of-line processing. [8–10] For application of AlN as a buffer layer for the growth of GaN and InGaN on silicon (Si) and silicon carbide (SiC), high-quality crystalline AlN films with c-axis orientation are necessary. [7,11,12] Deposition methods at comparatively lower temperatures (~350 ˚C), such as plasma-enhanced ALD (PE-ALD) and atomic layer annealing (ALA), can be used to deposit crystalline or polycrystalline AlN with less strain than films deposited at higher temperatures; however, PE-ALD produces non-stoichiometric AlN films that are often nano-crystalline. [13–15] Atomic layer annealing has recently drawn attention for low temperature deposition of crystalline or polycrystalline AlN, however its practical utility is limited by low deposition rates due to lengthy ion bombardment treatments and the relative complexity of required deposition tools. [16,17]

Trimethyl aluminum (TMA) is a common precursor for many deposition methods despite its thermal decomposition at temperatures above 350 ˚C; this often results in films with substantial carbon contamination and nitrogen poor stoichiometry. [18–20] Tris(dimethylamido) aluminum (TDMAA) and related tris(diethylamido) aluminum (TDEAA) have shown recent promise for higher-temperature deposition, enabling deposition of AlN with minimal contamination to be deposited by ALD and ALA at temperatures above 350˚C. [18,21,22] This work demonstrates the use of tris(dimethylamido) aluminum (TDMAA) at 400 ˚C and 580 ˚C to deposit AlN by a pulsed

chemical vapor deposition (CVD) method on non-lattice matched (Si) substrates and lattice-matched (SiC) substrates in a homebuilt deposition chamber with growth rates up to ~45 nm/hour. At 400 ˚C substrate temperature, the films are nanocrystalline with random crystallite orientation, while at 580 ˚C the films show growth of columnar grains. Films produced by the pulsed CVD method at 580 ˚C are demonstrated to template preferential c-axis orientation in additional AlN deposited by reactive sputtering and are compared to sputtered AlN on a template layer deposited by ALA at 400 ˚C. Both films show a similar result in enhancing AlN (002) orientation. On 4H-SiC, epitaxy is observed by the 580 ˚C pulsed CVD method, which greatly enhances the crystallinity of low temperature (< 100 ˚C) sputtered material when used as a templating layer.

2.3 Materials and Methods:

2.3.1 Substrates and Preparations

Silicon wafers with (100) and (111) orientations were obtained from WaferWorld. Silicon carbide wafers of 4H polymorph with a 4˚ off-c-axis cut were obtained from El Cat, Inc. Substrate coupons were degreased using acetone, methanol, and water (Fisher Scientific) and stripped of native oxide by a three-step cyclic etch in 2% HF in deionized water (VWR). Tris(dimethylamido) aluminum was supplied by EMD Performance Materials; anhydrous hydrazine was supplied by RASIRC.

2.3.2 Chemical Vapor Deposition System

The pulsed CVD was performed in a homebuilt vacuum chamber (walls heated to 90 ˚C, base pressure $<1x10^{-4}$ Pa) pumped by an Edwards EPX 500 NE high vacuum pump with an in-line liquid nitrogen trap. A tool schematic is shown in Figure 2.1. The deposition chamber is

attached to two additional vacuum chambers through an in-vacuum transfer system: the first containing a sputtering system and the second containing an x-ray photoelectron spectroscopy system.

The pulsed CVD process was performed at substrate temperatures of 400 ˚C and 580 ˚C. The TDMAA precursor container was heated to 105 ˚C for deposition and held at 85 ˚C for storage. All precursor dosing was controlled by a LabView system and was performed in a manner consistent with ALD: the precursors were pulsed in an alternating fashion separated by brief periods of pumping. The process is denoted as pulsed CVD because the TDMAA precursor did not display self-limiting growth, as is characteristic of ALD processes, for the short pulse times utilized in this study. Similar behavior has been observed for the deposition of AlN using TDMAA and NH_3. [23] Both precursor containers were pressurized with Ar prior to dosing; trace water and oxygen were removed from the Ar push gas using an Entegris GateKeeper purifier. The pulse times used for 400 ˚C and 580 ˚C deposition are shown in Table 1.1 and were previously optimized to achieve 1.2 – 1.5 Ang./cyc. growth rates. [22]

2.3.3 Deposited Thin Films and CVD-Templated Sputtered Films

Table 2.2 describe the samples deposited for the three studies performed in this paper. An initial set of thin films with 40 nm target thickness were deposited by pulsed CVD on Si(111) and Si(100) at 400 ˚C and 580 ˚C to evaluate the effects of lattice mismatch and substrate temperature. A second set of depositions was performed on Si(111) to analyze the templating ability of the 580 ˚C pulsed CVD relative to a previously reported ALA technique using Ar ions bombardment at -25 V DC substrate bias: a 20-30 nm template layer by either method was first deposited followed by 150-170 nm of sputtered AlN. [22] These two templated films are compared to a reference 190

nm AlN sputtered film deposited directly onto Si(111). A third set of depositions compares the effectiveness the 580 ˚C pulsed CVD template layers on 4H-SiC to a reference sputtered film; 20 nm and 40 nm template layers were deposited and all samples were brought to a total thickness of 190 nm by reactive sputtering. For all templated samples layer thicknesses are approximate and were based on observed growth rates. Reactive sputtering was performed using a 69% N_2/31% Ar gas mixture (Praxair and AirGas, >99.999%) in a balanced magnetron configuration (Kurt J. Lesker Torus MagKeeper, >99.99% purity Al target) with 100 W DC power operating at 0.43 Pa as measured by a capacitance manometer (Kurt J. Lesker Co.). Samples were not actively heated during sputter deposition, however a thermocouple mounted on the sputtering stage showed increases from 20 ˚C to 70-80 ˚C following deposition.

The surface composition of the films was determined by x-ray photoelectron spectroscopy (STAIB Instruments DESA 150 CMA, Mg Kα source) of the Al 2p, N 1s, C 1s, O 1s and Si 2p regions. Peak fitting (CASA XPS) was performed using a Shirley background profile and elemental composition was corrected using Scofield relative sensitivity factors. All photoelectron spectra were referenced to adventitious carbon at 284.8 eV.

2.3.4 Characterization

For all film depositions on Si(111) and Si(100), grazing incidence x-ray diffraction (GI-XRD) was performed to analyze film crystallinity and preferred orientation (Rigaku SmartLab, Cu anode operating at 2 kW, parallel beam configuration, fixed 1.005˚ incidence angle). X-ray reflectivity measurements of the thin film samples from 0-3˚ 2θ were performed on the same instrument and were modeled using Rigaku GlobalFit software to determine film thickness and density. Bragg-Brentano x-ray diffraction was used for films deposited on SiC due to its

comparatively lower instrumental broadening; this allowed for resolution of AlN and SiC diffraction peaks that are not easily resolved in GI-XRD.

Four types of transmission electron microscopy (TEM) were performed: bright filed (BF-TEM), dark field (DF-TEM), scanning (STEM), and high-resolution (HR-TEM). Selected area electron diffraction (SAED) was also performed for films on SiC. All lamellae were prepared using a focused ion beam (FIB) milling system with thinning to approximately 40 nm by Covalent Metrology (Sunnyvale, CA). All TEM, STEM, and SAED was performed using a ThermoFisher Talos F200X G2 transmission electron microscope.

2.4 Results and Discussion:

2.4.1 Thin Films

Representative composition data as determined by XPS is shown in Figure 2.2 for pulsed CVD thin film depositions at 400 ˚C and 580 ˚C on Si(111). At both substrate deposition temperatures, nearly 1:1 stoichiometric Al:N is observed with minimal oxygen and carbon content. The composition information reflects the composition of the top 3-5 nm of the AlN films. In-vacuum transfer of the substrates through the load lock after deposition may result in slight oxidation of the AlN surface, meaning bulk oxygen content is also likely lower than is the surface composition determined by XPS and shown in Figure 2.2.

Photoelectron spectra and corresponding peak fits used for the determination of film composition of these samples are shown in Figure 2.3. The Al 2p regions in Figure 2.3 (a) and (e) are fitted with a spin orbit split binding energy difference of 0.4 eV. The C 1s x-ray photoelectron spectra in Figure 2.3 (d) and (h) indicate adventitious hydrocarbon contamination of the film surfaces due to the presence of peaks at 284.8 eV, 287.3 eV, and 288.5 eV, corresponding to C-C,

C-O, and C=O bonds. At both deposition temperatures, no low binding energy peak is observed in the C 1s region indicating the absence of Al-C bonds. These observations suggest that the carbon content in the bulk of these films is likely lower than is observed on the film surface. This low carbon contamination is consistent with previous reports of TDMAA used for deposition of AlN and AlO_x and is attributed to the lack of Al-C bonds in the precursor structure. [21]

Note the N 1s spectra are fit using two peaks, as is customary in XPS characterization of aluminum nitride films; the main nitride peak is located at 397.0 eV and the higher binding energy peak at 398.8 eV corresponds to O-Al-N bonds likely present on the oxidized film surface. [24] It is commonly reported that the charge-balanced sum of nitrogen and oxygen content should equal that of aluminum. [24] While the stoichiometry of the bulk AlN was not measured (e.g., by depth profiling XPS), it is likely that the concentration of oxygen and nitrogen in the bulk of the films may equal that of aluminum and the films are, therefore, stoichiometric.

Results from the grazing-incidence x-ray diffraction study are shown in Figure 2.4; Table 2.3 lists the corresponding film thickness and density values, as determined by XRR, and AlN (002) peak full-width at half maximum (FWHM) as determined by GI-XRD. Polycrystallinity with preferential c-axis orientation is observed on both substrates at 580 ˚C whereas deposition at 400 ˚C is nanocrystalline on Si(111) and amorphous on Si(100). On Si (111) (Figure 2.4a), crystallinity is observed at 580 ˚C with a preferred AlN (002) orientation, whereas at 400 ˚C minimal diffraction signal is observed at the AlN (100) peak position. The full-width at half maximum intensity (FWHM) of the AlN (002) peak on the 580 ˚C film is 0.73˚ at a position of 36.2˚ relative to a theoretical position of 36.1˚. This may indicate that strain is present in the film, likely due to deposition on a non-lattice matched substrate. On Si (100) (Figure 2.4b), similar crystallinity is observed at 580 ˚C with an AlN (002) peak of 0.75˚ FWHM at an angle of 36.1˚. When depositing

at 400 ˚C substrate temperature on Si (100), no crystallinity is detected. The XRR measurement and fit profiles for each film are shown in Figure 2.5. The decrease in signal observed beyond 1.5˚ 2θ for the films deposited at 580 ˚C substrate temperature may be due to increased surface roughness, consistent with the growth of larger crystallites.

As listed in Table 2.3, the films deposited at 580 ˚C have greater density than their 400 ˚C counterparts, with increases of 8.4% and 17.6% observed for the films on Si (111) and Si (100), respectively. It is noted that the largest film density observed, 3.11 g/cm^3 for the film deposited at 580 ˚C on Si (111), is still less than that of bulk AlN at 3.26 g/cm^3. This is likely due to the presence of amorphous material at grain boundaries and at the Si-AlN interface.

The data in Figure 2.4, Figure 2.5, and Table 2.3 demonstrates that moderate increases in substrate temperature during pulsed CVD, such as increasing from 400 ˚C to 580 ˚C, can aid in developing crystalline structure on non-lattice matched substrates. The average crystallite size for any one condition is not limited by thickness as all films with observed crystallinity are of comparable thickness. The differences in crystallinity on Si (111) and Si (100) are consistent with the hexagonal wurtzite structure of aluminum nitride having a closer lattice match to the Si (111) face rather than the Si (100) face. [25]

These GI-XRD results are complemented by the electron microscopy and diffraction studies of the thin films deposited at 400 ˚C and 580 ˚C, shown in Figure 2.6. Bright field TEM for these films is shown in panels (a) and (b), respectively. In the micrograph of the film deposited by pulsed CVD at 400 ˚C, a nanocrystalline film with randomly oriented grains of ~5 nm diameter is observed. In contrast, the film deposited at 580 ˚C shows crystallites coalescing and taking on a columnar structure in which the crystallite diameter increases as a function of film thickness. These observations are confirmed by aperture-based dark field TEM used to highlight separate

crystallites, shown in Figures 2.6 (b) and (c). The 400 ˚C film appears nanocrystalline with rare instances of columnar grains. At 580 ˚C, the columnar grain structure noted in bright field TEM is observed across the entire film as is evidenced by the diffraction of several columnar crystallites. When considering the GI-XRD, XRR, BF-TEM, and DF-TEM results altogether, it is evident that the 580 ˚C pulsed CVD process deposits films with superior crystallinity and more ordered grain structure than those deposited by the 400 ˚C process.

2.4.2 Templated Sputtered Films on Si(111)

For AlN to be utilized as a buffer layer for the growth of GaN and InGaN on silicon and silicon carbide, goals of the RF and microLED industries, thicker layers with c-axis orientation are necessary. In Figure 2.7, two samples of 181-196 nm total thickness are compared by STEM and GI-XRD: the first is a 31 nm layer of AlN deposited using the 580 ˚C pulsed CVD process to template 150 nm of sputtered AlN (red in GI-XRD); the second is a templated film comprised of an initial 21 nm layer of AlN deposited using ALA at 400 ˚C substrate temperature with 175 nm of sputtered AlN deposited on top (blue in GI-XRD); note the substrate temperature is below 100 ˚C during the sputtering process. ALA was performed using a 20 s ion bombardment at the end of each precursor dosing cycle, with Ar ions generated by an inductively coupled plasma source. For this ion bombardment process, the substrate was biased to -25V_{DC} to accelerate the ions toward the growth surface to crystallize the material. Experimental details can be found in previous works. [22,26] These two templated films are also compared to a reference film of 190 nm sputtered AlN on Si(111) by GI-XRD (black line in GI-XRD comparison). AlN deposited by this sputtering condition showed 49.4 at.% Al, 42.5 at.% N, 5.1 at.% O, and 3.1 at.% C composition by XPS.

The GI-XRD comparison inset (Figure 2.7) shows that AlN (002) orientation is strongly preferred when the sputtering is performed on either the 580 ˚C pulsed-CVD or 400 ˚C ALA templating layer, both with AlN (002) FWHM of 0.64˚. The sputtered reference film has an AlN (002) FWHM of 0.79˚ and shows mixed AlN (002) and AlN (103) orientation which is not desirable for the intended applications. The increase in preferential AlN (002) orientation is likely the result of local domain epitaxy across the template-sputtered interface, as both the 580 ˚C pulsed CVD process and 400 ˚C ALA process have been shown to deposit films with AlN (002) orientation. [22] These results highlight that a templating layer deposited by pulsed CVD can be as effective as a templating layer deposited by the more complex ALA process in increasing the crystallinity of sputtered AlN.

2.4.3 Templated Sputtered Films on SiC

The crystallinity of sputtered material on 4H-SiC is also enhanced when grown on template layers deposited by the 580 ˚C pulsed CVD process. Shown in Figure 2.8 is a Bragg-Brentano XRD comparison: the first film is comprised of 190 nm of AlN sputtered directly onto 4H-SiC, the second and third films are comprised of 20 nm and 40 nm of AlN deposited by the 580 ˚C pulsed CVD process which were brought to a total thickness of 190 nm with sputtered AlN. Relative to the reference sputtered film with 0.38˚ FWHM, the 20 nm and 40 nm templated films show drastically sharper peaks at 0.17˚ and 0.18˚ FWHM, respectively, indicating superior crystallinity of the templated films. This increase in crystallinity is particularly notable since the sample temperature during sputtering was below 100 ˚C.

The efficacy of the pulsed CVD templating layers on SiC are made clear by the TEM, SAED, and HR-TEM shown in Figure 2.9. The 20 nm template layer deposited by the 580 ˚C

CVD process is shown in Figure 2.9 (a). This CVD layer is grown epitaxially, as is demonstrated by the SAED pattern in Figure 2.9 (b), which shows a single crystal-like pattern, and the HR-TEM shown in Figure 2.9 (c), where the lattice fringes of the SiC and AlN appear regularly spaced and uninterrupted. In comparison, TEM of the directly sputtered film in Figure 2.9d reveals an initial amorphous layer of ~3-4 nm thickness. Additionally, the SAED pattern shown in Figure 2.9e reveals diffraction rings from a film of polycrystalline nature columnar grains at various tilt angles relative to the SiC diffraction pattern. The HR-TEM, Figure 2.9 (f), of this film more clearly shows this initial amorphous region, with crystallites developing quickly thereafter.

Further analysis of the epitaxial relationship of the CVD-templated sputtered film shown in Figure 2.9 (a) is shown in Figure 2.10. Fast Fourier transform (FFT) analysis was performed from the HR-TEM image for five ~10 nm x 10 nm regions each of the substrate (I-V), the CVD layer (VI-X), and the sputtered layer (XI-XV). Each of the FFT regions shows the expected pattem for the 4H-SiC and AlN wurtzite structures, with matching orientation along the c-axis. This indicates that the epitaxial relationship observed between the SiC substrate and the CVD AlN layer creates long-range order and effectively templates the sputtered AlN layer.

The epitaxial growth of the 580 ˚C CVD template layer may be the result of comparatively greater adatom mobility on the growth surface due to the considerably higher substrate temperature and slower growth rate. In comparison, the initial amorphous region of the directly sputtered film may be the result of the combined higher deposition rate and a comparatively colder initial growth surface as the SiC substrate was not actively heated during sputtering. These effects likely resulted in constrained surface adatom mobility. For films deposited on SiC, these XRD, TEM, and SAED results demonstrate that the enhancement mechanism of the sputtered material is not a function of

the CVD template layer thickness, but rather is the result of sputtering AlN onto a highly crystalline and lattice-matched CVD template layer.

2.5 Conclusions:

These results demonstrate that a 580 ˚C pulsed CVD process for aluminum nitride is a viable alternative to more complex techniques such as atomic layer annealing and techniques requiring substantially greater substrate temperatures, such as MBE and MOCVD. Using tris(dimethylamido) aluminum and anhydrous hydrazine, crystalline films with low oxygen and carbon content can be achieved at temperatures as low as 400 ˚C, though substantially improvement in crystallinity and density is observed at 580 ˚C. When performed on SiC substrates, the 580 ˚C process demonstrates an epitaxial relationship with the substrate and forms a single crystal; this greatly enhances the crystallinity of reactively sputtered AlN with no active substrate heating. This technique may find use for the growth of crystalline AlN buffer layers for GaN and InGaN on silicon and silicon carbide, enabling a decrease in substrate costs for RF power electronics and for thermally conductive buffer layers for microLED devices.

2.6 Acknowledgements:

This work was supported in part by the Applications and Systems-Driven Center for Energy Efficient Integrated Nano Technologies (ASCENT), one of six centers in the Joint University Microelectronics Program (JUMP), an SRC program sponsored by the Defense Advanced Research Program Agency (DARPA). This work was performed in part at the San Diego Nanotechnology Infrastructure (SDNI) at UC San Diego, a member of the National Nanotechnology Coordinate Infrastructure, which is supported by the National Science Foundation (ECCS-1542148). The authors would like to thank EMD Performance Materials and Rasirc Matheson for supplying precursors.

Chapter 2, in full, is a reprint of the material as it appears in the following publication, of which the dissertation author was the primary researcher and author:

McLeod, Aaron J.; Ueda, Scott T.; Lee, Ping Che; Spiegelman, Jeff; Kanjolia, Ravindra; Moinpour, Mansour; Woodruff, Jacob; Kummel, Andrew C. "Pulsed Chemical Vapor Deposition for Crystalline Aluminum Nitride Thin Films and Buffer Layers on Silicon and Silicon Carbide", Thin Solid Films, vol. 768, 2023.

Table 2.1 Pulsed CVD Dosing Conditions at 400 ˚C and 580 ˚C. Dosing times and pump times for the TDMAA and N_2H_4 precursors at the 400 ˚C and 580 ˚C substrate temperature conditions.

	400 ˚C	580 ˚C
TDMAA Dose	150 ms	90 ms
Post-TDMAA Pump	4 s	4 s
N_2H_4 Dose	100 ms	80 ms
Post-N_2H_4 Pump	8 s	8 s

Table 2.1 List of Sample Depositions and Deposition Methods. Three sets of samples for comparisons in this chapter deposited by various techniques. Thicknesses of thin films were measured by XRR, while those for templated films were measured in TEM and estimated based on growth rates for the films on Si(111) and 4H-SiC, respectively.

Comparison Set	Sample Description	Substrate	Thin Film or Template Layer Thickness (nm)	Sputtered Layer Thickness (nm)
Thin Films	400 ˚C Pulsed CVD	Si (111)	44.6	N/A
		Si (100)	41.3	
	580 ˚C Pulsed CVD	Si (111)	43.8	
		Si (100)	44.6	
Templated Films on Si(111)	580 ˚C Pulsed CVD	Si (111)	31	~150
	400 ˚C ALA, Ar -25V DC		21	~175
	Sputtered Reference		N/A	~190
Templated Films on 4H-SiC	580 ˚C Pulsed CVD	4H-SiC	~20	~170
			~40	~150
	Sputtered Reference		N/A	~190

Table 2.2 Thin Film Properties for Pulsed CVD AlN. Substrate and deposition temperature for thin films deposited at 400 ˚C and 580 ˚C alongside thickness and density as measured by XRR and the AlN (002) diffraction peak FWHM and position measured using GI-XRD.

Substrate	Deposition Temperature (˚C)	Thickness (nm)	Density (g/cm^3)	AlN (002) FWHM (deg.)	AlN (002) Peak Position (deg.)
Si (111)	400	44.6	2.86	N/A	N/A
	580	43.8	3.11	0.73	36.2˚
Si (100)	400	41.3	2.59	N/A	N/A
	580	44.6	3.09	0.75	36.1˚

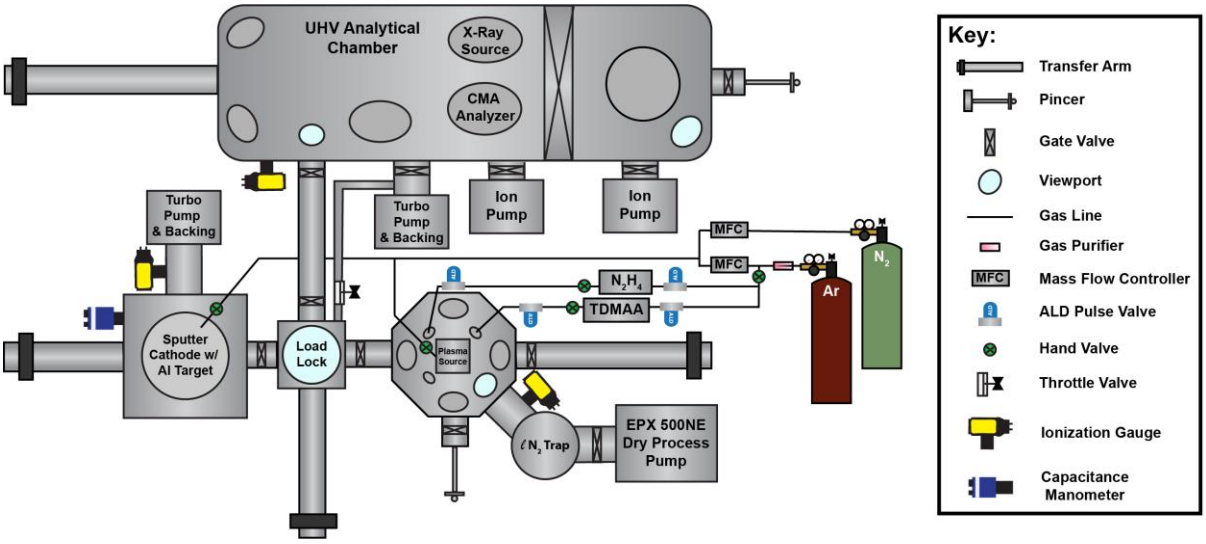

Figure 2.1 Chamber Schematic Diagram. Chamber schematic showing separate pulsed CVD and ALA chamber (bottom right), sputtering chamber (bottom left), and analytical chamber (top) linked through an in-vacuum transfer system.

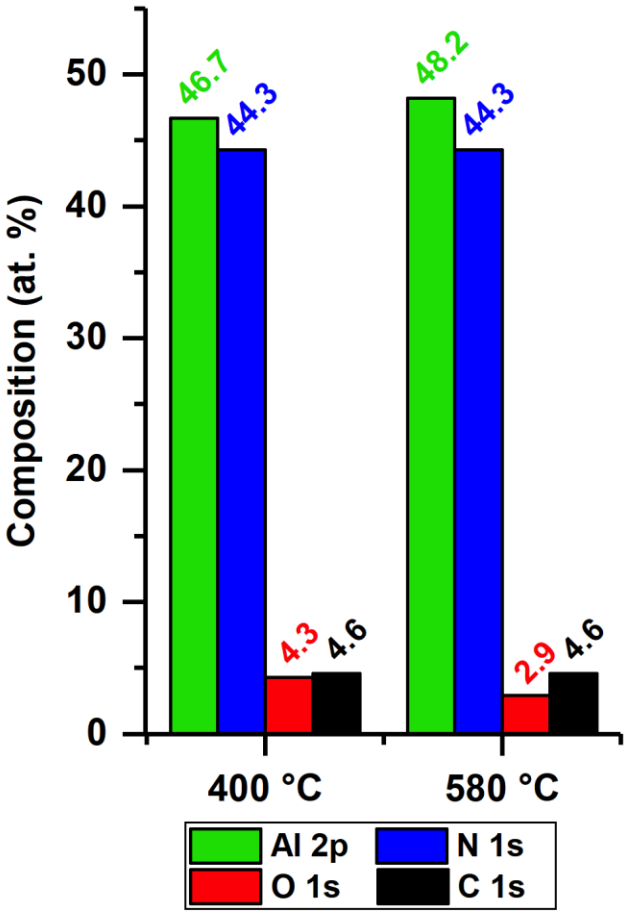

Figure 2.2 Composition of Pulsed CVD AlN vs Temperature. Film composition data for pulsed CVD at substrate temperatures of 400 ˚C (44.9 nm thick) and 580 ˚C (43.8 nm thick) on Si(111) as determined by XPS. Note, these are surface compositions and bulk contaminants may be lower.

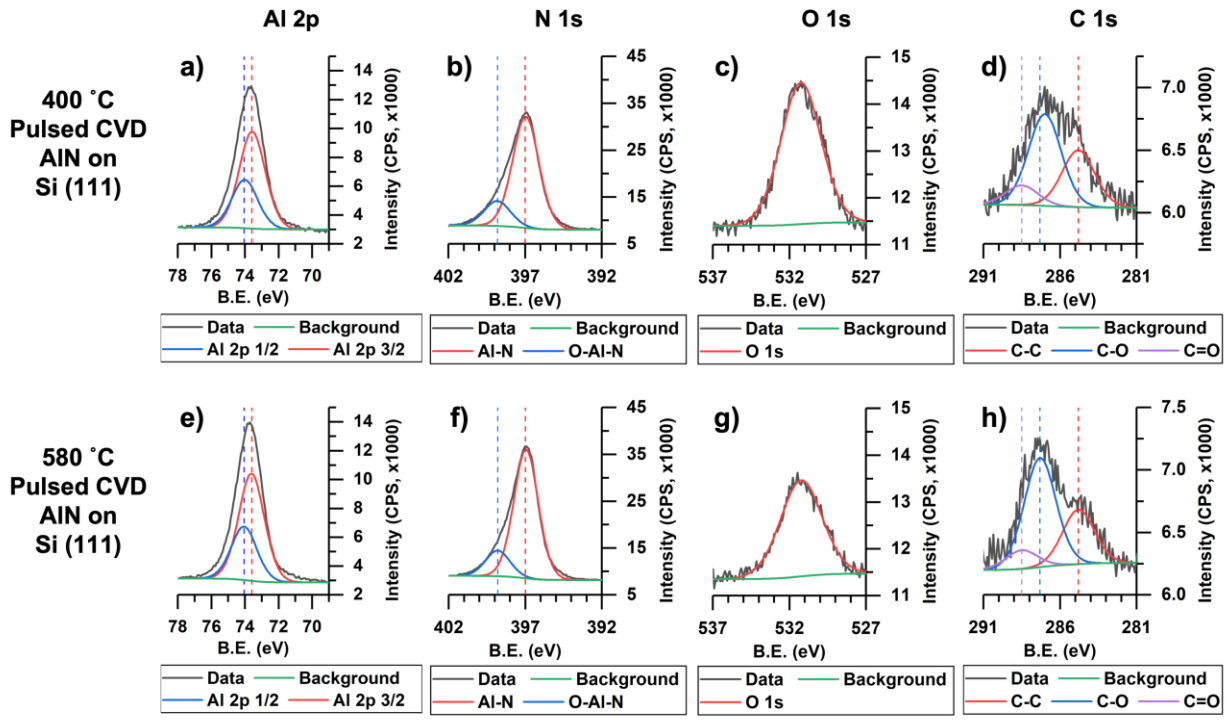

Figure 2.3 High Resolution X-Ray Photoelectron Spectra. X-Ray photoelectron spectra of the Al 2p, N 1s, O 1s, and C 1s regions for films deposited by (a-d) the 400 ˚C and (e-h) 580 ˚C pulsed CVD AlN processes on Si(111).

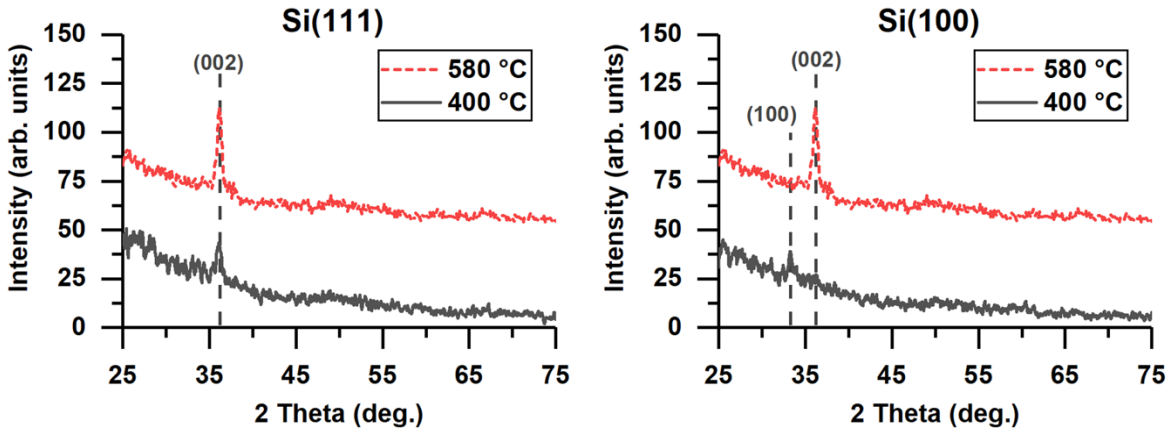

Figure 2.4 Crystallinity Analysis for Pulsed CVD AlN vs Temperature. Crystallinity Analysis for Pulsed CVD AlN vs Temperature. GI-XRD patterns for AlN films deposited at 400 ˚C and 580 ˚C by pulsed CVD on Si (111), left, and Si (100), right.

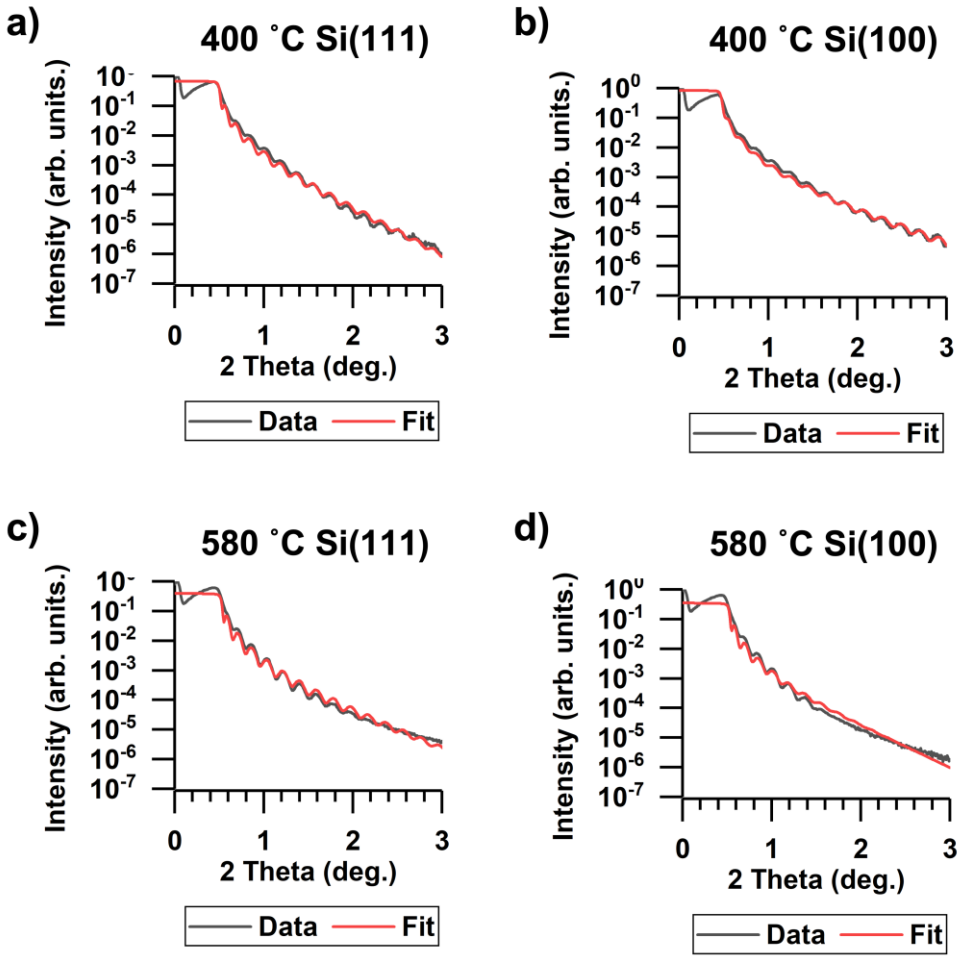

Figure 2.5 X-Ray Reflectivity Measurement and Fit Profiles. X-Ray reflectivity profiles for the films deposited at 400 ˚C on Si (111) and Si (100), and at 580 ˚C on Si (111) and Si(100), panels (a), (b), (c), and (d), respectively.

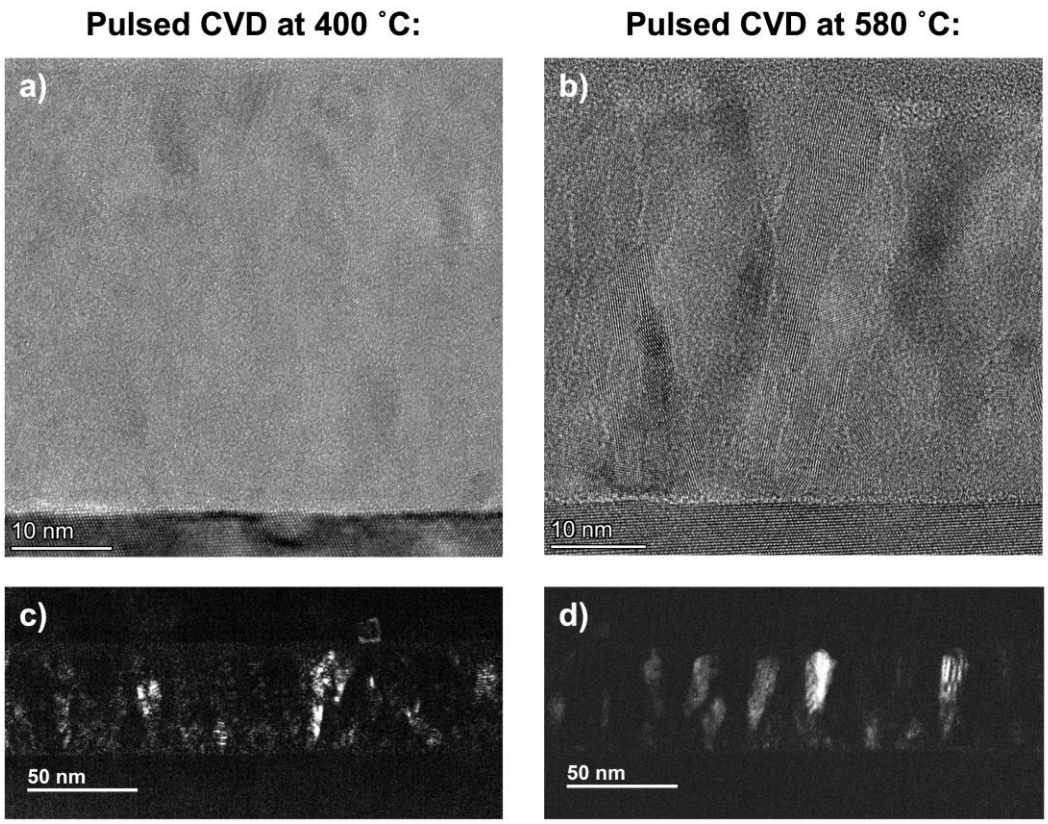

Figure 2.1 BF-TEM and DF-TEM of pulsed CVD films on Si (111). BF-TEM (top) and DF-TEM (bottom) of pulsed CVD films deposited on Si (111) at (a,c) 400 ˚C and (b,d) at 580 ˚C.

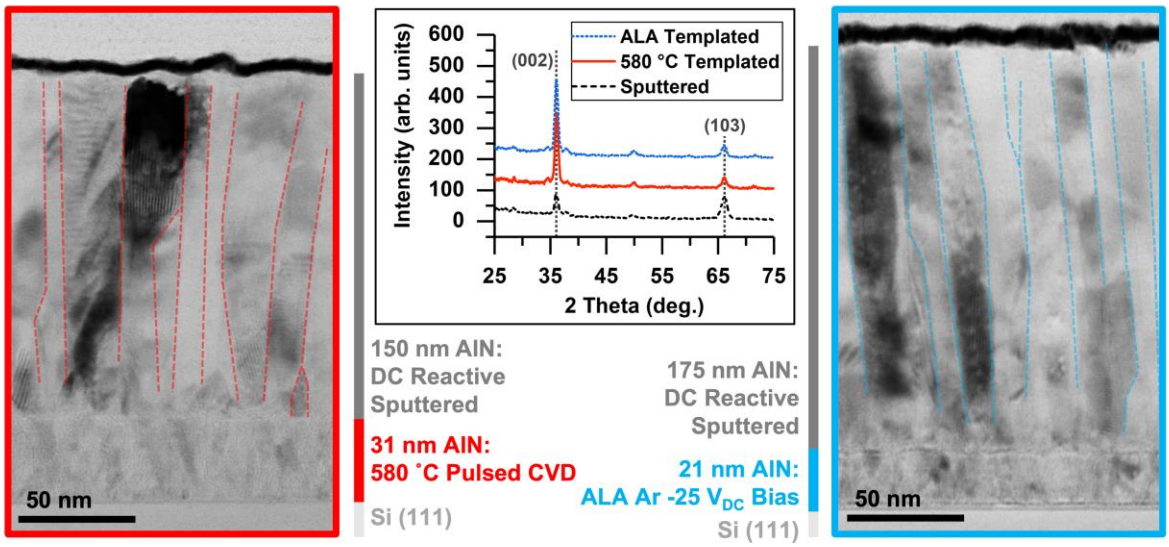

Figure 2.2 STEM Comparison of 580 ˚C CVD and 400 ˚C ALA Templated Films and GI-XRD Comparisons. STEM Comparison of grain structure by STEM in 580 ˚C pulsed CVD-templated sputtered AlN (left) and 400 ˚C ALA-templated sputtered AlN (right) on Si(111). Grain boundaries are manually traced in the top sputtered layer to visually aid in comparison.

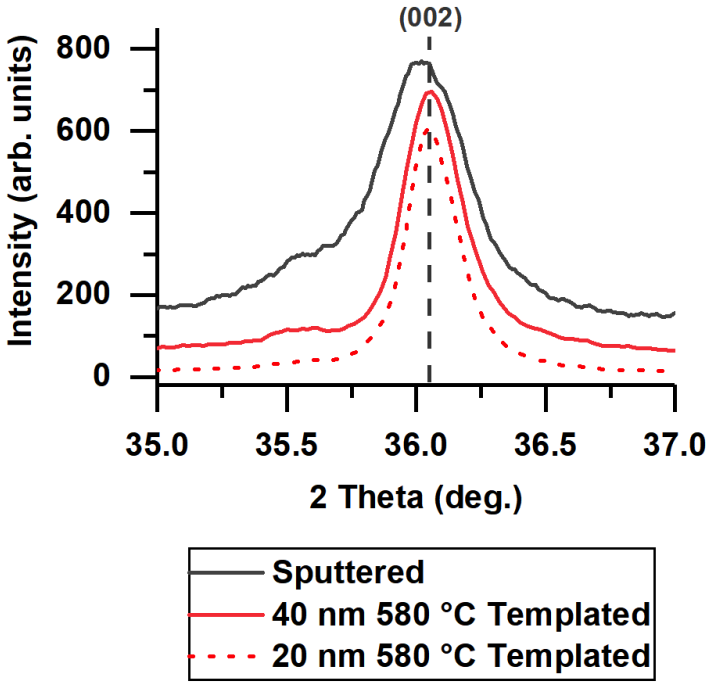

Figure 2.3 Bragg-Brentano XRD comparison of the AlN (002) diffraction peaks of three films on 4H-SiC with 190 nm total thickness. Bragg-Brentano XRD patterns of the AlN (002) diffraction peaks of three films on 4H-SiC with 190 nm total thickness. The first film is an entirely sputtered film with 0.38˚ FWHM; the second and third films are composed of 20 nm and 40 nm 580 ˚C pulsed CVD template layers followed by 170 nm and 150 nm of sputtered material, respectively. The second and third films have FWHM of 0.17˚ and 0.18˚ respectively.

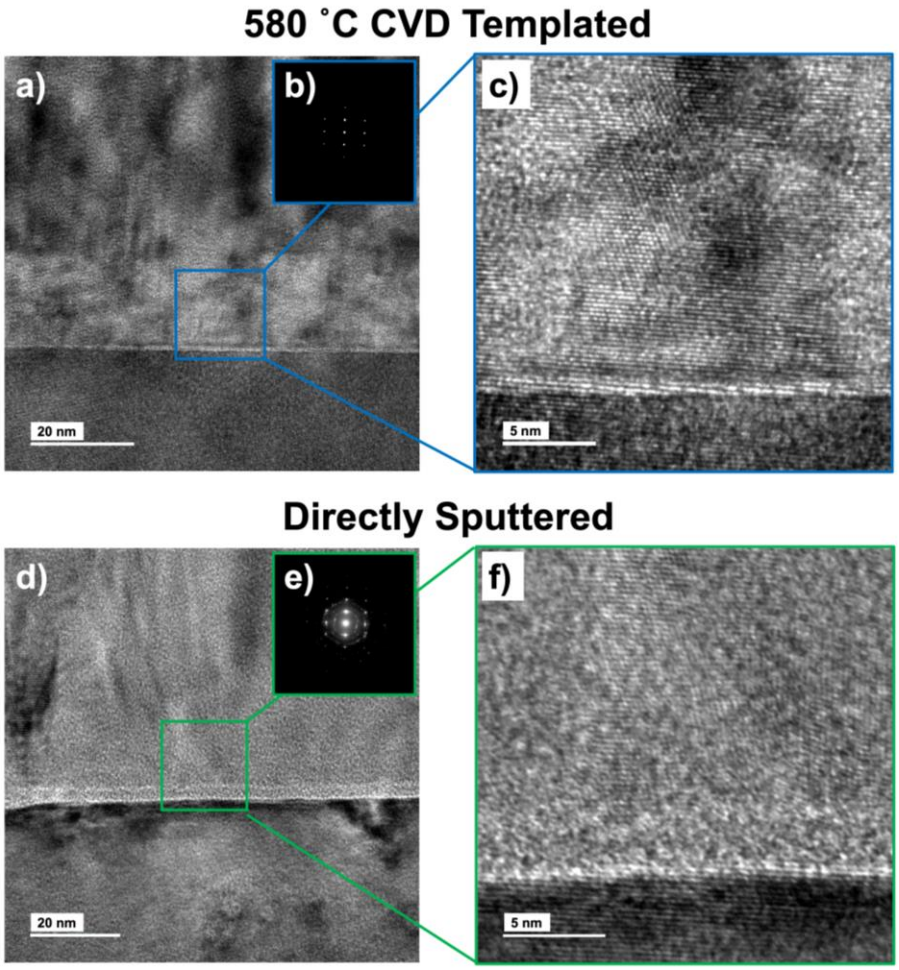

Figure 2.4 Electron Microscopy Comparisons of a 580 ˚C Pulsed CVD Templated Film and a Directly Sputtered Film on SiC Substrates. TEM, selected area electron diffraction, and HR-TEM, respectively, of the 20 nm 580 ˚C CVD templated film (a,b,c) and the directly sputtered film (d,e,f) on 4H-SiC substrates.

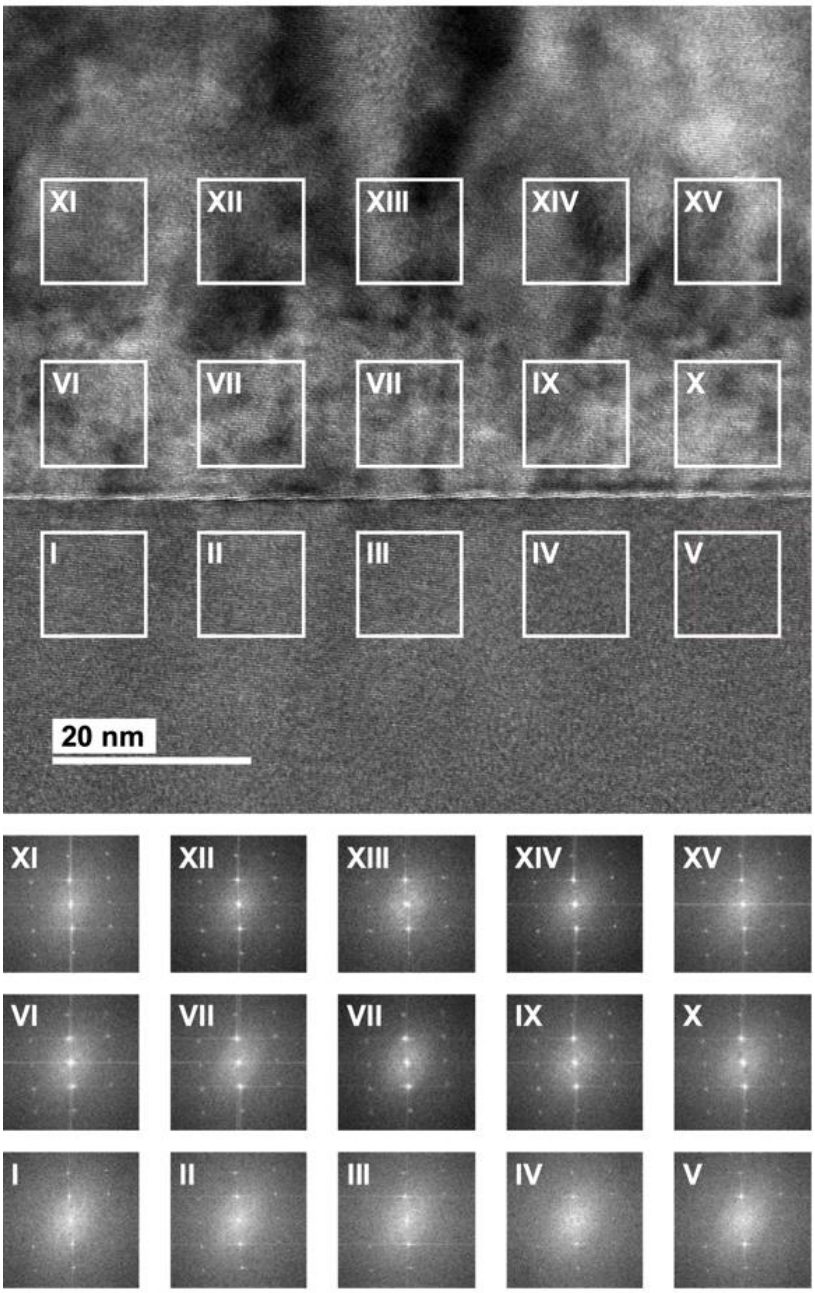

Figure 2.5 Fast Fourier Transform Analysis of a CVD-Templated Film on SiC. TEM image of the 20 nm 580℃ CVD templated - 170 nm sputtered AlN film on SiC with matching FFT patterns for the substrate (I-V), 580 ˚C CVD AlN layer (VI-X), and the sputtered AlN layer (XI-XV) at the bottom.

2.7 References:

[1] R.L. Xu, M. Munõz Rojo, S.M. Islam, A. Sood, B. Vareskic, A. Katre, N. Mingo, K.E. Goodson, H.G. Xing, D. Jena, E. Pop, Thermal conductivity of crystalline AlN and the influence of atomic-scale defects, J Appl Phys. 126 (2019). https://doi.org/10.1063/1.5097172.

[2] J.C. Nipko, C.-K. Loong, Phonon excitations and related thermal properties of aluminum nitride, Phys Rev B. 57 (1998) 10550–10554. https://doi.org/10.1103/PhysRevB.57.10550.

[3] A. Franco Júnior, D.J. Shanafield, Thermal conductivity of polycrystalline aluminum nitride (AlN) ceramics, Cerâmica. 50 (2004). https://doi.org/10.1590/s0366-69132004000300012.

[4] Y.J. Heo, H.T. Kim, K.J. Kim, S. Nahm, Y.J. Yoon, J. Kim, Enhanced heat transfer by room temperature deposition of AlN film on aluminum for a light emitting diode package, in: Appl Therm Eng, 2013: pp. 799–804. https://doi.org/10.1016/j.applthermaleng.2012.07.024.

[5] L. la Spina, E. Iborra, H. Schellevis, M. Clement, J. Olivares, L.K. Nanver, Aluminum nitride for heatspreading in RF IC's, Solid State Electron. 52 (2008) 1359–1363. https://doi.org/10.1016/j.sse.2008.04.009.

[6] J.W. Lee, S.H. Jung, H.Y. Shin, I.-H. Lee, C.-W. Yang, S.H. Lee, J.-B. Yoo, Effect of buffer layer on the growth of GaN on Si substrate, 2002.

[7] B.H. Kang, J.E. Lee, D.S. Kim, S. Bae, S. Jung, J. Park, J. Jhin, D. Byun, Effect of amorphous and crystalline AlN buffer layers deposited on patterned sapphire substrate on GaN film quality, J Nanosci Nanotechnol. 16 (2016). https://doi.org/10.1166/jnn.2016.13552.

[8] M. Sumiya, K. Fukuda, S. Yasiro, T. Honda, Influence of thin MOCVD-grown GaN layer on underlying AlN template, J Cryst Growth. 532 (2020). https://doi.org/10.1016/j.jcrysgro.2019.125376.

[9] A.C. Jones, S.A. Rushworth, D.J. Houlton, J.S. Roberts, V. Roberts, C.R. Whitehouse, G.W. Critchlow, Deposition of aluminum nitride thin films by MOCVD from the trimethylaluminum-ammonia adduct, Chemical Vapor Deposition. 2 (1996). https://doi.org/10.1002/cvde.19960020102.

[10] S. Yoshida, S. Misawa, Y. Fujii, S. Takada, H. Hayakawa, S. Gonda, A. Itoh, REACTIVE MOLECULAR BEAM EPITAXY OF ALUMINIUM NITRIDE., Journal of Vacuum Science & Technology. 16 (1979). https://doi.org/10.1116/1.570166.

[11] C.R. Eddy, T.J. Anderson, A.D. Koehler, N. Nepal, D.J. Meyer, M.J. Tadjer, R. Baranyai, J.W. Pomeroy, M. Kuball, T.I. Feygelson, B.B. Pate, M.A. Mastro, J.K. Hite, M.G. Ancona, F.J. Kub, K.D. Hobart, GaN Power Transistors with Integrated Thermal Management, ECS Trans. 58 (2013). https://doi.org/10.1149/05804.0279ecst.

[12] L. Shen, S. Heikman, B. Moran, R. Coffie, N.Q. Zhang, D. Buttari, I.P. Smorchkova, S. Keller, S.P. DenBaars, U.K. Mishra, AlGaN/AlN/GaN high-power microwave HEMT, IEEE Electron Device Letters. 22 (2001). https://doi.org/10.1109/55.954910.

[13] M. Bosund, T. Sajavaara, M. Laitinen, T. Huhtio, M. Putkonen, V.M. Airaksinen, H. Lipsanen, Properties of AlN grown by plasma enhanced atomic layer deposition, Appl Surf Sci. 257 (2011). https://doi.org/10.1016/j.apsusc.2011.04.037.

[14] P. Motamedi, K. Cadien, XPS analysis of AlN thin films deposited by plasma enhanced atomic layer deposition, Appl Surf Sci. 315 (2014). https://doi.org/10.1016/j.apsusc.2014.07.105.

[15] M. Legallais, H. Mehdi, S. David, F. Bassani, S. Labau, B. Pelissier, T. Baron, E. Martinez, G. Ghibaudo, B. Salem, Improvement of AlN Film Quality Using Plasma Enhanced Atomic Layer Deposition with Substrate Biasing, ACS Appl Mater Interfaces. 12 (2020). https://doi.org/10.1021/acsami.0c10515.

[16] H.Y. Shih, W.H. Lee, W.C. Kao, Y.C. Chuang, R.M. Lin, H.C. Lin, M. Shiojiri, M.J. Chen, Low-temperature atomic layer epitaxy of AlN ultrathin films by layer-by-layer, in-situ atomic layer annealing, Sci Rep. 7 (2017). https://doi.org/10.1038/srep39717.

[17] W.H. Lee, W.C. Kao, Y.T. Yin, S.H. Yi, K.W. Huang, H.C. Lin, M.J. Chen, Sub-nanometer heating depth of atomic layer annealing, Appl Surf Sci. 525 (2020). https://doi.org/10.1016/j.apsusc.2020.146615.

[18] A.I. Abdulagatov, R.R. Amashaev, K.N. Ashurbekova, K.N. Ashurbekova, M.K. Rabadanov, I.M. Abdulagatov, Atomic Layer Deposition of Aluminum Nitride and Oxynitride on Silicon Using Tris(dimethylamido)aluminum, Ammonia, and Water, Russ J Gen Chem. 88 (2018). https://doi.org/10.1134/S1070363218080236.

[19] Y.C. Jung, S.M. Hwang, D.N. Le, A.L.N. Kondusamy, J. Mohan, S.W. Kim, J.H. Kim, A.T. Lucero, A. Ravichandran, H.S. Kim, S.J. Kim, R. Choi, J. Ahn, D. Alvarez, J. Spiegelman, J. Kim, Low temperature thermal atomic layer deposition of aluminum nitride using hydrazine as the nitrogen source, Materials. 13 (2020). https://doi.org/10.3390/ma13153387.

[20] D. Riihelä, M. Ritala, R. Matero, M. Leskelä, J. Jokinen, P. Haussalo, Low Temperature Deposition of AlN Films by an Alternate Supply of Trimethyl Aluminum and Ammonia, Chemical Vapor Deposition. 2 (1996). https://doi.org/10.1002/cvde.19960020612.

[21] S.C. Buttera, D.J. Mandia, S.T. Barry, Tris(dimethylamido)aluminum(III): An overlooked atomic layer deposition precursor, Journal of Vacuum Science & Technology A: Vacuum, Surfaces, and Films. 35 (2017). https://doi.org/10.1116/1.4972469.

[22] S.T. Ueda, A. McLeod, D. Alvarez, D. Moser, R. Kanjolia, M. Moinpour, J. Woodruff, A.C. Kummel, Tris(dimethylamido)aluminum(III) and N2H4: Ideal precursors for the low-temperature deposition of large grain, oriented c-axis AlN on Si via atomic layer annealing, Appl Surf Sci. 554 (2021). https://doi.org/10.1016/j.apsusc.2021.149656.

[23] G. Liu, E. Deguns, L. Lecordier, G. Sundaram, J. Becker, Atomic Layer Deposition of AlN with Tris(Dimethylamido)Aluminum and NH 3 , ECS Trans. 41 (2011). https://doi.org/10.1149/1.3633671.

[24] L. Rosenberger, R. Baird, E. McCullen, G. Auner, G. Shreve, XPS analysis of aluminum nitride films deposited by plasma source molecular beam epitaxy, Surface and Interface Analysis. 40 (2008) 1254–1261. https://doi.org/10.1002/sia.2874.

[25] J.X. Zhang, H. Cheng, Y.Z. Chen, A. Uddin, S. Yuan, S.J. Geng, S. Zhang, Growth of AlN films on Si (100) and Si (111) substrates by reactive magnetron sputtering, Surf Coat Technol. 198 (2005) 68–73. https://doi.org/10.1016/j.surfcoat.2004.10.075.

[26] S.T. Ueda, A. McLeod, Y. Jo, Z. Zhang, J. Spiegelman, J. Spiegelman, D. Alvarez, D. Moser, R. Kanjolia, M. Moinpour, J. Woodruff, K. Cho, A.C. Kummel, Experimental and theoretical determination of the role of ions in atomic layer annealing, J Mater Chem C Mater. (2022). https://doi.org/10.1039/D1TC05194F.

CHAPTER 3

Atomic Layer Annealing with Radio Frequency Substrate Bias for Control of Grain Morphology in Gallium Nitride Thin Films

3.1 Abstract:

A method of performing atomic layer annealing with RF substrate bias on insulating and amorphous substrates is demonstrated for GaN deposition at 275 ˚C. GaN is typically deposited by MOCVD or MBE at >600 ˚C, resulting in strain upon cooling; this makes low temperature process alternatives desirable. Tris(dimethylamido) gallium (III) and hydrazine served as precursors while Ar and Kr were used for ion bombardment. Optimization of substrate bias potential is demonstrated by GI-XRD and XRR. Reference films were deposited by thermal ALD and non-substrate biased ALA processes. XPS surface and depth-profiling studies show that applied RF bias decreases film oxygen and carbon content relative to the reference films; these films also show crystallites broadening with increasing film thickness by TEM in contrast to the reference films. In summary, ALA with RF substrate bias is demonstrated as an effective method to deposit GaN thin films at a low deposition temperature on insulators.

3.2 Introduction:

Gallium nitride and other III-V materials are commonly deposited using high-temperature techniques, such as metal organic chemical vapor deposition (MOCVD) and molecular beam epitaxy (MBE) at temperatures exceeding 800 ˚C [1–13]. These elevated temperatures are often necessary to promote reactivity of gaseous nitridation agents, such as ammonia or nitrogen/hydrogen mixtures, and to crystallize the deposited material. GaN is typically deposited on sapphire or silicon carbide substrates, commonly requiring thick aluminum nitride (AlN) buffer

layers [3,5,6]. However, these elevated temperatures often produce stress in the films upon cooling due to differences in thermal expansion coefficients [1,7,8]. Accordingly, lower-temperature deposition methods and post-deposition annealing treatments for III-V materials are a focus of the materials science community [14–17].

Plasma-enhanced chemical vapor deposition (PE-CVD) and plasma-enhanced atomic layer deposition (PE-ALD) have shown promise for III-V materials; however, at low deposition temperatures compatible with standard techniques and equipment, PE-CVD and PE-ALD often produce films with high oxygen and carbon contamination [14,16,18–28]. Atomic layer annealing (ALA) processes have demonstrated an ability to further crystallize films deposited by both PE-ALD, where plasma-generated species serve as the co-reactant, and traditional thermal ALD with a chemical co-reactant [29–33]. In an ALA process, following each deposition cycle, a short bombardment with inert ions enhances surface adatom mobility and promotes the deposition of crystalline materials [29–34]. This allows for the healing of defects, such as amorphous chains on the growth surface and lattice vacancies on and below the growth surface. ALA processes may also produce films with comparatively lower contamination levels, as periodic ion bombardment may effectively heat the growth surface thereby desorbing residual ligands and contaminants and may sputter surface-bound contaminants, such as oxygen [29,32,33].

Applying DC bias to conductive substrates during the ALA treatment allows the momentum of the bombarding ions to be controlled; this additional tuning ensures that sufficient momentum is transferred to atoms on the growth surface to heal defects while remaining under damage, implantation, and sputtering thresholds [32,33]. Similar observations have been made in PE-ALD processes with applied substrate bias [21,35,36]. The use of a substrate bias decouples the tuning of ion momentum from tuning of the ion flux, which primarily depends on the power

applied to the plasma source. To date, ALA with substrate bias has been limited to DC bias applied; accordingly, development of ALA with RF substrate bias enables expansion of the ALA technique to insulating and patterned substrates without risk of damage due to charge buildup [32,33,37]. In the present study, RF substrate bias was applied during the ALA ion bombardment to deposit gallium nitride (GaN) on intrinsic silicon with 100 nm of thermal oxide (SiO_2/Si) substrates.

GaN was chosen as a model system due to the potential of a low-temperature deposition method to produce polycrystalline thin films or crystalline material on lattice-matched substrates. Advances in low temperature deposition on non-lattice matched substrates could lead to widespread implementation of GaN in lower-cost applications [18,38,39]. GaN is a desirable material due to its large breakdown voltage and high mobility compared to silicon; it is utilized alongside InGaN in many photonic and optoelectronic devices and is of considerable interest to the microLED industry [9,40–46].

3.3. Materials and Methods:

3.3.1 Substrates and Handling

Silicon (100) wafers with a 100 nm thick thermal oxide layer (SiO_2/Si) were purchased from University Wafter. Substrate coupons were diced, degreased using 30 s rinses of acetone, methanol, and water, and dried under N_2 before insertion into a load-lock vacuum chamber attached to the deposition and analysis chambers.

3.3.2 Atomic Layer Annealing Vacuum Chamber

Atomic layer annealing was performed in a homebuilt vacuum chamber system with a remote inductively coupled plasma (ICP) source (PIE Scientific Semi-KLEEN Sapphire Plasma Cleaner) and a homebuilt radio-frequency biased stage assembly. The stage was heated by an embedded cartridge heater controlled by a variable AC transformer such that the substrates in the sample carrier were heated to 275 ˚C, as determined by prior calibration studies. This chamber was pumped by a turbomolecular pump (Pfeiffer HiPace 300P). The walls of the atomic layer annealing chamber were heated to 90 ˚C while all tubing leading to the turbomolecular pump was not heated; an in-line liquid nitrogen trap (A&N Corp.) was filled approximately 20 minutes before each deposition to condense trace contaminants out of the gas phase. This resulted in a base pressure of $8x10^{-7}$ Torr.

3.3.3 Precursors, Dosing, And Plasma Treatment

Tris(dimethylamido) gallium (III) (TDMAGa, STREM Chemicals) was heated to 110 ˚C for deposition and held at 90 ˚C for storage; the dosing line was constantly heated to 115 ˚C. Anhydrous hydrazine was supplied by Rasirc, Inc and neither the precursor bottle nor the dosing lines were heated. Accordingly, the reported ALA technique is based on a thermal ALD process rather than a PE-ALD process. Argon push gas was used for both precursors and was purified using an Entegris GateKeeper placed just before the precursor containers. All precursor dosing and plasma treatment, a schematic of which is shown in Figure 3.1, was controlled by a LabView program. Each dosing cycle consisted of a 200 ms TDMAGa pulse (~40 mTorr) and a 175 ms hydrazine pulse (~60 mTorr) followed by purge times of 3 s and 7 s, respectively.

Approximately 7 sccm of Ar (PraxxAir 99.99%) or Kr (AirGas, 99.99%) was flowed through the vacuum chamber throughout the entire deposition, meaning this gas serves as both purge gas during precursor dosing and as the source of ions for plasma treatment. This brought the background pressure to 6 mTorr. To strike a plasma in the downstream ICP source (25 W, 13.560 MHz), an additional 20 sccm of gas was introduced for 1.5 s, briefly increasing the chamber pressure to 12 mTorr. An additional 500 ms long pulse of the desired ALA treatment gas at 80 sccm was used to extend the plasma into the deposition chamber. Following return to the background pressure of 6 mTorr, radio frequency bias was applied to the substrates for 8 s; this bias was supplied by an RF power supply (Manitou Systems Inc., 13.555 MHz) with the applied power adjusted to produce the desired substrate bias as indicated by the power supply display. All depositions were performed for 300 cycles.

3.3.4 Deposition of Reference Samples

An atomic layer deposition reference sample was deposited, where each cycle consisted of steps I-V from Figure 3.1. ALA reference samples without an applied substrate bias were also deposited, with each cycle consisting of steps I-IX in Figure 3.1. Ions generated by the ICP source produced a small self-bias of -4 V for both Ar and Kr.

3.3.5 X-Ray Diffraction and X-Ray Reflectivity

Grazing incidence x-ray diffraction (GI-XRD) and x-ray reflectivity (XRR) measurements were performed on a Rigakuy SmartLab system with a Cu anode operating at 2 kW under parallel beam configuration. GI-XRD measurements were performed using an incidence angle of 1.005˚ over a range 25-45˚ 2θ; diffraction peaks were analyzed using Rigaku GlobalFit software. XRR

profiles were obtained over 0-4˚ 2θ and were modeled to an R^2 value of less than 0.02 using Rigaku GlobalFit software to determine film thickness and density.

3.3.6 Spectroscopic Ellipsometry

Spectroscopic ellipsometry (SE) was performed using a J.A. Woollam M-2000D instrument at 500 wavelengths across a 193-1000 nm range and at a 75˚ incidence angle. The data was modeled using CompleteEASE software with an SiO_2 layer of 100 nm thickness and a GaN layer of thickness equivalent to that determined by XRR. The fit refractive index, n, of the films is reported at 633 nm.

3.3.7 Analytical Vacuum Chamber and X-Ray Photoelectron Spectroscopy

Following deposition, each set of samples was transferred without vacuum break to a separate chamber (Omicron VT) containing an x-ray photoelectron spectroscopy (XPS) system (STAIB Instruments DESA 150 CMA, Mg Kα source 1253.6 eV). A combination of turbomolecular, ionization, and titanium sublimation pumps utilized in this chamber maintained a base pressure of $5x10^{-10}$ Torr. Photoelectron spectra of the Ga 3d, N 1s, and O 1s regions were recorded at a 45˚ collection angle. Composition of the films was determined by peak fitting in CASA XPS 2.3 software using Shirley background profiles and correction using Scofield relative sensitivity factors.

3.3.8 Depth Profiling X-Ray Photoelectron Spectroscopy

X-ray photoelectron spectroscopy with depth profiling was performed on a film deposited using the Ar -14 V RF-biased ALA condition. Due to technical difficulties, this film was deposited

with chamber pumping performed by a turbomolecular pump with an integrated Holweck backing stage (Edwards EPX 500 NE). This required minor adjustments to precursor pulse lengths and gas flow rates to maintain equivalent dosing and plasma treatment pressures. The spectroscopy was performed in a Thermo Fisher Scientific Nexsa Surface Analyzer XPS instrument and was analyzed using Thermo Fisher Scientific Avantage (version 5.9925) software at Wayne State University. Sputtering was performed over a 2 mm x 2 mm area using argon ions supplied by an argon sputter gun positioned at a 45˚ angle with respect to the substrate normal. Incremental sputtering was performed in 30 s etch intervals with 500 eV acceleration potential. Measurements were made over a 0.2 mm^2 area using an Al Kα (1486.6 eV) X-ray source at a chamber base pressure of 10^{-8} Torr. High-resolution photoelectron spectra were collected for the Ga 2p, N 1s, O 1s, C 1s, and Si 2s ionization regions. Shirley background fitting was used in fitting peak areas from the high-resolution scans. The etching and characterization was performed for a total of 60 increments.

3.3.9 Transmission Electron Microscopy

Lamellae from selected films were prepared by Eurofins EAG (Sunnyvale, CA) with final thinning to approximately 30 nm. Transmission electron microscopy (TEM) was performed on a ThermoFisher Talos F200X instrument at 200 kV acceleration in bright field configuration. Image acquisition was performed using a Ceta 4k x 4k CMOS camera and Velox software. Fast Fourier Transform (FFT) and image processing was performed using Gatan Microscopy Suite software.

3.4 Results and Discussion:

3.4.1 X-Ray Diffraction and X-Ray Reflectivity

Grazing incidence x-ray diffraction was used to quantify the crystallinity of the deposited thin films and XRR was used to determine both density and thickness. All films deposited were of 30-35 nm thickness, except for those deposited at -44 V bias. A reference film deposited by thermal ALD was amorphous as determined by GI-XRD and had 5.08 g/cm^3 density as determined by XRR. All films deposited by ALA, both with and without radio frequency (RF) substrate bias, demonstrated diffraction at the expected (002) diffraction angle for gallium nitride (GaN). The GaN (002) diffraction regions for all films are shown in Figure 3.2; peak full width at half maximum (FWHM) and density by XRR are plotted as a function of substrate bias in Figure 3.3. In the reference depositions performed without RF bias applied, further denoted "ICP Only," a small -4 V self-bias developed. For these inductively coupled plasma (ICP) only processes, both argon and krypton produced films with increased density relative to the thermal ALD reference film at 5.70 g/cm^3 and 5.62 g/cm^3 respectively. These films demonstrated GaN (002) FWHM values of 0.76˚ and 1.02˚ respectively, indicating a nano-crystalline morphology.

Applying RF bias to the substrates during each ion bombardment step further increased crystallinity, as is shown by a smaller GaN (002) FWHM, and increased density. At -14 V, films deposited using Ar and Kr bombardment show significant improvement over the ICP only processes: GaN (002) peak FWHM decrease to 0.57˚ and 0.65˚, respectively and film densities are closer to that of bulk GaN (6.15 g/cm^3) at 6.07 g/cm^3 and 6.09 g/cm^3. Applying greater bias beyond -14 V shows only slightly increased density; this may indicate that at -14 V the bombarding ions for both process gasses have sufficient momentum transfer to the growth surface to begin to heal defects such as vacancies and amorphous chains. These densities are greater than that reported by

several PE-ALD techniques in the literature, ranging from 5.36 g/cm^3 -5.95 g/cm^3, highlighting the ability of substrate-biased ALA to densify the material deposited by ALD [27,47].

Film quality based on GaN (002) FWHM and density increase for the Ar and Kr processes at -24 V. The smallest GaN (002) FWHM of the Ar processes is observed at this condition 0.54˚. The density of this film is a bulk-like 6.14 g/cm^3. For the process run with Kr at -24 V, the (002) peak FWHM decreases to 0.58˚ and the density is slightly lower, at 6.11 g/cm^3. The optimal condition for Kr identified in this set is -34 V, where the film shows the most narrow (002) FWHM, 0.51˚, and a bulk-like density of 6.16 g/cm^3. The variance between Ar and Kr in the bias at which optimal film quality is observed may be the result of differences in how the bombarding ions interact with the growth surface.

At -44 V, both Ar and Kr ALA processes show significantly increased (002) FWHM. Further, the thickness of these films deviated from that of films produced at all other conditions, decreasing to 24.3 and 27.3 nm, respectively; this may be the cause of the decreased peak intensity observed in Figure 3.2. These observations are consistent with the onset of sputtering by the bombarding ions.

3.4.2 Spectroscopic Ellipsometry

The refractive indicies of the films deposited using the Ar -34 V and Kr -34 V bias conditions were determined to be 2.133 and 2.318 at 633 nm, respectively. These results are comparable to those of polycrystalline GaN films deposited by both PE-ALD and PE-CVD [25,27,48–50]. The Kr -34 V process result is within 3% of that of bulk GaN at 2.385 and is competitive with reported values for MOCVD processes, ranging from 2.24 to 2.397 [51–53].

3.4.3 X-Ray Photoelectron Spectroscopy

Composition of the films produced by the thermal ALD process, the ICP only processes, and the conditions at which Ar and Kr showed optimal crystallinity are shown in Figure 2.4. This composition information was determined by x-ray photoelectron spectroscopy (XPS) with corresponding photoelectron spectra and peak fits shown in Figure 3.5. It is noted that although films do not show 1:1 Ga:N stoichiometry, the films may be stoichiometric, as the large difference in binding energies between the Ga 3d region and N 1s regions at 19 eV and 397 eV, respectively, may result in varied photoelectron yield that is not entirely accounted for by the Scofield relative sensitivity factors utilized in calculating film composition. The thermal ALD film demonstrates the greatest oxygen content of 1.7 at.%. Atomic layer annealing reduces this contamination in all cases, with the largest oxygen reductions observed upon applying additional RF substrate bias to 0.4% and 0.7% for the Ar and Kr processes, respectively. This is consistent with ion bombardment resulting in the preferential sputtering of contaminants, such as residual ligands, and light elements, such as oxygen and carbon, from the growth surface during deposition. These results are a significant improvement over some of the lowest reported oxygen content of 1-2 at.% in the PE-ALD literature [27,29]. Due to the presence of multiple features in the C 1s region, carbon content was not analyzed in these experiments; however, carbon KLL Auger signal was not observed in any initial XPS survey scans.

3.4.4 Depth Profiling X-Ray Photoelectron Spectroscopy

The depth-dependent composition of an additional film deposited on SiO_2 using the Ar -14 V condition is shown in Figure 3.6, as determined by depth-profiling XPS. Due to the exposure of the sample to atmosphere prior to characterization, the surface of the film oxidized to

approximately 9.2% O. The surface oxidation reduced to the baseline level of oxygen detected in the film after 8 etching steps. The bulk of the film has an average composition of 48.4% Ga, 49.6% N, 1.8% O, and 0.2% C. The higher observed oxygen content in the bulk of the film relative to the *in-vacuo* XPS performed immediately after sample deposition may be due to edge effects, as the 2 mm width of the sputtered region is close to the 2.5 mm width of the substrate coupon. These discrepancies may also be due to differences in fitting procedure and sensitivity factors for the two XPS instruments. The low carbon content in the bulk of the film is consistent with ion bombardment promoting desorption of residual ligands and contaminants from the growth surface during each ALA cycle. It is possible that ALA with further increased substrate bias potential, such as the optimal -24 V and -34 V conditions, may demonstrate lower bulk oxygen content due to increased kinetic energy of the bombarding ions sputtering contaminants from the growth surface.

3.4.5 Transmission Electron Microscopy Analysis

The transmission electron microscopy (TEM) and accompanying fast Fourier transform (FFT) analysis for a film deposited by each of the ICP only, -24 V, and -34 V conditions with Ar and Kr is shown in Figure 3.7. Enlarged versions with polycrystalline grains outlined and enlarged FFT patterns of these micrographs are shown in Figures 3.8-3.13. The ICP only films deposited using Ar and Kr, Figures 3.7 (a) and (d), respectively, demonstrate an amorphous region nearest to the substrate interface identified by the presence of rings rather than discrete diffraction spots in the FFT analysis region I. A morphology of packed crystallites develops with increasing film thickness as shown by the presence of arcs in the FFT analyses for regions II-IV. Notable is the absence of any progressive strengthening of diffraction spots with film thickness; this indicates

that film is composed of packed nanocrystalline regions without preferred orientation. This may be due to the bombarding ions having kinetic energy sufficient to increase local surface adatom mobility leading to the creation of nanocrystalline regions, but insufficient to facilitate the development of long-range order. This is consistent with the large GaN (002) FWHM and low density of these films as identified by GI-XRD and XRR (Figures 3.2 and 3.3).

The -24 V conditions for Ar and Kr, 2.7 (b) and (e), respectively show an amorphous layer similar to that of the ICP only conditions at the interface; however, in these films, crystallinity increases with further deposition. This is observed by the broadening of crystalline regions with increasing film thickness in the micrographs and gradual strengthening of diffraction spots in the FFT patterns from regions II to regions IV. Of note is the significant tilting of grains in the Kr -24 V film, which is visible in the TEM and in the orientation of the FFT patterns. This tilting may have produced a broadened (002) diffraction peak in GI-XRD, as indicated in Figures 3.2 and 3.3. Shown in Figure 3.7 (c) and (f) are the micrographs for -34 V conditions for Ar and Kr. These films demonstrate morphologies and increases in crystallinity with thickness similar to the films deposited at -24 V, which is consistent with only minute differences identified by GI-XRD and XRR. The ability of the -24 V and -34 V ALA deposition processes to facilitate long-range order indicates that increased kinetic energy of the bombarding ions may induce collision cascades capable of healing sub-surface defects during the growth process. It is also possible that the increased kinetic energy may be responsible for sputtering any oxygen from the growth surface, leading to the lower oxygen content as detected by XPS (Figure 3.4).

3.5 Conclusion:

The present results demonstrate the ability to RF substrate-biased atomic layer annealing on amorphous and insulating substrates to deposit polycrystalline GaN of greater quality than reference depositions performed by thermal ALD or ALA without applied substrate bias. The optimization of bias potential is necessary to ensure that the kinetic energy of the bombarding ions remains below sputtering and implanting thresholds. The GI-XRD and XRR results demonstrate marked increases in film density and decreases in diffraction peak width at moderate -24 V and -34 V biases with ion bombardment by Ar and Kr. The *in-vacuuo* XPS composition analysis demonstrates that applied substrate bias in an ALA process can improve film composition by reducing oxygen content. Comparison of films deposited by the -24 V and -34 V RF-biased ALA conditions using TEM and FFT analysis demonstrates that while ALA without substrate bias can deposit polycrystalline films, an applied RF bias enables the development of long-range order in the deposited material. In comparison to previous DC-biased ALA studies of aluminum nitride, with this RF-biased study, minimal difference exists in the morphology of films deposited using Ar and Kr plasma treatment. This technique may find use in the deposition of high quality polycrystalline thin films at low temperatures on amorphous and insulating materials commonly utilized in optoelectronics, back-end thin film transistors, and metal semi-damascene deposition processes.

3.6 Acknowledgements

This work was supported in part by the Applications and Systems- Driven Center for Energy Efficient Integrated Nano Technologies (ASCENT), one of six centers in the Joint University Microelectronics Program (JUMP), an SRC program sponsored by the Defense Advanced Research Program Agency (DARPA). This work was performed in part at the San Diego Nanotechnology Infrastructure (SDNI) at UC San Diego, a member of the National Nanotechnology Coordinate Infrastructure, which is supported by the National Science Foundation (ECCS-1542148).

Chapter 3, in full, has been submitted for publication of the material as it may appear in the following publication, of which the dissertation author was the primary researcher and author:

McLeod, Aaron J.; Lee, Ping Che; Ueda, Scott T.; Devereaux, Zachary J.; Winter, Charles H.; Spiegelman, Jeff; Kanjolia, Ravindra; Moinpour, Mansour; Kummel, Andrew C. "Atomic Layer Annealing with Radio Frequency Substrate Bias for Control of Grain Morphology in Gallium Nitride Thin Films", Materials Research Society Bulletin Impact Section, 2023.

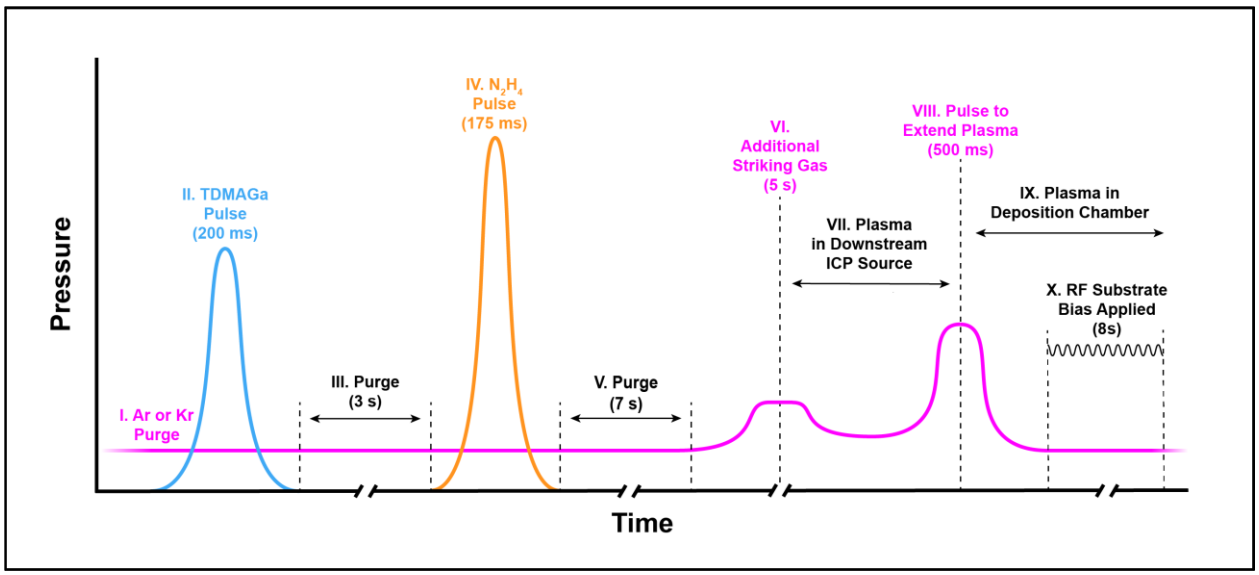

Figure 3.1 Precursor Pulsing, Purging, and Plasma Treatment Schematic. Each ALA cycle consisted of the following steps: I. Either Ar or Kr served as both purge gas and as the plasma treatment gas. II. TDMAGa pulses were 200 ms in duration and approximately 40 mTorr, followed by a 3 s purge (III). IV. A 175 ms pulse of hydrazine increased the chamber pressure to approximately 60 mTorr and was followed by a 7 s purge (V). VI. Additional gas required to strike a plasma in the remote ICP source was introduced, which brought the chamber pressure to 12 mTorr. VII. The plasma was contained in the remote ICP source until a larger pulse of gas extended the plasma into the deposition chamber (IX). X. Upon pumping down to the constant 6 mTorr purge pressure, RF bias (if utilized) was applied to the substrates for 8 s.

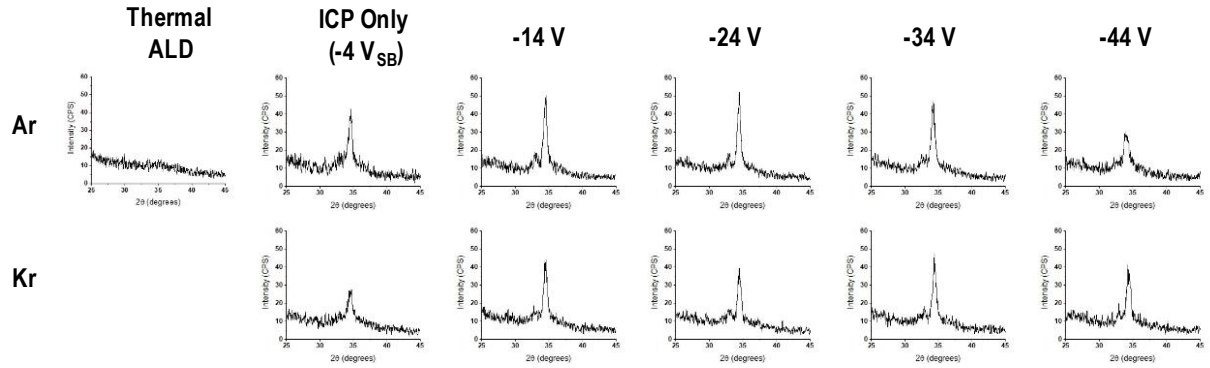

Figure 3.2 Grazing-Incidence X-Ray Diffraction of All Films. The GaN (002) diffraction peak region for each deposited film is shown. The thermal ALD process was only performed with Ar purge gas and shows that the film is amorphous. The ICP Only processes deposited weakly polycrystalline films, while films deposited with applied RF bias demonstrate stronger crystallinity as indicated by the more narrow and more intense diffraction peaks. Note that the diffraction peaks are most narrow for the Ar -24 V and Kr -34 V conditions. Increasing the bias to the -44 V condition resulted in both decreased peak intensity and increased width, indicating that the ion bombardment was likely too energetic and began damaging the films.

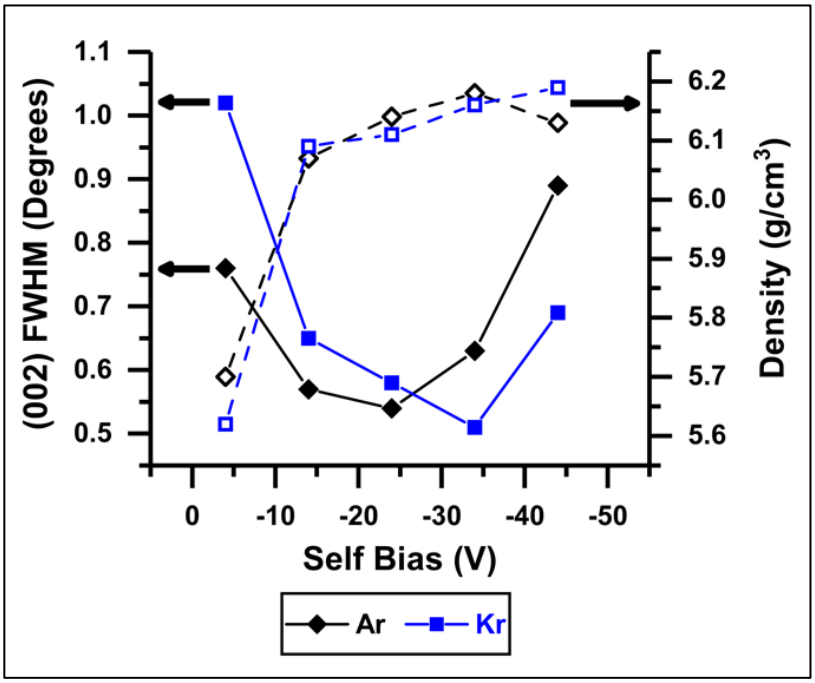

Figure 3.3 Film Quality as a Function of Substrate Bias. The GaN (002) diffraction peak FWHM determined by GI-XRD and density determined by XRR fitting for the ALA films deposited using Ar and Kr as the process gasses. Both Ar and Kr showed similar initial results, with improvements in film quality at -4 V (ICP only) process, and further improvements at -14 V. For the set of processes using Ar, optimal crystallinity was observed at -24 V, whereas Kr showed optimal crystallinity at -34 V. At -44 V, film quality degraded significantly, indicating the onset of sputtering and/or ion embedding.

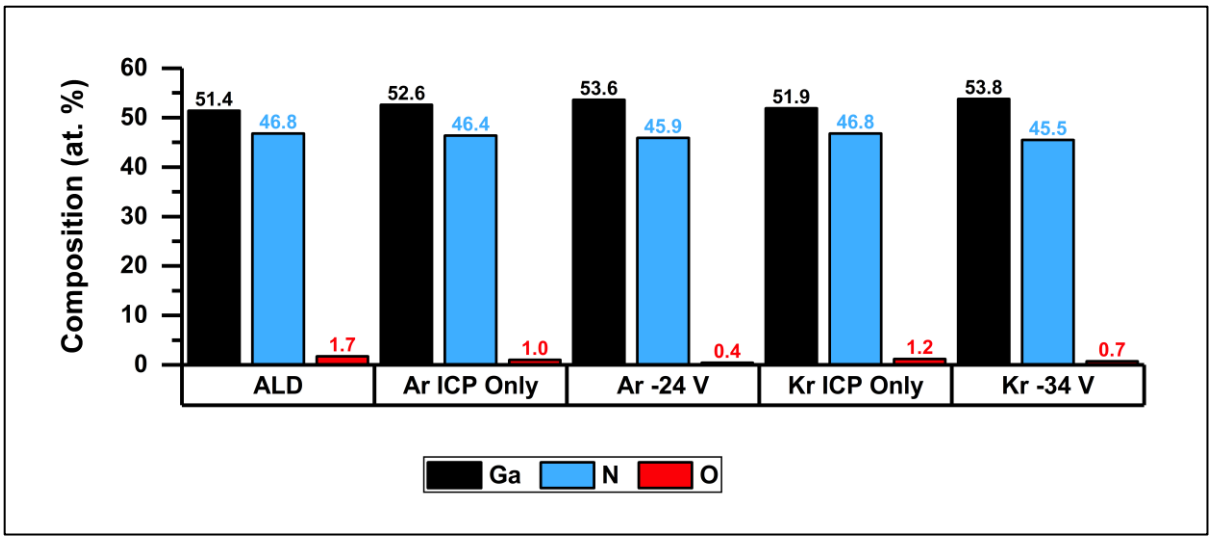

Figure 3.4 Film Composition Determined by X-Ray Photoelectron Spectroscopy. The composition of the top 3-5 nm of films produced by the reference thermal ALD process, the reference Ar and Kr ICP only processes, and the optimal Ar -24V and Kr -34 V processes. Note that all ALA conditions show decreased oxygen content relative to the thermal ALD film, with greatest reduction observed on both samples with applied RF bias. Note that 1:1 Ga:N stoichiometry is not observed, however this may be an effect of the large differences in binding energies between the Ga 3d and N 1s photoelectron binding energies.

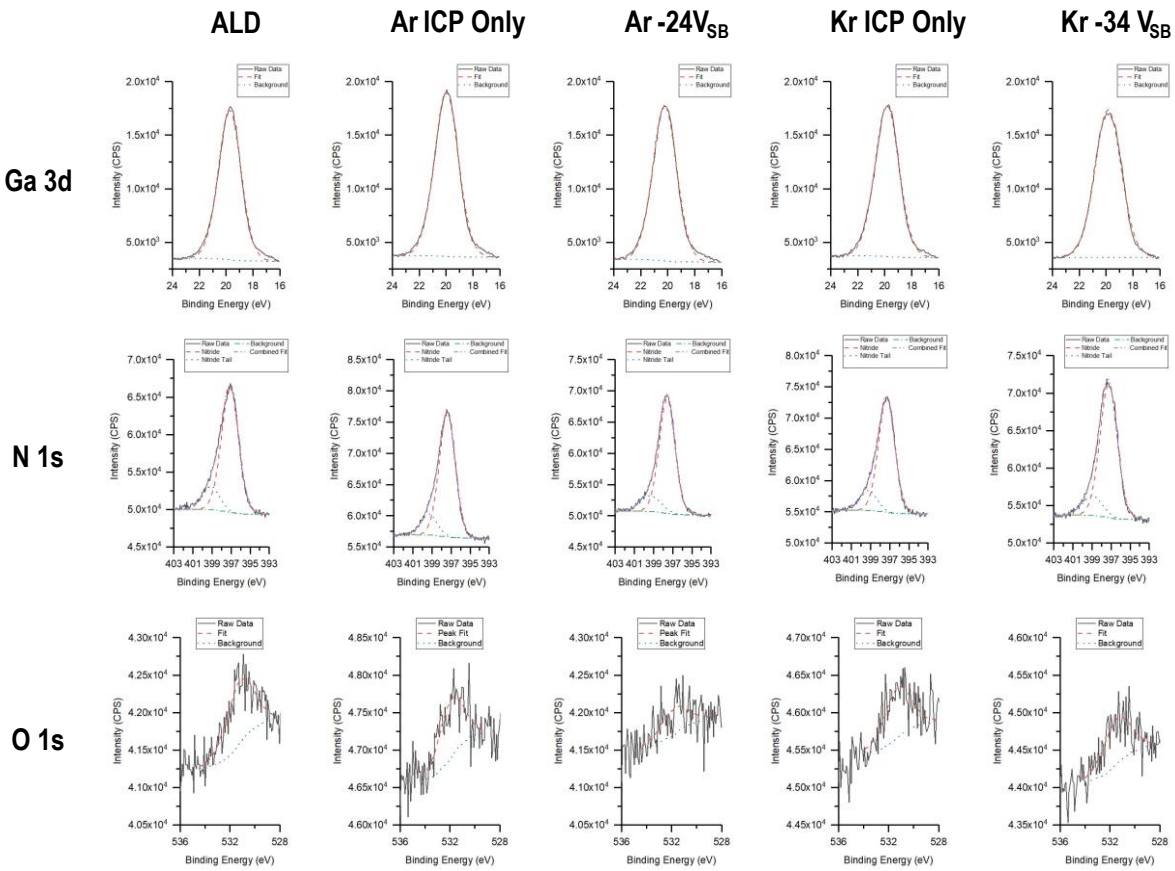

Figure 3.5 X-Ray Photoelectron Spectra for Regions Used to Determine Surface Composition. The Ga 3d, N 1s, and O 1s photoelectron spectra region used for calculating film composition are shown for selected process conditions – thermal ALD, Ar ICP only, Ar -24 V_{SB}, Kr ICP Only, and Kr -34 V_{SB}. The background and peak shapes used in fitting are shown. Note that the N 1s region was fit with two peaks as is characteristic for group III nitride materials.

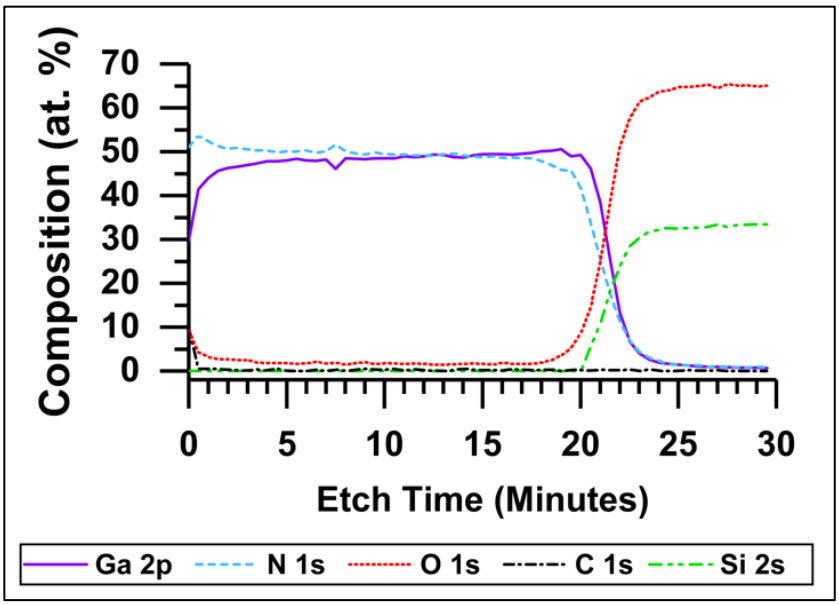

Figure 3.6 Film Composition by Depth Profiling X-Ray Photoelectron Spectroscopy. A GaN thin film deposited using the RF-biased Ar -14 V condition on an SiO_2 substrate shows an oxidized surface due to atmospheric exposure before analysis and a relatively pure bulk region with average 48.4% Ga, 49.6% N, 1.8% O, and 0.2% C content.

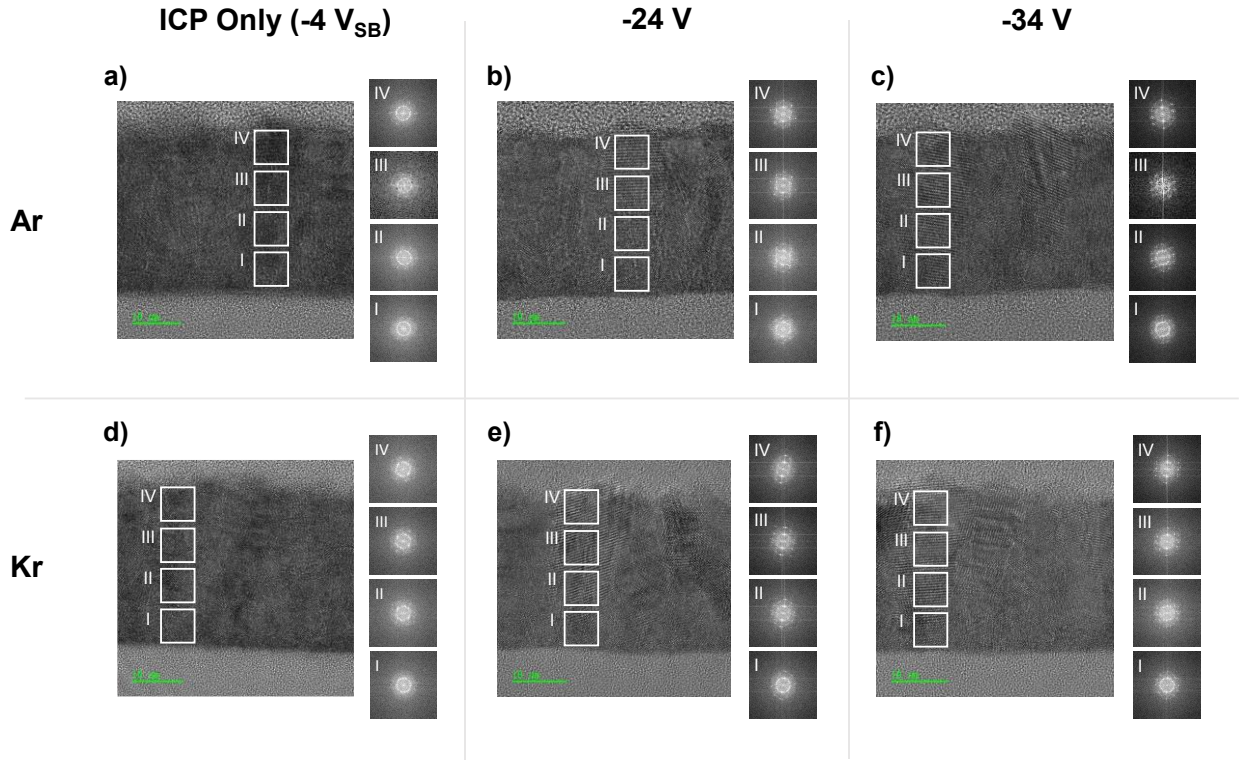

Figure 3.7 Transmission Electron Microscopy and Fast Fourier Transform Analysis. Thin films of GaN deposited on SiO_2 using Ar (a-c) and Kr (d-f) as the ion source in ALA at various bias potentials. Note that the ICP only condition did not utilize an applied RF bias, however the downstream plasma itself generated a -4 V potential. The ICP only films (a, d) are polycrystalline with grains of varied orientations, as is indicated by the presence of ring-like patterns in the FFT analyses. The -24 V films (b, e) show more columnar-like growth with FFT patterns demonstrating the development of well-defined crystallites of a single orientation throughout the deposition process. The -34 V films (d, f) show morphology similar to that of the -24 V films.

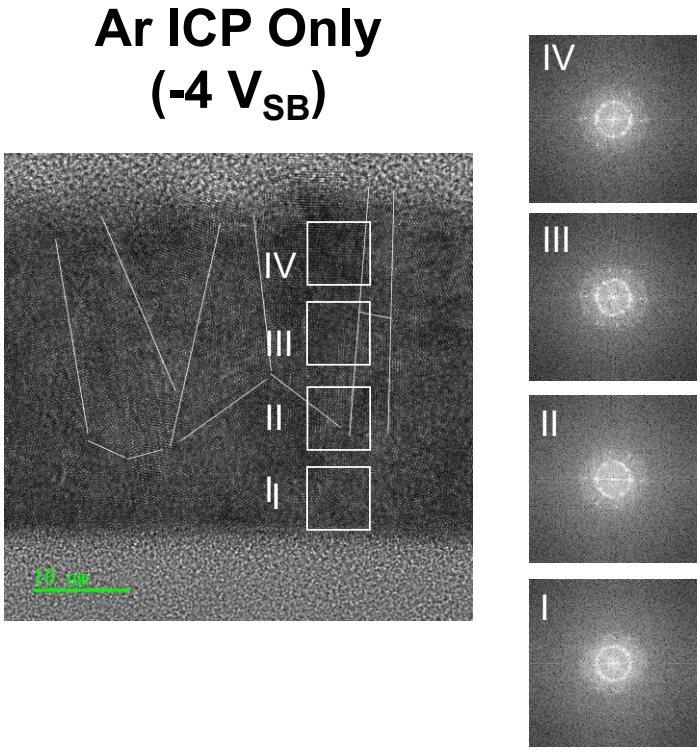

Figure 3.8 TEM and FFT of Film Deposited by the Ar ICP Only Condition. The film deposited by the Ar ICP only condition demonstrates densely packed nanocrystallites without preferential orientation. Lines drawn to guide the eye. The FFT regions I-IV all show diffraction rings with a minimal amount of discrete diffraction spots, indicating that crystallites are present, however alongside a large amount of amorphous material.

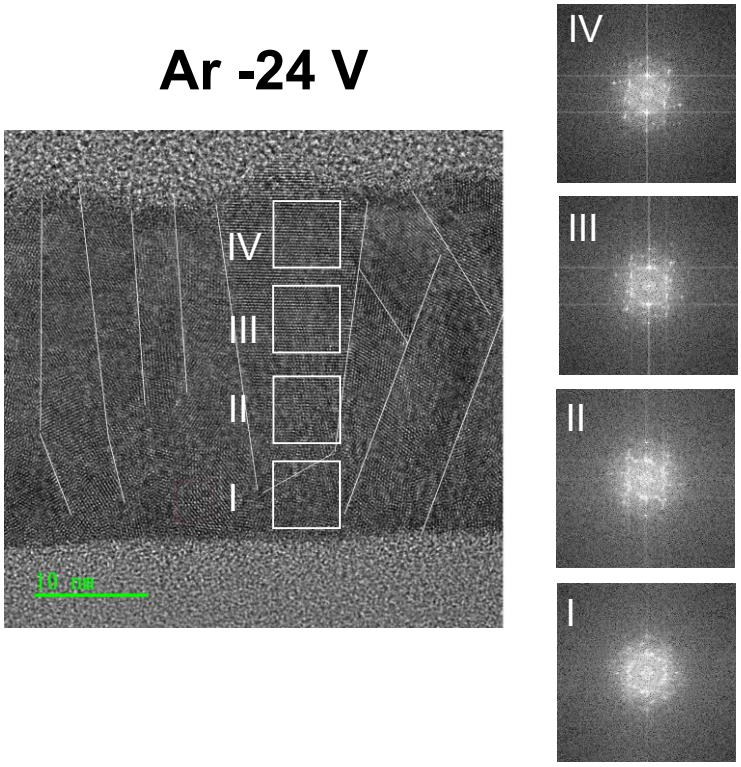

Figure 3.9 TEM and FFT of Film Deposited by the Ar -24 V RF bias Condition. The film deposited by the Ar -24 V applied RF bias condition demonstrates grains of columnar morphology and preferential c-axis orientation. Lines drawn to guide the eye. The FFT regions I-IV show an improvement in crystallinity consistent with a nearly-amorphous interface to developed crystallites at the film surface.

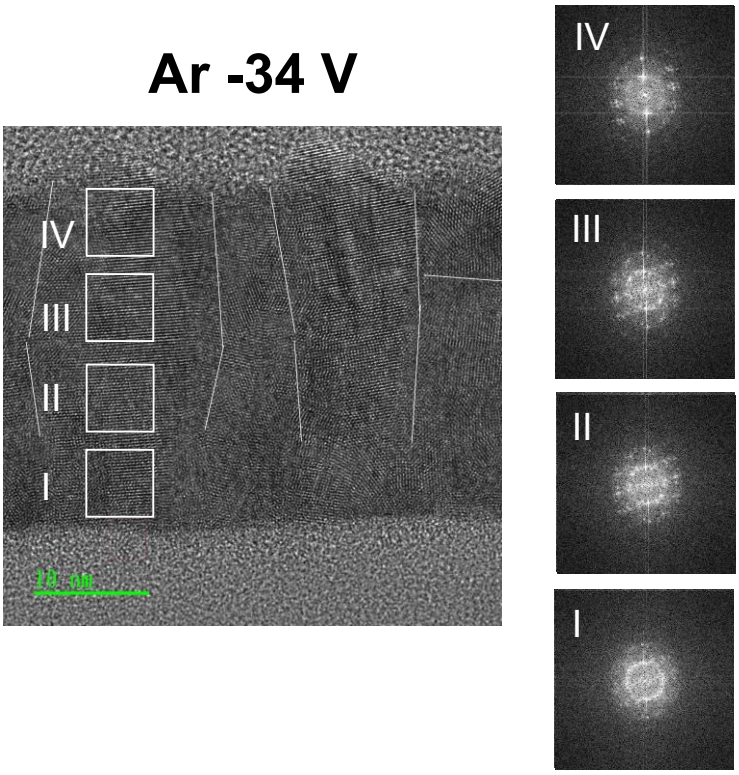

Figure 3.10 TEM and FFT of Film Deposited by the Ar -34 V RF bias Condition. The film deposited by the Ar -34 V applied RF bias condition demonstrates largely columnar grains with preferential c-axis orientation. Lines drawn to guide the eye. The FFT regions I-IV show an improvement in crystallinity consistent with a nearly-amorphous interface to large crystallites at the film surface.

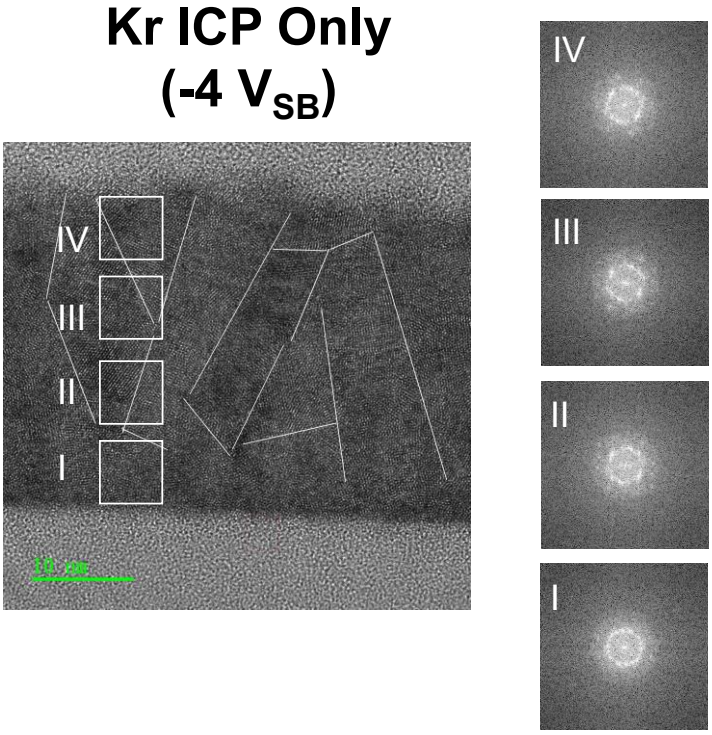

Figure 3.11 TEM and FFT of Film Deposited by the Kr ICP Only Condition. The film deposited by the Kr ICP only condition demonstrates densely packed small grains without preferential orientation. Lines drawn to guide the eye. The FFT regions I-IV all show diffraction arcs with a minimal amount of discrete diffraction spots, indicating that crystallites are present but do not have a preferred orientation.

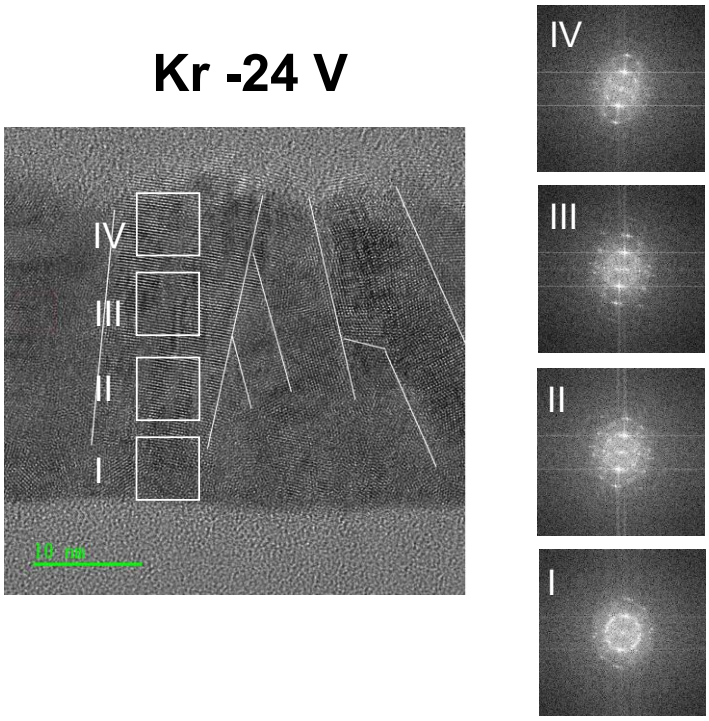

Figure 3.12 TEM and FFT of Film Deposited by the Kr -24 V RF bias Condition. The film deposited by the Kr -24 V applied RF bias condition demonstrates a large amount of tilted but columnar grains. Lines drawn to guide the eye. The FFT regions I-IV show an improvement in crystallinity consistent with a nearly-amorphous interface to developed crystallites at the film surface.

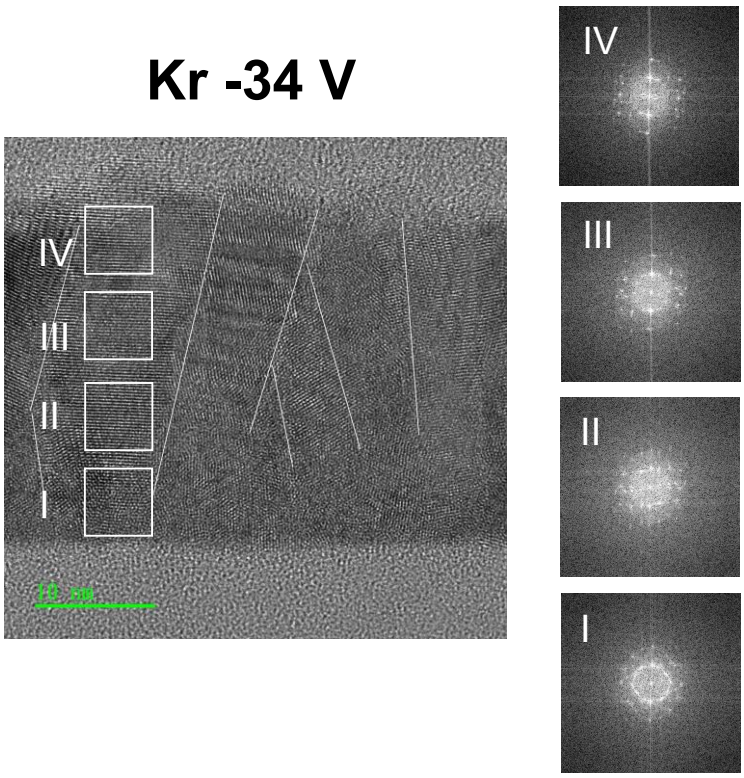

Figure 3.13 TEM and FFT of Film Deposited by the Kr -34 V RF bias Condition. The film deposited by the Kr -34 V applied RF bias condition large columnar grains with preferential but tilted c-axis orientation. Lines drawn to guide the eye. The FFT regions I-IV show an improvement in crystallinity consistent with a nearly-amorphous interface to large crystallites at the film surface.

3.7 References:

[1] P. Gibart, Metal organic vapour phase epitaxy of GaN and lateral overgrowth, Reports on Progress in Physics. 67 (2004) 667–715. https://doi.org/10.1088/0034-4885/67/5/R02.

[2] M. Sumiya, K. Fukuda, S. Yasiro, T. Honda, Influence of thin MOCVD-grown GaN layer on underlying AlN template, J Cryst Growth. 532 (2020). https://doi.org/10.1016/j.jcrysgro.2019.125376.

[3] J.W. Lee, S.H. Jung, H.Y. Shin, I.-H. Lee, C.-W. Yang, S.H. Lee, J.-B. Yoo, Effect of buffer layer on the growth of GaN on Si substrate, 2002.

[4] M. Asif Khan, J.N. Kuznia, J.M. van Hove, D.T. Olson, S. Krishnankutty, R.M. Kolbas, Growth of high optical and electrical quality GaN layers using low-pressure metalorganic chemical vapor deposition, Appl Phys Lett. 58 (1991) 526–527. https://doi.org/10.1063/1.104575.

[5] B.H. Kang, J.E. Lee, D.S. Kim, S. Bae, S. Jung, J. Park, J. Jhin, D. Byun, Effect of amorphous and crystalline AlN buffer layers deposited on patterned sapphire substrate on GaN film quality, J Nanosci Nanotechnol. 16 (2016). https://doi.org/10.1166/jnn.2016.13552.

[6] K. Tamura, Y. Kuroki, K. Yasui, M. Suemitsu, T. Ito, T. Endou, H. Nakazawa, Y. Narita, M. Takata, T. Akahane, Growth of GaN on SiC/Si substrates using AlN buffer layer by hot-mesh CVD, Thin Solid Films. 516 (2008) 659–662. https://doi.org/10.1016/j.tsf.2007.06.200.

[7] T. Kozawa, T. Kachi, H. Kano, H. Nagase, N. Koide, K. Manabe, Thermal stress in GaN epitaxial layers grown on sapphire substrates, J Appl Phys. 77 (1995) 4389–4392. https://doi.org/10.1063/1.359465.

[8] R.F. Davis, S. Einfeldt, E.A. Preble, A.M. Roskowski, Z.J. Reitmeier, P.Q. Miraglia, Gallium nitride and related materials: Challenges in materials processing, Acta Mater. 51 (2003) 5961–5979. https://doi.org/10.1016/j.actamat.2003.08.005.

[9] H. Amano, Y. Baines, E. Beam, M. Borga, T. Bouchet, P.R. Chalker, M. Charles, K.J. Chen, N. Chowdhury, R. Chu, C. de Santi, M.M. de Souza, S. Decoutere, L. di Cioccio, B. Eckardt, T. Egawa, P. Fay, J.J. Freedsman, L. Guido, O. Häberlen, G. Haynes, T. Heckel, D. Hemakumara, P. Houston, J. Hu, M. Hua, Q. Huang, A. Huang, S. Jiang, H. Kawai, D. Kinzer, M. Kuball, A. Kumar, K.B. Lee, X. Li, D. Marcon, M. März, R. McCarthy, G. Meneghesso, M. Meneghini, E. Morvan, A. Nakajima, E.M.S. Narayanan, S. Oliver, T. Palacios, D. Piedra, M. Plissonnier, R. Reddy, M. Sun, I. Thayne, A. Torres, N. Trivellin, V. Unni, M.J. Uren, M. van Hove, D.J. Wallis, J. Wang, J. Xie, S. Yagi, S. Yang, C. Youtsey, R. Yu, E. Zanoni, S. Zeltner, Y. Zhang, The 2018 GaN power electronics roadmap, J Phys D Appl Phys. 51 (2018). https://doi.org/10.1088/1361-6463/aaaf9d.

[10] G. Li, W. Wang, W. Yang, Y. Lin, H. Wang, Z. Lin, S. Zhou, GaN-based light-emitting diodes on various substrates: A critical review, Reports on Progress in Physics. 79 (2016). https://doi.org/10.1088/0034-4885/79/5/056501.

[11] D. Zhu, D.J. Wallis, C.J. Humphreys, Prospects of III-nitride optoelectronics grown on Si, Reports on Progress in Physics. 76 (2013). https://doi.org/10.1088/0034-4885/76/10/106501.

[12] M.Z. Mohd Yusoff, A. Mahyuddin, Z. Hassan, H. Abu Hassan, M.J. Abdullah, M. Rusop, S.M. Mohammad, N.M. Ahmed, AlN/GaN/AlN heterostructures grown on Si substrate by plasma-assisted MBE for MSM UV photodetector applications, Mater Sci Semicond Process. 29 (2015) 231–237. https://doi.org/10.1016/j.mssp.2014.03.041.

[13] Q. Zhang, X. Yin, S. Zhao, Recent Progress on Aluminum Gallium Nitride Deep Ultraviolet Lasers by Molecular Beam Epitaxy, Physica Status Solidi - Rapid Research Letters. 15 (2021). https://doi.org/10.1002/pssr.202100090.

[14] C. Ozgit-Akgun, E. Goldenberg, A.K. Okyay, N. Biyikli, Hollow cathode plasma-assisted atomic layer deposition of crystalline AlN, GaN and AlxGa1-xN thin films at low temperatures, J Mater Chem C Mater. 2 (2014) 2123–2136. https://doi.org/10.1039/c3tc32418d.

[15] N.H. Karam, T. Parodos, P. Colter, D. McNulty, W. Rowland, J. Schetzina, N. El-Masry, S.M. Bedair, Growth of device quality GaN at 550°C by atomic layer epitaxy, Appl Phys Lett. 67 (1995) 94. https://doi.org/10.1063/1.115519.

[16] J.K. Sprenger, A.S. Cavanagh, H. Sun, K.J. Wahl, A. Roshko, S.M. George, Electron Enhanced Growth of Crystalline Gallium Nitride Thin Films at Room Temperature and 100 °c Using Sequential Surface Reactions, Chemistry of Materials. 28 (2016) 5282–5294. https://doi.org/10.1021/acs.chemmater.6b00676.

[17] W.H. Lee, F.J. Jhong, Y.T. Yin, C.Y. Chou, J.J. Shyue, M.J. Chen, Large area and rapid electron beam annealing for high-quality epitaxial GaN layer, Mater Res Bull. 153 (2022). https://doi.org/10.1016/j.materresbull.2022.111903.

[18] H. Wei, J. Wu, P. Qiu, S. Liu, Y. He, M. Peng, D. Li, Q. Meng, F. Zaera, X. Zheng, Plasma-enhanced atomic-layer-deposited gallium nitride as an electron transport layer for planar perovskite solar cells, J Mater Chem A Mater. 7 (2019) 25347–25354. https://doi.org/10.1039/c9ta08929b.

[19] M. Bosund, T. Sajavaara, M. Laitinen, T. Huhtio, M. Putkonen, V.M. Airaksinen, H. Lipsanen, Properties of AlN grown by plasma enhanced atomic layer deposition, Appl Surf Sci. 257 (2011). https://doi.org/10.1016/j.apsusc.2011.04.037.

[20] P. Motamedi, K. Cadien, XPS analysis of AlN thin films deposited by plasma enhanced atomic layer deposition, Appl Surf Sci. 315 (2014). https://doi.org/10.1016/j.apsusc.2014.07.105.

[21] M. Legallais, H. Mehdi, S. David, F. Bassani, S. Labau, B. Pelissier, T. Baron, E. Martinez, G. Ghibaudo, B. Salem, Improvement of AlN Film Quality Using Plasma Enhanced Atomic Layer Deposition with Substrate Biasing, ACS Appl Mater Interfaces. 12 (2020). https://doi.org/10.1021/acsami.0c10515.

[22] N.J. O'Brien, P. Rouf, R. Samii, K. Rönnby, S.C. Buttera, C.W. Hsu, I.G. Ivanov, V. Kessler, L. Ojamäe, H. Pedersen, In Situ Activation of an Indium(III) Triazenide Precursor for Epitaxial Growth of Indium Nitride by Atomic Layer Deposition, Chemistry of Materials. 32 (2020) 4481–4489. https://doi.org/10.1021/acs.chemmater.9b05171.

[23] S. Liu, G. Zhao, Y. He, H. Wei, Y. Li, P. Qiu, Y. Song, Y. An, X. Wang, X. Wang, J. Cheng, M. Peng, X. Zheng, Interfacial Tailoring for the Suppression of Impurities in GaN by in Situ Plasma Pretreatment via Atomic Layer Deposition, ACS Appl Mater Interfaces. 11 (2019) 35382–35388. https://doi.org/10.1021/acsami.9b08816.

[24] P. Rouf, N.J. O'Brien, S.C. Buttera, I. Martinovic, B. Bakhit, E. Martinsson, J. Palisaitis, C.W. Hsu, H. Pedersen, Epitaxial GaN using Ga(NMe2)3and NH3plasma by atomic layer deposition, J Mater Chem C Mater. 8 (2020) 8457–8465. https://doi.org/10.1039/d0tc02085k.

[25] S. Liu, G. Zhao, Y. He, H. Wei, Y. Li, P. Qiu, Y. Song, Y. An, X. Wang, X. Wang, J. Cheng, M. Peng, X. Zheng, Interfacial Tailoring for the Suppression of Impurities in GaN by in Situ Plasma Pretreatment via Atomic Layer Deposition, ACS Appl Mater Interfaces. 11 (2019) 35382–35388. https://doi.org/10.1021/acsami.9b08816.

[26] M. Alevli, A. Haider, S. Kizir, S.A. Leghari, N. Biyikli, Comparison of trimethylgallium and triethylgallium as "Ga" source materials for the growth of ultrathin GaN films on Si (100) substrates via hollow-cathode plasma-assisted atomic layer deposition, Journal of Vacuum Science & Technology A: Vacuum, Surfaces, and Films. 34 (2016) 01A137. https://doi.org/10.1116/1.4937725.

[27] S. Kizir, A. Haider, N. Biyikli, Substrate impact on the low-temperature growth of GaN thin films by plasma-assisted atomic layer deposition, Journal of Vacuum Science & Technology A: Vacuum, Surfaces, and Films. 34 (2016) 041511. https://doi.org/10.1116/1.4953463.

[28] C. Ozgit, I. Donmez, M. Alevli, N. Biyikli, Atomic layer deposition of GaN at low temperatures, Journal of Vacuum Science & Technology A: Vacuum, Surfaces, and Films. 30 (2012) 01A124. https://doi.org/10.1116/1.3664102.

[29] H.Y. Shih, W.H. Lee, W.C. Kao, Y.C. Chuang, R.M. Lin, H.C. Lin, M. Shiojiri, M.J. Chen, Low-temperature atomic layer epitaxy of AlN ultrathin films by layer-by-layer, in-situ atomic layer annealing, Sci Rep. 7 (2017). https://doi.org/10.1038/srep39717.

[30] W.H. Lee, W.C. Kao, Y.T. Yin, S.H. Yi, K.W. Huang, H.C. Lin, M.J. Chen, Sub-nanometer heating depth of atomic layer annealing, Appl Surf Sci. 525 (2020). https://doi.org/10.1016/j.apsusc.2020.146615.

[31] W.-H. Lee, Y.-T. Yin, P.-H. Cheng, J.-J. Shyue, M. Shiojiri, H.-C. Lin, M.-J. Chen, Nanoscale GaN Epilayer Grown by Atomic Layer Annealing and Epitaxy at Low Temperature, ACS Sustain Chem Eng. 7 (2019) 487–495. https://doi.org/10.1021/acssuschemeng.8b03982.

[32] S.T. Ueda, A. McLeod, Y. Jo, Z. Zhang, J. Spiegelman, J. Spiegelman, D. Alvarez, D. Moser, R. Kanjolia, M. Moinpour, J. Woodruff, K. Cho, A.C. Kummel, Experimental and theoretical determination of the role of ions in atomic layer annealing, J Mater Chem C Mater. (2022). https://doi.org/10.1039/D1TC05194F.

[33] S.T. Ueda, A. McLeod, D. Alvarez, D. Moser, R. Kanjolia, M. Moinpour, J. Woodruff, A.C. Kummel, Tris(dimethylamido)aluminum(III) and N2H4: Ideal precursors for the low-temperature deposition of large grain, oriented c-axis AlN on Si via atomic layer annealing, Appl Surf Sci. 554 (2021). https://doi.org/10.1016/j.apsusc.2021.149656.

[34] A.J. McLeod, S.T. Ueda, P.C. Lee, J. Spiegelman, R. Kanjolia, M. Moinpour, J. Woodruff, A.C. Kummel, Pulsed chemical vapor deposition for crystalline aluminum nitride thin films and buffer layers on silicon and silicon carbide, Thin Solid Films. 768 (2023). https://doi.org/10.1016/j.tsf.2023.139717.

[35] H.B. Profijt, M.C.M. van de Sanden, W.M.M. Kessels, Substrate biasing during plasma-assisted ALD for crystalline phase-control of TiO 2 thin films, Electrochemical and Solid-State Letters. 15 (2012). https://doi.org/10.1149/2.024202esl.

[36] H.B. Profijt, M.C.M. van de Sanden, W.M.M. Kessels, Substrate-biasing during plasma-assisted atomic layer deposition to tailor metal-oxide thin film growth, Journal of Vacuum Science & Technology A: Vacuum, Surfaces, and Films. 31 (2013) 01A106. https://doi.org/10.1116/1.4756906.

[37] A.C. Kummel, A. McLeod, S.T. Ueda, Deposition of Large-Grain Polycrystalline Aluminum Nitride at Low Temperature Via Bias-Enhanced Atomic Layer Annealing, ECS Meeting Abstracts. MA2020-02 (2020). https://doi.org/10.1149/ma2020-02251793mtgabs.

[38] J.K. Sprenger, A.S. Cavanagh, H. Sun, K.J. Wahl, A. Roshko, S.M. George, Electron Enhanced Growth of Crystalline Gallium Nitride Thin Films at Room Temperature and 100 °c Using Sequential Surface Reactions, Chemistry of Materials. 28 (2016) 5282–5294. https://doi.org/10.1021/acs.chemmater.6b00676.

[39] S. Banerjee, A.A.I. Aarnink, D.J. Gravesteijn, A.Y. Kovalgin, Thermal atomic layer deposition of polycrystalline gallium nitride, Journal of Physical Chemistry C. 123 (2019) 23214–23225. https://doi.org/10.1021/acs.jpcc.9b05946.

[40] A.C. Liu, K.J. Singh, Y.M. Huang, T. Ahmed, F.J. Liou, Y.H. Liou, C.C. Ting, C.C. Lin, Y. Li, S. Samukawa, H.C. Kuo, Increase in the Efficiency of III-Nitride Micro-LEDs: Atomic-Layer Deposition and Etching, IEEE Nanotechnol Mag. 15 (2021) 18–34. https://doi.org/10.1109/MNANO.2021.3066393.

[41] P.J. Parbrook, B. Corbett, J. Han, T.-Y. Seong, H. Amano, P.J. Parbrook, B. Corbett, T.-Y. Seong, H. Amano, Micro-Light Emitting Diode: From Chips to Applications, n.d. www.advancedsciencenews.com.

[42] H. Jiang, J. Lin, Development of nitride microLEDs and displays, in: Semiconductors and Semimetals, Academic Press Inc., 2021: pp. 1–56. https://doi.org/10.1016/bs.semsem.2021.01.006.

[43] S.P. Denbaars, Gallium-Nitride-Based Materials for Blue to Ultraviolet Optoelectronics Devices, 1997.

[44] L. Shen, S. Heikman, B. Moran, R. Coffie, N.Q. Zhang, D. Buttari, I.P. Smorchkova, S. Keller, S.P. DenBaars, U.K. Mishra, AlGaN/AlN/GaN high-power microwave HEMT, IEEE Electron Device Letters. 22 (2001). https://doi.org/10.1109/55.954910.

[45] C.R. Eddy, T.J. Anderson, A.D. Koehler, N. Nepal, D.J. Meyer, M.J. Tadjer, R. Baranyai, J.W. Pomeroy, M. Kuball, T.I. Feygelson, B.B. Pate, M.A. Mastro, J.K. Hite, M.G. Ancona, F.J. Kub, K.D. Hobart, GaN Power Transistors with Integrated Thermal Management, ECS Trans. 58 (2013). https://doi.org/10.1149/05804.0279ecst.

[46] J.T. Chen, J. Bergsten, J. Lu, E. Janzén, M. Thorsell, L. Hultman, N. Rorsman, O. Kordina, A GaN-SiC hybrid material for high-frequency and power electronics, Appl Phys Lett. 113 (2018). https://doi.org/10.1063/1.5042049.

[47] S.J. Liu, Y.F. He, H.Y. Wei, P. Qiu, Y.M. Song, Y.L. An, A. Rehman, M.Z. Peng, X.H. Zheng, PEALD-deposited crystalline GaN films on Si (100) substrates with sharp interfaces, Chinese Physics B. 28 (2019). https://doi.org/10.1088/1674-1056/28/2/026801.

[48] H.Y. Shih, M.C. Lin, L.Y. Chen, M.J. Chen, Uniform GaN thin films grown on (100) silicon by remote plasma atomic layer deposition, Nanotechnology. 26 (2015). https://doi.org/10.1088/0957-4484/26/1/014002.

[49] A.M. El-Naggar, S.Y. El-Zaiat, S.M. Hassan, Optical parameters of epitaxial GaN thin film on Si substrate from the reflection spectrum, Opt Laser Technol. 41 (2009) 334–338. https://doi.org/10.1016/j.optlastec.2008.05.022.

[50] D.M. Hoffman, S. Prakash Rangarajan, S.D. Athavale, D.J. Economou, J. Liu, Z. Zheng, W. Chu, Chemical vapor deposition of aluminum and gallium nitride thin films from metalorganic precursors, Journal of Vacuum Science & Technology A: Vacuum, Surfaces, and Films. 14 (1996) 306–311. https://doi.org/10.1116/1.579893.

[51] N. Ihashi, K.-I. Itoh, O. Matsumoto, Deposition of Gallium Nitride Thin Films by MOCVD in Microwave Plasma, 1997.

[52] I. Saraswati, A. Stolz, S. Ko, E. Dogheche, N.R. Poespawati, R. Wigajatri, D. Decoster, Optical properties of gallium nitride heterostructures grown on silicon for waveguiding

application, in: Adv Mat Res, Trans Tech Publications Ltd, 2014: pp. 41–45. https://doi.org/10.4028/www.scientific.net/AMR.980.41.

[53] R. Dylewicz, S. Patela, R.A. Hogg, P.W. Fry, P.J. Parbrook, R. Airey, A. Tahraoui, In-plane optical anisotropy of GaN refractive index in visible light region, IEEE Photonics Technology Letters. 21 (2009) 966–968. https://doi.org/10.1109/LPT.2009.2021150.

CHAPTER 4

High Thermal Conductivity of Sub-Micron Aluminum Nitride Thin Films Sputter-Deposited at Low Temperature

4.1 Abstract:

Aluminum nitride (AlN) is one of the few electrically insulating materials with high thermal conductivity, but high-quality films typically require high deposition temperatures >800 ˚C. For thermal management applications in dense or high-power integrated circuits, it is important to deposit heat spreaders at lower temperatures without affecting the underlying electronics. Here we demonstrate 100 nm to 1.7 um thick AlN films achieved by low-temperature (<100 ˚C) sputtering, correlating their thermal properties with their grain size and interfacial quality, which we analyze by x-ray diffraction, transmission x-ray microscopy, Raman and Auger spectroscopy. Controlling the deposition conditions through the ratios of inert Ar with reactive N_2 demonstrates a ~3x variation in thermal conductivity (36-104 $Wm^{-1}K^{-1}$) of ~600 nm films, with the upper range representing a record for such film thicknesses at room temperature. Defect densities are estimated from the thermal conductivity measurements, providing insight into the thermal engineering of AlN that can be optimized for application-specific heat spreading or thermal confinement.

4.2 Introduction:

The generation of heat impedes the performance and longevity of nearly all modern electronic devices [1–3]. This is especially true in high-density integrated circuits [4] and power or radio frequency (RF) electronics [3,5], where elevated temperatures reduce transistor performance, increase leakage, and ultimately diminish the device lifetime [6–8]. A mere 5 ˚C increase in temperature above the optimum operating range can halve the lifetime of a device [7,9].

Thermal management could be achieved by actively tuning heat flow and managing thermal transients, e.g. with the use of emerging thermal transistors and diodes [10–12]. Passive approaches involve simply using thin films to block or route heat away from hot spots in electronics. Such heat spreaders must have high thermal conductivity while being electrical insulators to isolate devices - a set of properties that are common only to a few materials, like aluminum nitride, boron nitride, and diamond.

In particular, AlN has attracted much attention due to its large band gap (6.1 eV) [13,14] and bulk thermal conductivity (~340 $Wm^{-1}K^{-1}$) [15,16]. Indeed, bulk-like thermal conductivities have been demonstrated for AlN films on the order of hundreds [16], tens [16,17], and several microns [17–20] in thickness, but such films are typically deposited at over 800 ˚C. High temperatures are incompatible with many requirements of fabricating integrated circuits, where low-temperature (<400 ˚C) deposition is required for back-end-of-line (BEOL) processes [21–23]. Moreover, integrated electronics would also benefit from thinner, microscale films of AlN, whose thermal conductivity has not been optimized, and their thermal limits remain poorly understood. Devices fabricated with AlN, for example, can be compositionally complex and the literature remains unclear as to the dominant phonon scattering mechanisms in sub-micron versions of these materials [24,25]. In general, there is a lack of systematic investigation surrounding the generation of defects within AlN films that can be understood and utilized for thermal control.

In this work, AlN films are deposited by low-temperature (<100 ˚C) DC reactive balanced magnetron sputtering with thicknesses ranging from 100 nm to 1.7 μm. The thermal conductivity of the films is determined by time-domain thermoreflectance (TDTR) and is correlated with microstructural properties, such as grain size and morphology, as determined by x-ray diffraction

(XRD) and transmission electron microscopy (TEM), respectively. For films of roughly 600 nm in thickness, the thermal conductivity can be tuned by a factor of three by controlling the sputtering gas composition during deposition, with the upper end ~104 $Wm^{-1}K^{-1}$ representing a record value for this thickness range at room temperature. Comparing these results with models based on the Boltzmann Transport Equation (BTE) for phonons show that defect densities are being modulated over an order of magnitude, resulting in the observed large range in film thermal conductivity.

4.3 Materials and Methods

4.3.1 AlN Film Deposition

The AlN films were deposited in a home-built vacuum chamber system comprised of a load lock and sputtering chamber, each pumped by individual turbomolecular pumps with base pressures 4×10^{-7} Torr and 1×10^{-7} Torr, respectively.

The Silicon (111) and c-Al_2O_3 substrates were used in this work were prepared by a degrease with acetone, methanol, and water followed by three cycles of an HF etch consisting of submersion in 2% HF for 30 seconds and rinsing with deionized water for 30 seconds. All substrates were dried under N_2. The sapphire substrates were cleaned using the same degrease process followed by a 20 minute etch in a 3:1 bath of sulfuric acid and phosphoric acid held at 80 °C. Following the etch, sapphire substrates were rinsed with deionized water for 15 seconds before drying under N_2. The substrate coupons were then loaded into the load-lock chamber for pump down; substrates were only transferred into the sputter chamber after the load-lock had reached its base pressure.

A 2” Al target (99.999%, Kurt J. Lesker Co.) was attached to the sputter cathode (Torus MagKeeper 2, Kurt J. Lesker Co., balanced magnetron configuration) which was fitted with a

pneumatic shutter. The target to substrate distance was approximately 10 cm. The substrates were transferred into the sputtering chamber under 20 sccm of Ar and were placed on a grounded copper stage with integrated water-cooling capability. The chamber pressure was brought to 6 mTorr with Ar for a two minute target cleaning at 100 W DC. Following this clean, a ramp to the desired N_2/Ar gas composition at approximately 3 mTorr pressure was performed over approximately two minutes. Select depositions were repeated using Kr in place of Ar. A brief pre-sputter of approximately 30 seconds was performed against the target shutter before beginning reactive sputter deposition using 100 W DC. Growth rates ranged from ~4-6 nm/min in this configuration.

The Ar, and N_2 gasses were obtained from AirGas (99.99%); Kr was obtained from Praxair all gas flows were controlled by a home-built system of mass flow controllers and were purified by an Entegris GateKeeper mounted just before the gas inlet to remove trace oxygen and water contaminants. Pressures were measured using a capacitance manometer (Kurt J. Lesker Co.) mounted on the body of the sputtering chamber.

AlN films were deposited using balanced DC sputtering [29,30], as depicted in Figure 3.1a. Two series of AlN films were deposited (Figure 3.1b); the first used a standard gas composition of 25% Ar and 75% N_2 with film thicknesses of 685 nm, 1156 nm, and 1735 nm on both Si(111) and c-Al_2O_3 substrates. The data for these films are summarized in Table 3.1.

The second series of films approximately 600 nm in thickness were grown to demonstrate the tunability of the room temperature (RT) thermal conductivity (κ) via manipulation of the sputtering gas composition. Deposition details for these films can be found in Table 3.2 using both Si(111) and c-sapphire substrates with gas compositions varied from 19% to 41% Ar and 58% to 80% N_2, shown in Figure 3.1b. Two of the samples in this series were deposited using a 10 ˚C cooled stage during deposition.

An 80 nm Al film was then deposited on top of all the samples via electron beam evaporation (AJA International Inc., ATC-E Series) to facilitate thermal measurements by acting as an optothermal transducer. Deposited at a nominal chamber pressure of 9.8×10^{-7} Torr with a 0.5 Å s^{-1} deposition rate, the thickness of the Al films was determined via scanning electron microscopy (SEM).

4.3.2 Diffraction, Ellipsometry, and Transmission Electron Microscopy

Following deposition of the AlN films, all samples were analyzed by Bragg-Brentano x-ray diffraction (XRD) to assess their crystallinity using a Rigaku Smartlab system (Cu anode operating at 2 kW). Grain sizes were estimated by the Debeye-Scherrer formula based on AlN (002) diffraction peak full-width at half max (FWHM) fits determined using Rigaku GlobalFit software. This is given by:

$$C.S. = \frac{0.94\lambda}{\beta cos(\theta)}$$

where C.S. is the estimated crystallite size, λ is the x-ray wavelength, β is the peak FWHM in radians, and θ is the diffraction angle. We note that although this model was originally intended for powders, the estimated crystallite sizes, i.e. grain sizes, provided are intended solely for comparative purposes within our datasets.

The thickness of the sputtered films was measured using a J.A. Woollam M-2000D spectroscopic ellipsometer at 75˚ incidence angle across 500 wavelengths from 190 nm to 1000 nm.

Lamellae from select samples on c-sapphire substrates were prepared using a focused ion beam system with final thinning to ~35 nm by Eurofins EAG Laboratories (Sunnyvale, CA).

Transmission electron microscopy (TEM) and high-resolution TEM (HR-TEM) was performed using a ThermoFisher Talos F200X G2 instrument equipped with a Ceta CMOS camera and double-tilt sample holder. All image processing and fast Fourier transform (FFT) analysis was performed using Gatan Microscopy Suite.

4.3.3 Time-Domain Thermoreflectance

The thermal conductivity of the AlN films was measured with time-domain thermoreflectance (TDTR), an optical pump-probe method used extensively to determine the thermal properties of nanoscopic materials [26–28]. The focused radii of the beams were determined through knife-edge measurements and measured to be 5.36 ± 0.1 and 3.19 ± 0.05 for the pump and probe, respectively. A pump power of 9.5 mW was utilized and modulated with a frequency of 10 MHz. The probe, set to 3 mW, was focused concentrically with the pump onto the sample surface using a 20× objective lens. Thermoreflectance data were then fit to the solution of a 3D heat diffusion model for a multi-layer stack of materials and the unknown properties of interest are used as parameters to converge measurement and theory.

We note that all controlled parameters were obtained from either independent measurements or from the literature. As such, the thermal conductivity of our Al transducer and substrates were independently determined with TDTR. The thickness of the Al transducer was provided by scanning electron microscopy (SEM) using a our reference Si(111) substrate sample to avoid substrate charging. The resulting uncertainties for independent measurements were inputted into a thermal model to produce the total uncertainty of the measurement. The results are listed in Table 3.3.

The measurable properties in a TDTR measurement critically depend on the sensitivity of the measured signal to said properties when described by a multilayer heat diffusion model. As such, the sensitivity of the measured TDTR signal to an unknown property x is defined as

$$S_x = \frac{\partial ln(MS)}{\partial ln(x)}$$

where MS is the measured signal, the ratio (V_{in}/V_{out}) in this work. As discussed briefly in the main text, sensitivity calculations were performed for AlN thin film system considering both Si(111) and c-Al_2O_3 substrates. Input properties for these calculations are summarized in Table 3.3, where we applied typical AlN/substrate and Al/AlN thermal boundary conductances of 200 $MWm^{-2}K^{-1}$. We assumed 20, 40, and 80 $Wm^{-1}K^{-1}$ for the 100, 600, and 1700 nm films, respectively.

4.4 Results and Discussion

4.4.1 Experiment Design

The films were characterized by Bragg-Brentano x-ray diffraction (XRD), an example of which is shown for the set of films with varied thickness in Figure 4.1 (c). In addition, high-resolution transmission electron microscopy (HR-TEM) was performed on the most thermally dissimilar samples. Time domain thermoreflectance (TDTR), seen in Figure 4.1 (d-f), was performed on all films.

A schematic of the AlN film specimens measured in this work are displayed in Figure 4.1 (d), consisting of an aluminum (Al) opto-thermal transducer, an AlN film, and a Si(111) or c-Al_2O_3 substrate. Thermal properties were determined by TDTR, an optical pump-probe technique described extensively in prior works [26–28]. In TDTR, an ultra-fast laser is used to both induce (pump) and monitor (probe) modulated heating on the surface of sample as a function of pump-

probe time-delay. The thermal conductivity and thermal boundary conductances are then determined by fitting the intensity of the ratio V_{in}/V_{out} to a 3D heat diffusion model for a multi-layer stack of materials. Given the measurement conditions provided in section 4.3.3, the measurement is primarily sensitive to cross-plane thermal conductivity as shown by the sensitivity calculations displayed in Figure 4.1 (e), which show the sensitivity to the relevant properties for 100-1700 nm AlN films on an Si(111) substrate. This is attributed to the disparity between the root-mean-square (RMS) average laser spot radius w_{RMS} and the in-plane thermal penetration depth that induces 1D heat transfer [31].

The high thermal conductivity and sub-micron thicknesses of these AlN films complicate the extraction of thermal properties and thus warrant an optimization approach. As the thermal penetration into the sample becomes comparable to the film thicknesses, the thermal boundary conductances on either side of the film increasingly influence the total thermal resistance of the measured system. As seen in Figure 4.1 (e), both the Al/AlN and AlN/Si interfaces contribute prominently to the thermal response for a 100 nm AlN film, while the AlN-Si interface becomes insensitive with a 1700 nm AlN film, i.e. it is thermally thick. For the ~600 nm films, however, the contribution of the AlN/Si interface is diminished but still significant. Films on c-Al_2O_3 were analyzed in a similar manner but with slightly greater uncertainties in the thermal interfaces due to the increased contribution of the substrate to the probed thermal resistance [33]. Input material characteristics and resulting sensitivity analyses for all fitting can be found in Table 4.3 and Figure 4.2.

4.4.2 Benchmarking

Cross-plane thermal conductivities for these AlN films are provided in Figure 4.3 (a) with deposition temperature and are compared to values reported in the literature [17–19,32,34–40]. Here, films are distinguished by their thickness: red, green, and blue symbols for films greater than 2 μm, 1-2 μm, and less than 1 μm in thickness, respectively. In addition to the relatively low deposition temperature of the films in this study, reaching temperatures of less than 100 ˚C during deposition due to plasma exposure (the stage was not actively heated), represent some of the highest reported thermal conductivities for AlN films in the sub-micron regime. Further, the depositions performed with the stage cooled to 10 ˚C are estimated to have been deposited at 70 ˚C due to ambiguity in the sample temperature as a result of thermal gradients. In contrast, most chemical and physical deposition methods rely on heating substrates to several hundred degrees Celsius to effectively crystallize deposited material, in turn producing films with greater thermal conductivity.

The thermal conductivity of our AlN films sputtered at BEOL-compatible temperatures are compared with results from other works as a function of film thickness in Figure 4.3 (b); these results are represented by filled symbols that are either red or blue, for films on c-Al_2O_3 and Si(111), respectively. In the sub-micron regime, the high thermal conductivity of our films indicates decreased defect density and reduced boundary scattering effects that typically plague non-epitaxial thin films, regardless of deposition technique. Indeed, minimizing defect densities and promoting the growth of larger grains is the primary focus of thin film synthesis in electronic heat-spreading applications [41,42]. However, the integration of materials with a wide range of thermal conductivities at low temperatures is desired for strategic heat spreading or thermal confinement, exemplified by the yellow shaded region in Figure 4.3 (b) showing the range of

thermal conductivities achieved via sputtering gas manipulation. Figure 4.3 (c) magnifies this region to show that the AlN thermal conductivity for the set of ~600 nm films can range from 104 to 36 $Wm^{-1}K^{-1}$; a nearly three-fold change.

4.4.3 Time Domain Thermoreflectance Results

The modulation of thermal conductivity in these AlN films by tuning the sputtering gas composition was employed to understand the underlying mechanisms of improvement. Figure 4.4 (a) plots the thermal conductivity with respect to N_2 gas concentration of the ~600 nm films on both c-Al_2O_3 and Si(111) in red and blue, respectively, with open symbols representing samples deposited using a cooled stage. Note that the balance gas is Ar such that it comprises the full gas mixture, i.e. Ar (%)=1-N_2 (%). Deposition on a non-cooled stage with lower N_2 concentrations of 59% to 75% yielded lower thermal conductivity values <50 $Wm^{-1}K^{-1}$. Conversely, an 80% N_2 deposition environment produced the most thermally conductive film among those that were not cooled. This is in contrast to work by Shinoda et al., who implemented a low N_2 concentration of 30% to produce films of high crystallinity, though with RF reactive magnetron sputtering and substrate temperatures exceeding 900 ˚C [43]. Conversely, Kumada et al. reported optimal N_2 concentrations of 40-50%, but with lower substrate temperatures of approximately 500 ˚C [44]. The general trend between higher N_2 concentrations and lower substrate temperatures in the literature and in this work, highlights the complex interplay of sputtering yield and reactive species present in the plasma with the substrate, where both thermal energy from heating and surface bombardment with various species determine the properties of the deposited film.

Depositions performed using the cooled stage produced the most thermally conductive films in this work and some of the largest values reported in the field. Average grain sizes are

provided in Figure 4.4 (b), estimated using the FWHM of the AlN (002) diffraction peak and the Debye-Scherrer Equation, and reveal a positive correlation between crystallite size and thermal conductivity. Such a trend is consistent with decreased phonon scattering at grain boundaries, which is often the dominant scattering mechanism in dielectrics and semiconductors [45]. For clarity, these data are combined in Figure 4.4 (c) to show the generally positive correlation between thermal conductivity, nitrogen content, and average crystallite size. It is well established that increasing the substrate temperature enhances surface migration and thus, crystalline quality. However, increased compressive stress at the AlN/substrate interface can occur during the post-deposition cooling process [44], which can play a major role in determining overall crystallinity [46].

4.4.4 Transmission Electron Microscopy

TEM was performed on three films deposited on c-Al_2O_3 to gain insight into the microstructural features that influence transport. Figure 4.5 shows cross sections of two films deposited without stage cooling: (a) the most thermally insulating film deposited using 66% N_2, and (b) a film deposited using 75% N_2 with a larger thermal conductivity value. Grain boundaries are outlined to reveal a noticeable difference in their size and frequency, in agreement with both the estimated crystallite sizes and the thermal conductivity values (~38 and ~50 $Wm^{-1}K^{-1}$, respectively). Figure 4.5 (c) is shown to isolate the effect of the cooled stage since it was also deposited using 75% N_2. With crystallite sizes of roughly 70 nm, this film is also the most thermally conductive reported in this work (~104 $Wm^{-1}K^{-1}$) and clearly exhibits larger grains than either of the films presented.

Further inspection of the HR-TEM images suggests that the state of the film-substrate interface is a potential driver for transport, as shown in Figure 4.6. Analysis by fast Fourier transform (FFT) is provided for each film in three different near-interface regions (I-III) and for each underlying c-Al_2O_3 substrate (IV) for comparison. An amorphous layer develops at the AlN/c-Al_2O_3 interface for the film deposited with 66% N_2, further confirmed by the presence of rings rather than discrete diffraction spots in Figure 4.6 (a), I-III. This amorphous layer may be the result of an excess of energetic Ar ions bombarding the growth surface during initial deposition, resulting in amorphization at the initial stages of growth, as observed in existing literature reports [19]. This effect is reduced for both films deposited using 75% N_2, using the non-cooled and cooled stages in Figure 4.6 (b) and (c), respectively. Both these films exhibit stronger crystallinity above the interface and an `abrupt' character that is more prominent still for the film deposited with a cooled stage. It is likely that the substrate cooling in Figure 4.6 (c) may have minimized adatom mobility during the initial growth, considering established qualitative models attributing such mobility to larger nucleation sites for crystal growth [44]. However, lower substrate temperatures can also provide a more favorable thermodynamic environment for the formation of nuclei, thereby leading to the formation of more uniformly sized and evenly distributed crystallites. Coupled with suspected reduced strain due to higher quality interfaces, both effects can lead to a more relaxed crystal lattice structure upon cooling, resulting in fewer defects and a more ordered crystal structure [47–49]. In practice, these effects are most easily observed in the larger and more uniformly sized crystallite columns in Figure 4.6 (c) as compared to Figure 4.6 (b).

4.4.5 Thermal Boundary Conductance Predictions

Thermal boundary conductance measurements of the AlN/substrate interface reaffirm our microstructural results and lend validity to the most thermally conductive films reported in this work. In Figure 4.7, the extracted AlN/substrate thermal boundary conductance values are compared with predictions from the diffuse mismatch model (DMM) [50,51] with a Born von Karman (BVK) phonon dispersion approximation. The DMM thermal boundary conductance G_{DMM} from material A to B is given by:

$$G_{A\to B} = \frac{1}{4}\sum_{j}\int_{0}^{\infty} v_{Aj}\,\hbar\omega\,D_A(\omega)\frac{\partial f_{BE}^{0}\,(\omega,T)}{\partial T}\alpha_{A\to B}\,d\omega$$

where j is the phonon branch, v is the phonon velocity in material A, $D_A(\omega)$ is the phonon density of states in material A, $f_{BE}^{0}\,(\omega,T)$ is the Bose-Einstein equilibrium function, and $\alpha_{A\to B}$ is the transmissivity from material A to B. Despite the DMM's inability to capture atomic-scale interface characteristics [52], it is in broad agreement with our measured values for samples deposited with a non-cooled stage, ranging from ~170 to ~280 $MWm^{-2}K^{-1}$. However, the general effect of a cooled stage is to increase the AlN/substrate thermal boundary conductance, seen as the open symbols in Figure 4.7. This increase is more notable for AlN on c-Al_2O_3, which is also the substrate that produced our most thermally conductive film attributed to more favorable lattice matching compared to Si(111). Indeed, stage cooling also increased the AlN/substrate thermal boundary conductance of films deposited with Kr gas in place of Ar, thus reinforcing this trend. Though large uncertainties prevent a more decisive conclusion due to suppressed sensitivities typical of embedded interfaces, the sharp increase of thermal boundary conductances is evident. This is important from a device perspective, where high quality interfaces not only promote crystalline growth, but can also dissipate more thermal energy to mitigate high operating temperatures and hot spots [27].

4.4.6 Boltzmann Transport Modeling

The underlying phonon scattering mechanisms in these AlN films were analyzed via an analytical model based on the Boltzmann transport equation (BTE). We employed a treatment of the BTE in a paradigm similar to past works [16,53–55]

$$\kappa = \frac{1}{3}\, Cv\lambda = \frac{1}{3}\sum_{j}\int_{0}^{\omega_{max}} \hbar\omega\; D(\omega)\frac{\partial f_{BE}^{0}\;(\omega,T)}{\partial T}\; v_j^2\; \tau_j(\omega)\; d\omega$$

where C is the volumetric heat capacity, λ is the phonon mean free path, ω_{max} is the Debeye cutoff frequency, and $\tau\ (\omega)$ is the phonon relaxation time. Umklapp, defect, and boundary scattering comprise the relaxation time and are summed in accordance to Matthiessen's rule. Specifically, the point defect scattering rate can be expressed as [56]:

$$\frac{1}{\tau_D} = \frac{V}{4\pi v^3}\;\omega^4\;\sum_{i} f_i\left(\frac{m-m_i}{m}\right)^2$$

where f_i is the fractional concentration of the i^{th} impurity atom, and m and m_i are the masses of original and i^{th} impurity atoms, respectively. We make an important simplification in light of previous studies [16,57] that suggest Al vacancies play a dominant role due to the large atomic mass difference between Al and common impurities (e.g. Si, O, C, and N atoms). As such, the Al defect density is used as a fitting parameter in conjunction with our experimental data.

The foregoing BTE model sheds light on the degree of defect modulation occurring in our AlN films, shown in Figure 4.8 (a). Here, a solid black line is provided to indicate the model behavior in the limit of no defects, and a fit of the model to the thickness-dependent experimental data using the standard 75% N_2 composition is also shown for comparison. Remarkably, changing the sputter gas composition alters the defect densities in the present films by over an order of magnitude, from $1.6\text{x}10^{20}$ to $1.9\text{x}10^{21}$ cm^{-3}. Such values are in agreement with similar predictions

for AlN films, though the purest films still possess a defect density an order of magnitude larger than bulk [16].

4.4.7 Further Context

Finally, Figure 4.8 (b) provides a landscape of other materials used in electronic devices with respect to deposition temperature [16,58–68]. There is a clearly negative correlation between the thermal conductivity and deposition temperature in all the materials shown that is emphasized by the multi-colored arrow. In this context, materials exhibiting both high thermal conductivity and electrical resistivity deposited at low temperatures are desirable, especially with subsequent annealing steps that can introduce atomic diffusion and severe thermal stresses between dissimilar materials. Our results substantiate the modulation of thermal conductivity while maintaining <500 ˚C BEOL temperatures using WBG materials, and are thus attractive candidates for integration in electronic device applications requiring high operating frequencies and the handling of high power density [3,5].

4.5 Conclusion

To conclude, we use sputter deposit AlN films ranging from 100 nm to 1.7 μm in thickness on Si(111) and c-Al_2O_3 substrates at low temperature (<100 ˚C). At thicknesses of roughly 600 nm, a ~3x change in thermal conductivity was observed by controlling the sputtering gas composition during deposition. We elucidated these effects via direct characterization with XRD, TEM, and HR-TEM and are complemented by thermal conductivity measurements performed by TDTR. These results are further investigated using analytical models based on the Boltzmann Transport Equation and reveal estimated defect densities varying over an order of magnitude.

Record high thermal conductivity values are reported for depositions performed using a cooled stage, which demonstrated improved film morphology. Across the entire sample set, correlations between thermal conductivity and microstructure confirm the importance of grain size and the quality and uniformity of the interfacial crystallinity, which are further reinforced by measurements of thermal boundary conductance. Overall, these results show the potential of wide-bandgap semiconductors as thermal routing materials with BEOL-compatible deposition parameters. Understanding the nature and origins of thermal transport is not only theoretically important with regard to scattering dynamics, but increasingly technologically relevant for application-specific strategic heat spreading or thermal confinement.

4.6 Acknowledgements

This work was supported in part by the Applications and Systems-Driven Center for Energy Efficient Integrated Nano Technologies (ASCENT), one of six centers in the Joint University Microelectronics Program (JUMP), an Semiconductor Research Corporation (SRC) program sponsored by the Defense Advanced Research Program Agency (DARPA). This work was performed in part at the San Diego Nanotechnology Infrastructure (SDNI) at UC San Diego, a member of the National Nanotechnology Coordinate Infrastructure, which is supported by the National Science Foundation (ECCS-1542148). Part of this work was performed at the Stanford Nano Shared Facilities (SNSF), supported by the National Science Foundation under award ECCS-1542152. The authors acknowledge the use of the SNSF of Stanford University for sample preparation and characterization.

Chapter 4, in part, is being prepared for publication of which the dissertation author was a primary researcher and coauthor:

McLeod, Aaron J. and Perez, Christopher; Chen, Michelle; Yi, Su-in; Vaziri, Sam; Hood, Ryan; Ueda, Scott T.; Bao, Xinyu; Asheghi, Mehdi; Park, Woosung; Talin, A. Alec; Kumar, Suhas; Pop, Eric; Kummel, Andrew C.; Goodson, Kenneth E. "High Thermal Conductivity of Sub-Micron Aluminum Nitride Thin Films Sputter Deposited at Low Temperature"

Table 4.1 Sputtered AlN Films with Varied Thickness. Thickness, thermal conductivity, AlN (002) diffraction peak width, and estimated grain size for films of varied thickness deposited using a 75% N_2 and 25% Ar mixture on a non-chilled sample stage.

Substrate	d [nm]	κ [W m^{-1} K^{-1}]	(002) FWHM [$^\circ$]	C.S. [nm]
Si(111)	100	18.7 ± 4.6	0.998	9.0
	300	25.5 ± 4.7	0.660	13.2
	647	51.1 ± 5.0	0.260	33.6
	800	48.1 ± 6.4	0.620	14.0
	1156	124.3 ± 19.4	0.194	45.2
	1735	125.7 ± 21.4	0.186	47.0
c-Al_2O_3	647	68.1 ± 8.6	0.207	42.2
	1156	122.8 ± 20.4	0.195	44.8
	1735	118.9 ± 18.4	0.152	57.5

Table 4.2 Conditions for ~600 nm Thick Sputtered AlN Films. Deposition conditions, film thicknesses, thermal conductivities, AlN (002) diffraction peak full-width at half max values, and estimated grain sizes for the measured films deposited using various sputtering gas compositions.

Substrate	Cooled?	N_2%	Ar%	d [nm]	κ [W m^{-1} K^{-1}]	(002) FWHM [°]	C.S. [nm]
c-Al_2O_3		59	41	645	48.3 ± 5.0	0.262	33.3
		66	34	607	36.1 ± 3.8	0.303	28.8
		69	31	600	50.8 ± 6.2	0.185	47.2
		75	25	685	50.6 ± 3.3	0.168	52.0
	Y	75	25	670	103.9 ± 17.9	0.126	69.3
		80	20	639	74.9 ± 6.4	0.215	40.6
	Y	80	20	668	62.9 ± 6.9	0.222	39.4
Si(111)		59	41	645	43.2 ± 4.3	0.242	36.1
		66	34	607	38.1 ± 3.2	0.198	44.1
		69	31	600	50.2 ± 5.4	0.205	42.6
		75	25	685	43.7 ± 4.2	0.222	39.3
	Y	75	25	670	78.5 ± 10.3	0.168	52.0
		80	20	639	79.8 ± 5.5	0.177	49.3
	Y	80	20	668	66.9 ± 8.4	0.185	47.2

Table 4.3 Film Properties Table for Sputtering Gas Composition Study. Properties used to determine the cross-plane thermal conductivity ($\boldsymbol{\kappa_\perp}$) and boundary conductances ($\mathbf{G_s}$) of the AlN thin films. The volumetric heat capacities(ρ_{cp}) are taken from the literature and the thermal conductivity of the Al transducer ($\boldsymbol{\kappa_{Al}}$) was found from TDTR using companion samples during the Al deposition. The thicknesses for AlN and Al were measured with ellipsometry and scanning electron microscopy (SEM), respectively.

Material	ρ_{cp} [MJ m^{-3} K^{-1}]	$\kappa_\perp$ [Wm^{-1}K^{-1}]	$\kappa_\perp/\kappa_\parallel$	Film thickness [nm]
Al	2.44 ± 0.05	151.2 ± 25.0	1	81.1 ± 1.3
AlN	2.68 ± 0.08	$\kappa_{\perp,\mathrm{AlN}} \pm \sigma$	1	$100-1700$
Si	1.66 ± 0.09	142.0 ± 12.0	1	1×10^5
c-Al_2O_3	3.10 ± 0.09	42.5 ± 3.3	1	1×10^5

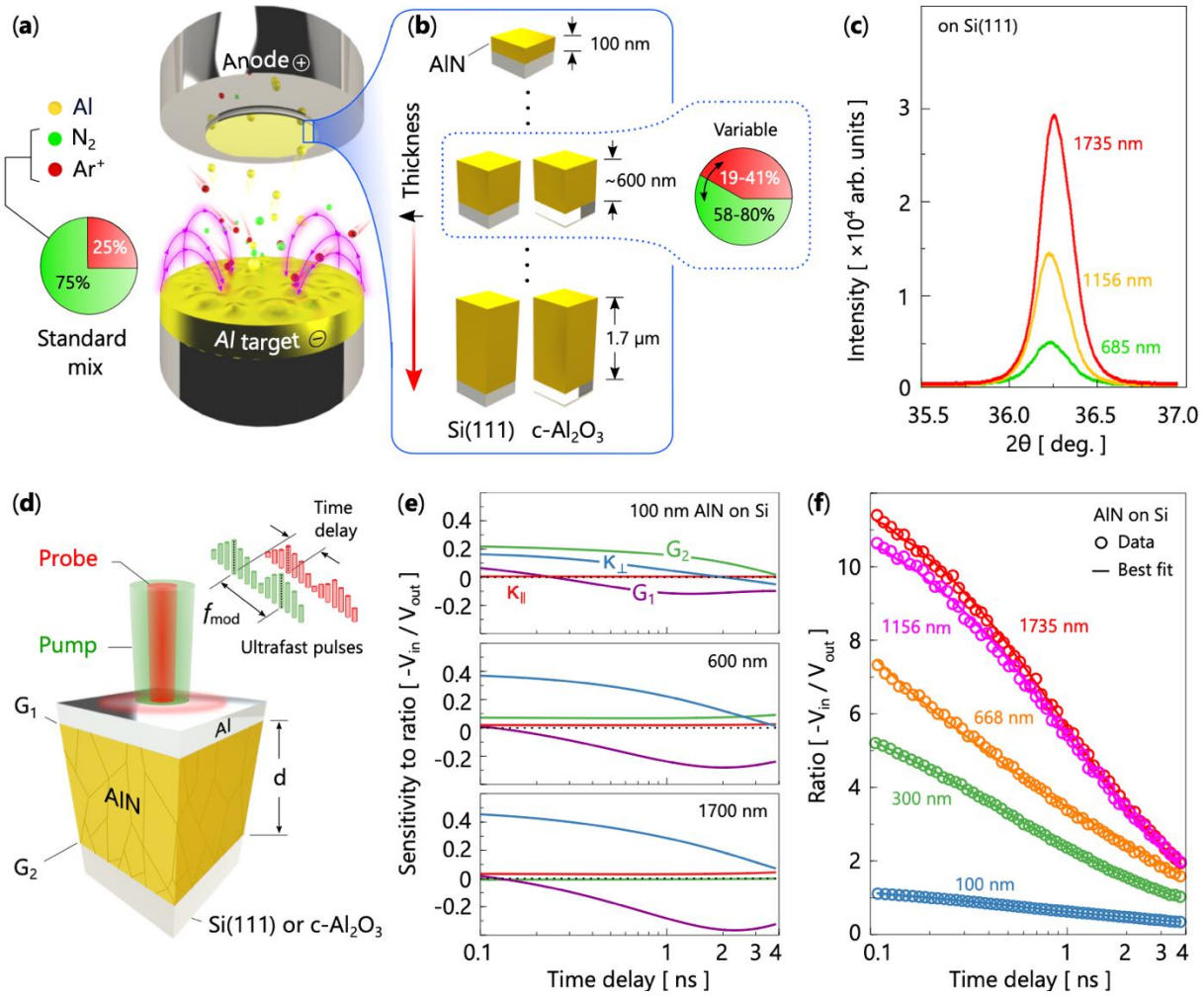

Figure 4.1 Experimental overview. (a) An illustration of our balanced DC magnetron sputtering deposition of AlN films using a standard sputter gas mix of 25% Ar and 75% N_2. (b) A schematic for the AlN film thickness variations explored in this work, along with their deposition on both Si(111) and c-Al_2O_3. The ~600 nm films are used to highlight the tuning of thermal transport via manipulation of the sputtering gas composition. (c) Bragg-Brentano x-ray diffraction (XRD) spectra are shown for the AlN films of various thicknesses deposited on Si(111), the results of which are used to estimate the grain size. (d) A simplified schematic of the TDTR measurement of the multilayer stack of materials used to determine thermal properties of the AlN films. (e) Sensitivity to the cross- and in-plane thermal conductivity $\kappa_\perp/\kappa_{||}$, Al-AlN thermal boundary conductance G_1, and AlN-substrate thermal boundary conductance G_2, and (f) characteristic model fits for the AlN films on Si ranging from 100 to ~1700 nm in thickness. Input properties for these calculations are given in Table 3.3.

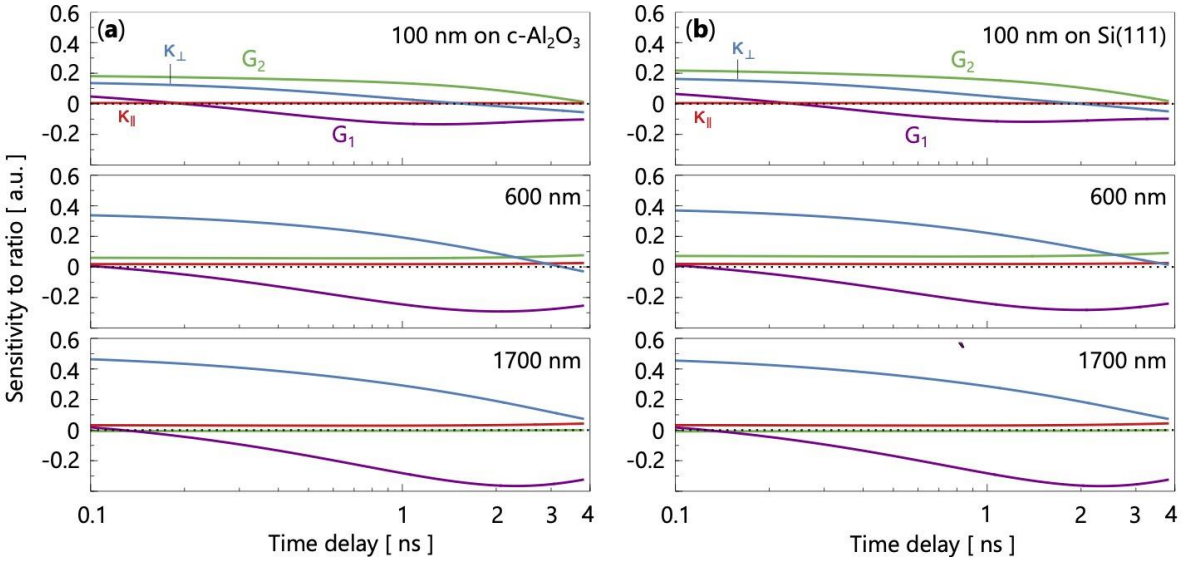

Figure 4.2 TDTR Sensitivity Analyses. The TDTR measurement sensitivity for the cross- and in-plane thermal conductivity ($\boldsymbol{\kappa_\perp}$ **and** $\boldsymbol{\kappa_\parallel}$), the Al/AlN thermal boundary conductance ($\boldsymbol{G_1}$), and the AlN/substrate thermal boundary conductance ($\boldsymbol{G_2}$) for AlN films on (a) c-Al_2O_3 and (b) Si(111). The thicknesses of the AlN films are provided in the insets.

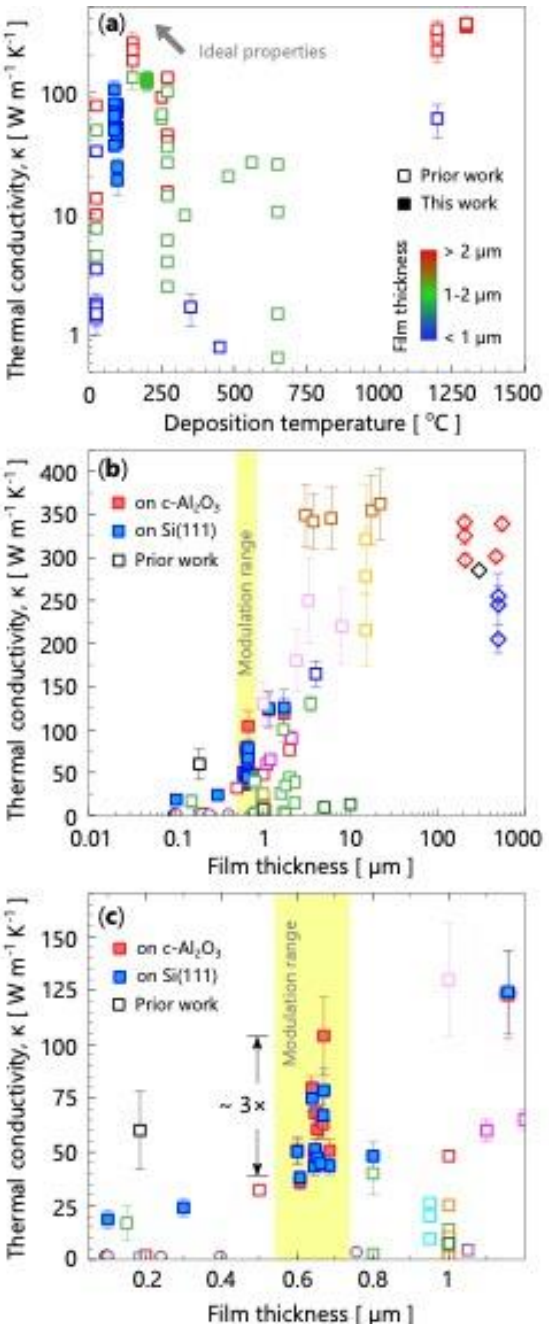

Figure 4.3 Literature Comparisons of AlN Thermal Conductivity Values. The room-temperature thermal conductivity of our AlN films (filled square symbols) as functions of (a) deposition temperature and (b) thickness with those from the literature. In (b), diamond symbols are single crystal samples: Slack [59] (black), Rounds [69] (red), and Xu [16] (blue). Square symbols are polycrystalline films: Kuo [19] (orange), Jacquot [70] (light blue), Zhao [34] (purple), Choi [35] (red), Duquenne [36] (green), Pan [37] (cyan), Aissa [38] (pink), Bian [39] (dark green), Yalon [40] (black), Cheng [17] (yellow), and Koh [18] (brown), Bellerk [71] (magenta). Round symbols correspond to amorphous thin films: Zhao [34] (purple) and Gaskins [72] (black). The yellow shaded region emphasizes the range of thicknesses with which we demonstrate the modulation of thermal conductivity, magnified in (c) to show a ~3x change.

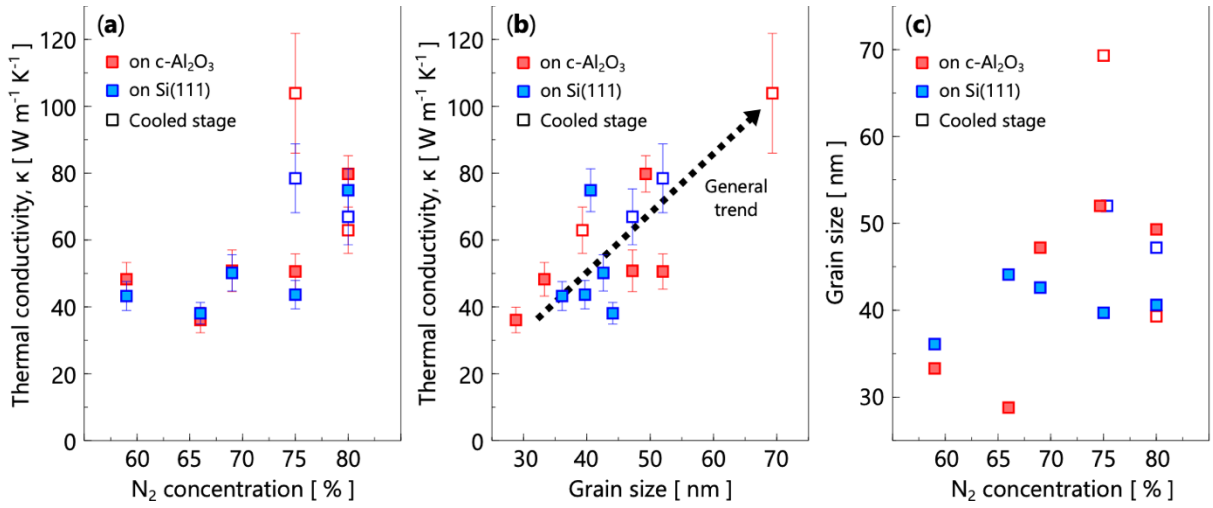

Figure 4.4 Thermal Conductivity and Correlation Analysis. Correlations between Thermal Conductivity, Grain Size, and Gas Composition for ~600 nm AlN Films (a) Thermal conductivity with respect to N_2 concentration and (b) grain size. The relationship between grain size and thermal conductivity is consistent with the importance of grain boundary scattering on thermal transport. Open squares represent films deposited on a cooled stage and exhibit the largest thermal conductivities. (c) Grain size with respect to N_2 concentration. We note that the data at 75% N_2 concentration is slightly offset for clarity.

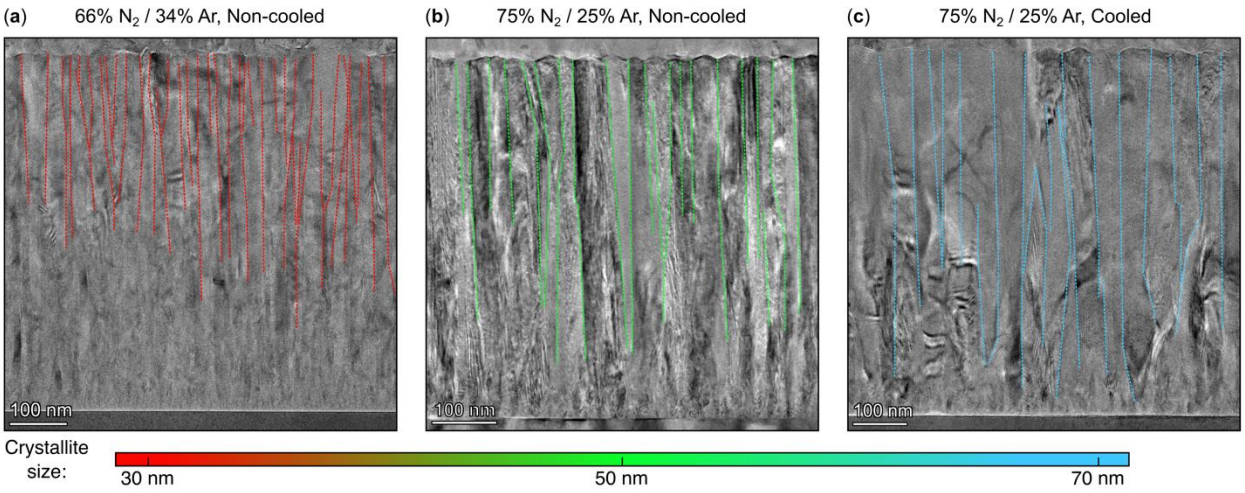

Figure 4.5 Grain Morphology Analysis by TEM. Transmission electron micrographs showing the full grain morphology for three sputtered films on c-Al_2O_3 using different conditions: (a) 66% N_2 and 34% Ar on a non-chilled stage, (b) 75% N_2 and 25% Ar without stage cooling (c) 75% N_2 and 25% Ar with the stage cooled to 10 ˚C throughout deposition. Grain boundaries are outlined to guide the eye.

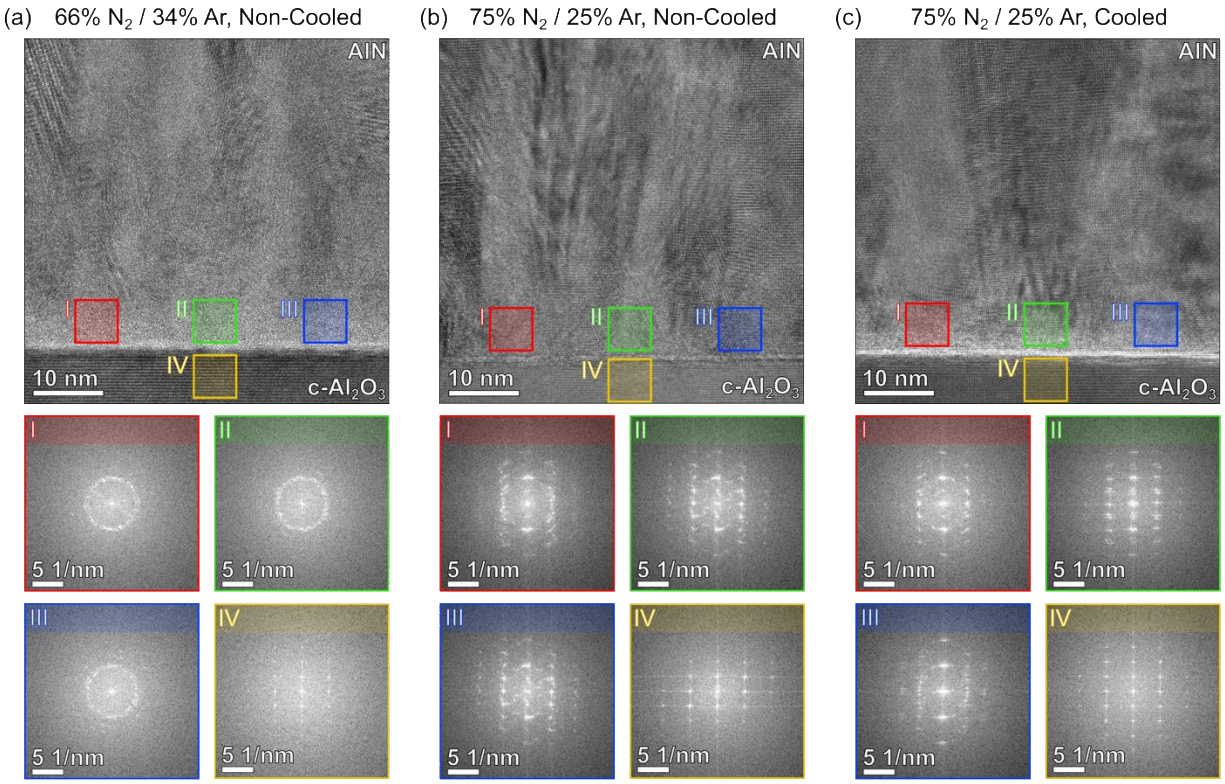

Figure 4.6 TEM and FFT Analysis of the Film-Substrate Interface. HR-TEM and FFT analysis of film crystalline at the substrate interface of three key films deposited on c-Al_2O_3 using different conditions: (a) 66% N_2 and 34% Ar on a non-chilled stage, (b) 75% N_2 and 25% Ar without stage cooling, (c) 75% N_2 and 25% Ar with the stage cooled to 10 ˚C throughout deposition.

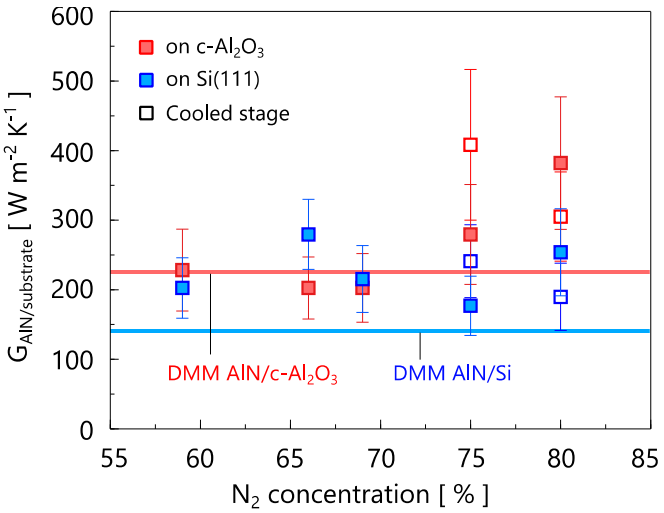

Figure 4.7 Thermal Boundary Conductance at the Film-Substrate Interface. The AlN/substrate thermal boundary conductances, G_2, determined for our AlN films deposited on both Si(111) and c-Al_2O_3. Note the increasing trend of the AlN-substrate thermal boundary conductance upon stage cooling suggesting the creation of a more well-matched interface, further reinforced by the TEM analysis in Figure 4.6.

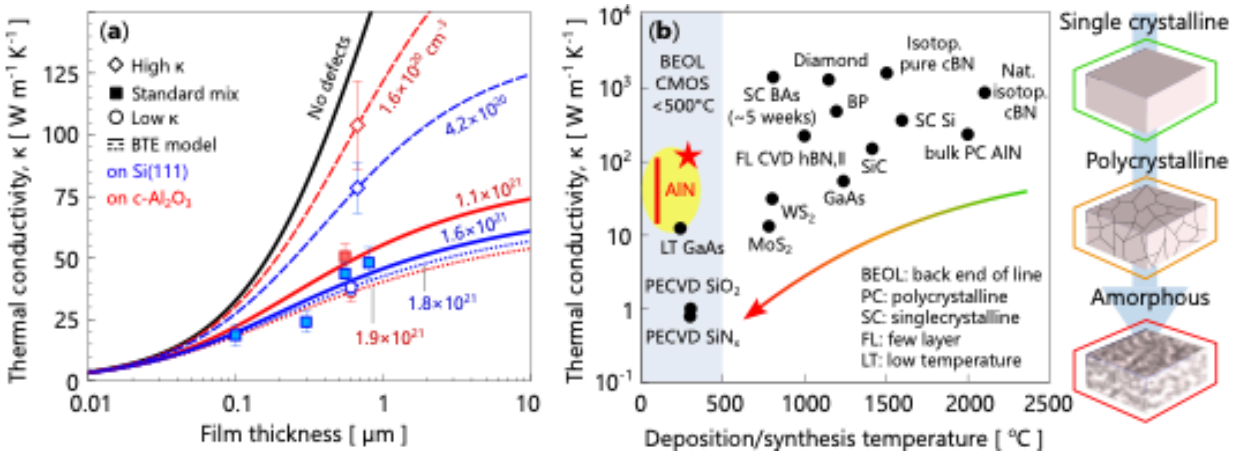

Figure 4.8 Estimated Defect Densities and Literature Comparisons. Thermal conductivity with respect to (a) film thickness and (b) deposition or synthesis temperature. In (a), the lines correspond to BTE predictions by fitting a defect density to the experimental data, revealing a modulation of roughly an order of magnitude. (b) A plot of thermal conductivity as a function of deposition temperature demonstrates the appeal for BEOL-compatible deposition of AlN films with high thermal conductivity relative to other materials commonly used in electronic devices [16,58–68].

4.7 References

[1] E. Pop, Energy dissipation and transport in nanoscale devices, Nano Res. 3 (2010) 147–169. https://doi.org/10.1007/s12274-010-1019-z.

[2] E. Pop, V. Varshney, A.K. Roy, Thermal properties of graphene: Fundamentals and applications, MRS Bull. 37 (2012) 1273–1281. https://doi.org/10.1557/mrs.2012.203.

[3] Y. Fu, J. Hansson, Y. Liu, S. Chen, A. Zehri, M.K. Samani, N. Wang, Y. Ni, Y. Zhang, Z. Zhang, Q. Wang, M. Li, H. Lu, M. Sledzinska, C.M.S. Torres, S. Volz, A.A. Balandin, X. Xu, J. Liu, Graphene related materials for thermal management, 2d Mater. 7 (2020) 1–42.

[4] M.M. Sabry Aly, M. Gao, G. Hills, C.-S. Lee, G. Pitner, M.M. Shulaker, T.F. Wu, M. Asheghi, J. Bokor, F. Franchetti, K.E. Goodson, C. Kozyrakis, I. Markov, K. Olukotun, L. Pileggi, E. Pop, J. Rabaey, C. Ré, H.-S.P. Wong, S. Mitra, Energy-Efficient Abundant-Data Computing: The N3XT 1,000x, Computer (Long Beach Calif). 48 (2015) 24–33. https://doi.org/10.1109/MC.2015.376.

[5] S.K. Oh, J.S. Lundh, S. Shervin, B. Chatterjee, D.K. Lee, S. Choi, J.S. Kwak, J.-H. Ryou, Thermal Management and Characterization of High-Power Wide-Bandgap Semiconductor Electronic and Photonic Devices in Automotive Applications, J Electron Packag. 141 (2019) 1–17. https://doi.org/10.1115/1.4041813.

[6] J. Xu, W. Yin, S. Member, J. Mao, S. Member, Transient Thermal Analysis of GaN Heterojunction Transistors (HFETs) for High-Power Applications, IEEE Microwave and Wireless Components Letters. 17 (2007) 55–57.

[7] G. Meneghesso, S. Member, G. Verzellesi, F. Danesin, F. Rampazzo, F. Zanon, A. Tazzoli, S. Member, M. Meneghini, S. Member, E. Zanoni, S. Member, Reliability of GaN High-Electron-Mobility Transistors : State of the Art and Perspectives, IEEE Transactions on Device and Materials Reliability. 8 (2008) 332–343.

[8] H. Amano, Y. Baines, E. Beam, M. Borga, T. Bouchet, P.R. Chalker, M. Charles, K.J. Chen, N. Chowdhury, R. Chu, C. De Santi, M.M. De Souza, S. Decoutere, L. Di Cioccio, B. Eckardt, T. Egawa, P. Fay, J.J. Freedsman, L. Guido, O. Häberlen, G. Haynes, T. Heckel, D. Hemakumara, P. Houston, J. Hu, M. Hua, Q. Huang, A. Huang, S. Jiang, H. Kawai, D. Kinzer, M. Kuball, A. Kumar, K.B. Lee, X. Li, D. Marcon, M. März, R. McCarthy, G. Meneghesso, M. Meneghini, E. Morvan, A. Nakajima, E.M.S. Narayanan, S. Oliver, T. Palacios, D. Piedra, M. Plissonnier, R. Reddy, M. Sun, I. Thayne, A. Torres, N. Trivellin, V. Unni, M.J. Uren, M. Van Hove, D.J. Wallis, J. Wang, J. Xie, S. Yagi, S. Yang, C. Youtsey, R. Yu, E. Zanoni, S. Zeltner, Y. Zhang, The 2018 GaN power electronics roadmap, J Phys D Appl Phys. 51 (2018). https://doi.org/10.1088/1361-6463/aaaf9d.

[9] E. Wyrwas, L. Condra, A. Hava, Accurate Quantitative Physics-of-Failure Approach to Integrated Circuit Reliability, in: IPC APEX EXPO Technical Conference, 2011: pp. 3:1776–1815.

[10] G. Wehmeyer, T. Yabuki, C. Monachon, J. Wu, C. Dames, Thermal diodes, regulators, and switches: Physical mechanisms and potential applications, Appl Phys Rev. 4 (2017) 41304. https://doi.org/10.1063/1.5001072.

[11] A. Sood, F. Xiong, S. Chen, H. Wang, D. Selli, J. Zhang, C.J. Mcclellan, J. Sun, D. Donadio, Y. Cui, E. Pop, K.E. Goodson, An electrochemical thermal transistor, Nat Commun. (2018) 41866–41874. https://doi.org/10.1038/s41467-018-06760-7.

[12] M.E. Chen, M.M. Rojo, F. Lian, J. Koeln, A. Sood, S.M. Bohaichuk, C.M. Neumann, S.G. Garrow, K.E. Goodson, A.G. Alleyne, E. Pop, Graphene-based electromechanical thermal switches, 2d Mater. 8 (2021). https://doi.org/10.1088/2053-1583/abf08e.

[13] J. Li, K.B. Nam, M.L. Nakarmi, J.Y. Lin, H.X. Jiang, Band structure and fundamental optical transitions in wurtzite AlN, Appl Phys Lett. 83 (2003) 5163–5165. https://doi.org/10.1063/1.1633965.

[14] M. Feneberg, R.A.R. Leute, B. Neuschl, K. Thonke, M. Bickermann, High-excitation and high-resolution photoluminescence spectra of bulk AlN, Phys Rev B. 82 (2010) 1–8. https://doi.org/10.1103/PhysRevB.82.075208.

[15] J.D. Albrecht, T. Chang, A.S. Kane, M.J. Rosker, B. Allen, N.F. Drive, DARPA's Nitride Electronic NeXt Generation Technology Program, (2010).

[16] R.L. Xu, M. Munõz Rojo, S.M. Islam, A. Sood, B. Vareskic, A. Katre, N. Mingo, K.E. Goodson, H.G. Xing, D. Jena, E. Pop, Thermal conductivity of crystalline AlN and the influence of atomic-scale defects, J Appl Phys. 126 (2019). https://doi.org/10.1063/1.5097172.

[17] Z. Cheng, Y.R. Koh, A. Mamun, J. Shi, T. Bai, K. Huynh, L. Yates, Z. Liu, R. Li, E. Lee, M.E. Liao, Y. Wang, H.M. Yu, M. Kushimoto, T. Luo, M.S. Goorsky, P.E. Hopkins, H. Amano, A. Khan, S. Graham, Experimental observation of high intrinsic thermal conductivity of AlN, Phys Rev Mater. 4 (2020) 1–7. https://doi.org/10.1103/PhysRevMaterials.4.044602.

[18] Y.R. Koh, Z. Cheng, A. Mamun, S. Bin Hoque, Z. Liu, T. Bai, K. Hussain, M.E. Liao, R. Li, J.T. Gaskins, A. Giri, J. Tomko, L. Braun, M. Gaevski, E. Lee, L. Yates, M.S. Goorsky, T. Luo, A. Khan, S. Graham, P.E. Hopkins, Bulk-like Intrinsic Phonon Thermal Conductivity of Micrometer- Thick AlN Films, ACS Appl Mater Interfaces. 12 (2020) 29443–29450. https://doi.org/10.1021/acsami.0c03978.

[19] P.K. Kuo, G.W. Auner, Z.L. Wu, Microstructure and thermal conductivity of epitaxial AlN thin films, Thin Solid Films. 253 (1994) 223–227.

[20] M.S. Bin Hoque, Y.R. Koh, J.L. Braun, A. Mamun, Z. Liu, K. Huynh, M.E. Liao, K. Hussain, Z. Cheng, E.R. Hoglund, D.H. Olson, J.A. Tomko, K. Aryana, R. Galib, J.T. Gaskins, M.M.M. Elahi, Z.C. Leseman, J.M. Howe, T. Luo, S. Graham, M.S. Goorsky, A. Khan, P.E. Hopkins, High In-Plane Thermal Conductivity of Aluminum Nitride Thin Films, ACS Nano. 15 (2021) 9588–9599. https://doi.org/10.1021/acsnano.0c09915.

[21] F. Deprat, C. Fenouillet-Beranger, V. Jousseaume, C. Guerin, V. Beugin, N. Rochat, C. Licitra, V. Caubet-Hilloutou, D. Benoit, G. Imbert, N. Rambal, P. Batude, M. Vinet, Dielectrics stability for intermediate BEOL in 3D sequential integration, Microelectron Eng. 167 (2017) 90–94. https://doi.org/https://doi.org/10.1016/j.mee.2016.11.006.

[22] C. Fenouillet-Beranger, S. Beaurepaire, F. Deprat, A.A. de Sousa, L. Brunet, P. Batude, O. Rozeau, F. Andrieu, P. Besombes, M.-P. Samson, B. Previtali, F. Nemouchi, G. Rodriguez, P. Rodriguez, R. Famulok, N. Rambal, V. Balan, Z. Saghi, V. Jousseaume, C. Guerin, F. Ibars, F. Proud, D. Nouguier, D. Ney, V. Delaye, H. Dansas, X. Federspiel, M. Vinet, Guidelines for intermediate back end of line (BEOL) for 3D sequential integration, in: 2017 47th European Solid-State Device Research Conference (ESSDERC), 2017: pp. 252–255. https://doi.org/10.1109/ESSDERC.2017.8066639.

[23] J. Schmitz, Low temperature thin films for next-generation microelectronics (invited), Surf Coat Technol. 343 (2018) 83–88. https://doi.org/https://doi.org/10.1016/j.surfcoat.2017.11.013.

[24] C. Mion, J.F. Muth, E.A. Preble, Accurate dependence of gallium nitride thermal conductivity on dislocation density, Appl Phys Lett. 89 (2006) 1–3. https://doi.org/10.1063/1.2335972.

[25] T.E. Beechem, A.E. Mcdonald, E.J. Fuller, Size dictated thermal conductivity of GaN Size dictated thermal conductivity of GaN, J Appl Phys. 120 (2016) 1–6. https://doi.org/10.1063/1.4962010.

[26] H. Kwon, C. Perez, H.K. Kim, M. Asheghi, W. Park, K.E. Goodson, Thermal Interface Enhancement via Inclusion of an Adhesive Layer Using Plasma-Enhanced Atomic Layer Deposition, ACS Appl Mater Interfaces. 13 (2021) 21905–21913. https://doi.org/10.1021/acsami.0c19197.

[27] H. Kwon, C. Perez, W. Park, M. Asheghi, K.E. Goodson, Thermal Characterization of Metal–Oxide Interfaces Using Time-Domain Thermoreflectance with Nanograting Transducers, ACS Appl Mater Interfaces. 13 (2021) 58059–58065. https://doi.org/10.1021/acsami.1c12422.

[28] C. Perez, A. Jog, H. Kwon, D. Gall, M. Asheghi, S. Kumar, W. Park, K.E. Goodson, Dominant Energy Carrier Transitions and Thermal Anisotropy in Epitaxial Iridium Thin Films, Adv Funct Mater. 2207781 (2022) 1–9. https://doi.org/10.1002/adfm.202207781.

[29] S.T. Ueda, A. McLeod, D. Alvarez, D. Moser, R. Kanjolia, M. Moinpour, J. Woodruff, A.C. Kummel, Tris(dimethylamido)aluminum(III) and N2H4: Ideal precursors for the low-temperature deposition of large grain, oriented c-axis AlN on Si via atomic layer annealing, Appl Surf Sci. 554 (2021). https://doi.org/10.1016/j.apsusc.2021.149656.

[30] A.J. McLeod, S.T. Ueda, P.C. Lee, J. Spiegelman, R. Kanjolia, M. Moinpour, J. Woodruff, A.C. Kummel, Pulsed chemical vapor deposition for crystalline aluminum nitride thin films and buffer layers on silicon and silicon carbide, Thin Solid Films. 768 (2023). https://doi.org/10.1016/j.tsf.2023.139717.

[31] P. Jiang, X. Qian, R. Yang, Time-domain thermoreflectance (TDTR) measurements of anisotropic thermal conductivity using a variable spot size approach, Review of Scientific Instruments. 88 (2017). https://doi.org/10.1063/1.4991715.

[32] J.T. Gaskins, P.E. Hopkins, D.R. Merrill, S.R. Bauers, E. Hadland, D.C. Johnson, D. Koh, J.H. Yum, S. Banerjee, B.J. Nordell, M.M. Paquette, A.N. Caruso, W.A. Lanford, P. Henry, L. Ross, H. Li, L. Li, M. French, A.M. Rudolph, S.W. King, Review—Investigation and Review of the Thermal, Mechanical, Electrical, Optical, and Structural Properties of Atomic Layer Deposited High- k Dielectrics: Beryllium Oxide, Aluminum Oxide, Hafnium Oxide, and Aluminum Nitride , ECS Journal of Solid State Science and Technology. 6 (2017) N189–N208. https://doi.org/10.1149/2.0091710jss.

[33] C. Perez, R. Knepper, M.P. Marquez, E.C. Forrest, A.S. Tappan, M. Asheghi, K.E. Goodson, E.O. Ziade, Non-Contact Mass Density and Thermal Conductivity Measurements of Organic Thin Films Using Frequency – Domain Thermoreflectance, Adv Mater Interfaces. 9 (2021) 1–6. https://doi.org/10.1002/admi.202101404.

[34] Y. Zhao, C. Zhu, S. Wang, J.Z. Tian, D.J. Yang, C.K. Chen, H. Cheng, P. Hing, Pulsed photothermal reflectance measurement of the thermal conductivity of sputtered aluminum nitride thin films, J Appl Phys. 96 (2004) 4563–4568. https://doi.org/10.1063/1.1785850.

[35] S.R. Choi, D. Kim, S.H. Choa, S.H. Lee, J.K. Kim, Thermal conductivity of AlN and SiC thin films, Int J Thermophys. 27 (2006) 896–905. https://doi.org/10.1007/s10765-006-0062-1.

[36] C. Duquenne, Thermal conductivity of aluminium nitride thin films prepared by reactive magnetron sputtering, J Phys D Appl Phys. 45 (2012) 1–8. https://doi.org/10.1088/0022-3727/45/1/015301.

[37] T.S. Pan, Y. Zhang, J. Huang, B. Zeng, D.H. Hong, S.L. Wang, H.Z. Zeng, M. Gao, W. Huang, Y. Lin, Enhanced thermal conductivity of polycrystalline aluminum nitride thin films by optimizing the interface structure, J Appl Phys. 112 (2012). https://doi.org/10.1063/1.4748048.

[38] K.A. Aissa, N. Semmar, A. Achour, Q. Simon, A. Petit, J. Camus, C. Boulmer-Leborgne, M.A. Djouadi, Achieving high thermal conductivity from AlN films deposited by high-power impulse magnetron sputtering, J Phys D Appl Phys. 47 (2014). https://doi.org/10.1088/0022-3727/47/35/355303.

[39] Y. Bian, M. Liu, G. Ke, Y. Chen, J. Dibattista, E. Chan, Y. Yang, Surface & Coatings Technology Aluminum nitride thin film growth and applications for heat dissipation, Surf Coat Technol. 267 (2015) 65–69. https://doi.org/10.1016/j.surfcoat.2014.11.060.

[40] E. Yalon, Ö.B. Aslan, K.K.H. Smithe, C.J. McClellan, S. V Suryavanshi, F. Xiong, A. Sood, C.M. Neumann, X. Xu, K.E. Goodson, T.F. Heinz, E. Pop, Temperature-Dependent Thermal Boundary Conductance of Monolayer MoS2 by Raman Thermometry, ACS Appl Mater Interfaces. 9 (2017) 43013–43020. https://doi.org/10.1021/acsami.7b11641.

[41] K. Hirama, Y. Taniyasu, M. Kasu, AlGaN/GaN high-electron mobility transistors with low thermal resistance grown on single-crystal diamond (111) substrates by metalorganic vapor-phase epitaxy, Appl Phys Lett. 98 (2011). https://doi.org/10.1063/1.3574531.

[42] J.-T. Chen, J.W. Pomeroy, N. Rorsman, C. Xia, C. Virojanadara, U. Forsberg, M. Kuball, E. Janzén, Low thermal resistance of a GaN-on-SiC transistor structure with improved structural properties at the interface, J Cryst Growth. 428 (2015) 54–58.

[43] H. Shinoda, N. Mutsukura, Structural properties of GaN and related alloys grown by radio-frequency magnetron sputter epitaxy, Thin Solid Films. 516 (2008) 2837–2842. https://doi.org/10.1016/j.tsf.2007.05.035.

[44] T. Kumada, M. Ohtsuka, H. Fukuyama, Influence of substrate temperature on the crystalline quality of AlN layers deposited by RF reactive magnetron sputtering, AIP Adv. 5 (2015). https://doi.org/10.1063/1.4906796.

[45] J. Cho, D. Francis, P.C. Chao, M. Asheghi, K.E. Goodson, Cross-Plane Phonon Conduction in Polycrystalline Silicon Films, J Heat Transfer. 137 (2015) 71303. https://doi.org/10.1115/1.4029820.

[46] N. Matsunami, H. Kakiuchida, M. Sataka, S. Okayasu, XRD Characterization of AlN Thin Films Prepared by Reactive RF-Sputter Deposition, Advances in Materials Physics and Chemistry. 03 (2013) 101–107. https://doi.org/10.4236/ampc.2013.31a012.

[47] F. El Akkad, M. Marafi, A. Punnoose, G. Prabu, Effect of substrate temperature on the structural, electrical and optical properties of ITO films prepared by RF magnetron sputtering, Physica Status Solidi A Appl Res. 177 (2000) 445–452. https://doi.org/10.1002/(SICI)1521-396X(200002)177:2<445::AID-PSSA445>3.0.CO;2-N.

[48] C. Gonçalves, S. Charvet, A. Zeinert, M. Clin, K. Zellama, Nanocrystalline silicon thin films prepared by radiofrequency magnetron sputtering, Thin Solid Films. (2002) 91–96.

[49] H. Jin, B. Feng, S. Dong, C. Zhou, J. Zhou, Y. Yang, T. Ren, J. Luo, D. Wang, Influence of substrate temperature on structural properties and deposition rate of AlN thin film deposited by reactive magnetron sputtering, J Electron Mater. 41 (2012) 1948–1954. https://doi.org/10.1007/s11664-012-1999-4.

[50] W.A. Little, The transport of heat between dissimilar solids at low temperatures, Can J Phys. 37 (1959) 334–349.

[51] E.T. Swartz, R.O. Pohl, Thermal boundary resistance, Rev Mod Phys. 61 (1989) 605–668. https://doi.org/10.1103/RevModPhys.61.605.

[52] C. Monachon, L. Weber, C. Dames, Thermal Boundary Conductance: A Materials Science Perspective, Annu Rev Mater Res. 46 (2016) 433–463. https://doi.org/10.1146/annurev-matsci-070115-031719.

[53] W. Liu, A.A. Balandin, Thermal conduction in AlxGa1-xN alloys and thin films, J Appl Phys. 97 (2005). https://doi.org/10.1063/1.1868876.

[54] S.I. Yi, C. Yu, Modeling of thermoelectric properties of SiGe alloy nanowires and estimation of the best design parameters for high figure-of-merits, J Appl Phys. 117 (2015). https://doi.org/10.1063/1.4906226.

[55] S.I. Yi, V. Attari, M. Jeong, J. Jian, S. Xue, H. Wang, R. Arroyave, C. Yu, Strain-induced suppression of the miscibility gap in nanostructured Mg2Si-Mg2Sn solid solutions, J Mater Chem A Mater. 6 (2018) 17559–17570. https://doi.org/10.1039/c8ta05798b.

[56] D.T. Morelli, J.P. Heremans, G.A. Slack, Estimation of the isotope effect on the lattice thermal conductivity of group IV and group III-V semiconductors, Phys Rev B Condens Matter Mater Phys. 66 (2002) 1953041–1953049. https://doi.org/10.1103/PhysRevB.66.195304.

[57] B.E. Gaddy, Z. Bryan, I. Bryan, J. Xie, R. Dalmau, B. Moody, Y. Kumagai, T. Nagashima, Y. Kubota, T. Kinoshita, A. Koukitu, R. Kirste, Z. Sitar, R. Collazo, D.L. Irving, The role of the carbon-silicon complex in eliminating deep ultraviolet absorption in AlN, Appl Phys Lett. 104 (2014). https://doi.org/10.1063/1.4878657.

[58] G.A. Slack, C.J. Glassbrenner, Thermal conductivity of Si and Ge from 3K to the melting point, Physical Review. 134 (1964) A1058–A1069. https://journals.aps.org/pr/pdf/10.1103/PhysRev.134.A1058.

[59] G.A. Slack, R.A. Tanzilli, R.O. Pohl, J.W. Vandersande, The intrinsic thermal conductivity of AlN, Journal of Physics and Chemistry of Solids. 48 (1987) 641–647. https://doi.org/https://doi.org/10.1016/0022-3697(87)90153-3.

[60] D.T. Morelli, C.P. Beetz, T.A. Perry, Thermal conductivity of synthetic diamond films, J Appl Phys. 64 (1988) 3063–3066. https://doi.org/10.1063/1.341571.

[61] S.M. Lee, D.G. Cahill, Heat transport in thin dielectric films, J Appl Phys. 81 (1997) 2590–2595. https://doi.org/10.1063/1.363923.

[62] A.W. Jackson, J.P. Ibbetson, A.C. Gossard, U.K. Mishra, Reduced thermal conductivity in low-temperature-grown GaAs, Appl Phys Lett. 74 (1999) 2325–2327. https://doi.org/10.1063/1.123839.

[63] AzoM, Gallium Arsenide (GaAs) Semiconductors, Https://Www.Azom.Com/Article.Aspx?ArticleID=8349. (2013).

[64] R. Yan, J.R. Simpson, S. Bertolazzi, J. Brivio, M. Watson, X. Wu, A. Kis, T. Luo, A.R.H. Walker, H.G. Xing, Thermal conductivity of monolayer molybdenum disulfide obtained from temperature-dependent Raman spectroscopy, ACS Nano. 8 (2014) 986–993. https://doi.org/10.1021/nn405826k.

[65] N. Peimyoo, J. Shang, W. Yang, Y. Wang, C. Cong, T. Yu, Thermal conductivity determination of suspended mono- and bilayer WS2 by Raman spectroscopy, Nano Res. 8 (2015) 1210–1221. https://doi.org/10.1007/s12274-014-0602-0.

[66] Z. Lin, C. Liu, Y. Chai, High thermally conductive and electrically insulating 2D boron nitride nanosheet for efficient heat dissipation of high-power transistors, 2d Mater. 3 (2016). https://doi.org/10.1088/2053-1583/3/4/041009.

[67] J.S. Kang, M. Li, H. Wu, H. Nguyen, Y. Hu, Experimental observation of high thermal conductivity in boron arsenide, Science (1979). 361 (2018) 575–578. https://doi.org/10.1126/science.aat5522.

[68] K. Chen, B. Song, N.K. Ravichandran, Q. Zheng, X. Chen, H. Lee, H. Sun, S. Li, G.A.G.U. Gamage, F. Tian, Z. Ding, Q. Song, A. Rai, H. Wu, P. Koirala, A.J. Schmidt, K. Watanabe, B. Lv, Z. Ren, L. Shi, D.G. Cahill, T. Taniguchi, D. Broido, G. Chen, Ultrahigh thermal conductivity in isotope-enriched cubic boron nitride, Science (1979). 367 (2020) 555–559.

[69] R. Rounds, B. Sarkar, D. Alden, Q. Guo, A. Klump, C. Hartmann, T. Nagashima, R. Kirste, A. Franke, M. Bickermann, Y. Kumagai, Z. Sitar, R. Collazo, The influence of point defects on the thermal conductivity of AlN crystals, J Appl Phys. 123 (2018). https://doi.org/10.1063/1.5028141.

[70] A. Jacquot, B. Lenoir, A. Dauscher, P. Verardi, F. Craciun, M. Stolzer, M. Gartner, M. Dinescu, Optical and thermal characterization of AlN thin films deposited by pulsed laser deposition, Appl Surf Sci. 186 (2002) 507–512.

[71] B.E. Belkerk, J. Camus, B. Garnier, H. Al Brithen, S. Sahli, M.A. Djouadi, Measuring anisotropic thermal conductivity of aluminum nitride films with the ultra-fast hot strip technique, International Journal of Thermal Sciences. 151 (2020) 1–10. https://doi.org/10.1016/j.ijthermalsci.2019.106259.

[72] J.T. Gaskins, P.E. Hopkins, D.R. Merrill, S.R. Bauers, E. Hadland, D.C. Johnson, D. Koh, J.H. Yum, S. Banerjee, B.J. Nordell, M.M. Paquette, A.N. Caruso, W.A. Lanford, P. Henry, L. Ross, H. Li, L. Li, M. French, A.M. Rudolph, S.W. King, Review—Investigation and Review of the Thermal, Mechanical, Electrical, Optical, and Structural Properties of Atomic Layer Deposited High- k Dielectrics: Beryllium Oxide, Aluminum Oxide, Hafnium Oxide, and Aluminum Nitride, ECS Journal of Solid State Science and Technology. 6 (2017) N189–N208. https://doi.org/10.1149/2.0091710jss.